HIGH ENERGY PHOTOPRODUCTION OF THE ρ AND ρ' VECTOR MESONS

E-87
or
E-358

BY

JOHN MICHAEL BRONSTEIN

B.A., Illinois Wesleyan University, 1970
M.S., University of Illinois, 1972

THESIS

Submitted in partial fulfillment of the requirements
for the degree of Doctor of Philosophy in Physics
in the Graduate College of the
University of Illinois at Urbana-Champaign, 1977

Urbana, Illinois

HIGH ENERGY PHOTOPRODUCTION OF THE ρ AND ρ' VECTOR MESONS

John Michael Bronstein, Ph. D.
Department of Physics
University of Illinois at Urbana-Champaign, 1977

In an experiment in the broad band photon beam at Fermilab we observe diffractive production of $2\pi^{\pm}$ and $4\pi^{\pm}$ states from Be, Al, Cu and Pb targets. The $2\pi^{\pm}$ data is dominated by the $\rho(770)$ and the $4\pi^{\pm}$ is dominated by the $\rho'(1500)$.

We measure the energy dependence of ρ photoproduction from Be and see no evidence for energy variation of the forward cross section in the range 30 to 160 GeV. The forward cross section is consistent with its average value $d\sigma/dt\big|_0 = 3.42 \pm 0.28\ \mu b/\mathrm{GeV}^2$ over the entire range.

We obtain for the ρ' a mass of 1487 ± 20 MeV and a width of 675 ± 60 MeV. All quoted errors are statistical.

A standard optical model analysis of the A dependence of the ρ and ρ' photoproduction yields the following results.

$$f^2_{\rho'}/f^2_{\rho} = 3.7 \pm 0.7$$

$$\sigma_{\rho'}/\sigma_{\rho} = 1.05 \pm 0.18$$

Our results for the photon coupling constants are in good agreement

with GVMD and with the e^+e^- storage ring results. The approximate equality of the ρ-nucleon and ρ'-nucleon total cross sections is inconsistent with the diagonal version of GVMD and provides strong motivation for including transitions between different vector mesons in GVMD.

ACKNOWLEDGMENTS

I wish to express my appreciation for the efforts of the many people who have contributed to the successes of Experiment 87A and have helped make the work described in this thesis possible. Some of the people and groups who have contributed most directly to the experiment and my education in high energy experimental physics are listed below.

It is a particular pleasure to be able to thank my advisor Dr. Michael Gormley for his help and support. Both by instruction and example he has shown the techniques and the insight needed to do high energy physics. He has always been available for help and advice, giving his time generously in his role as teacher and advisor.

I must thank Dr. Albert Wattenberg both for getting me started in the high energy physics group and for his continuing attention and constructive criticism during my time in the group. His appreciation of the importance of experimental technique has been valuable throughout the experiment.

It has been a privilege to work with Dr. Wonyong Lee, who has provided the leadership and foresight that was so crucial to the existence and success of the experiment.

The following people have given helpful discussions and other input during the work in this thesis: Dr. M. Binkley, Dr. Joel Butler, Dr. R. Messner, Dr. B. C. Knapp, Dr. G. Gladding, Rick Coleman, Maury Goodman, and Jim Russell.

The senior collaborators in the experiment have contributed not only to the experiment but to my education in physics. In addition to those already mentioned these individuals include Dr. J. Peoples, Dr. Irwin Gaines, Dr. A. L. Read, Dr. R. Orr, Dr. T. A. O'Halloran, and Dr. D. Yount.

My fellow graduate students during the course of the experiment have given their hard work and dedication to the experiment and have provided countless interesting and informative hours of discussion. These include Dean Wheeler, Larry Cormell, John Sarracino, Pat Leung, Dave Smith, Tony Wijanco, Dave Nease and Jim Knauer.

For technical support, I wish to thank Leonard Seward, Ken Gray, Sal Marino, and the personnel of the Fermilab Proton Department.

Computing support was provided by the Fermilab Computing Department and the University of Illinois High Energy Physics Group computing staff.

Innovative electronics has been custom designed and built for the experiment by the University of Illinois High Energy Physics Group electronics shop, including Joe Simaitis, Bob Downing, and Tom Noggle, and by the Nevis Laboratory electronics shop under the direction of Bill Sippach. It is a pleasure to be able to recognize the important contributions made by these individuals.

I take this unique opportunity to put the debt I owe my wife Linda "on the record". She has supported me throughout my graduate career, where support must be read with all its meanings to cover her contributions. She makes all the difference.

This work was funded in part by the U.S. Energy Research and Development Administration under Contract AT(11-1)-1195.

TABLE OF CONTENTS

Chapter

CHAPTER I. INTRODUCTION

Traditionally when a new energy range becomes available in elementary particle reactions a number of the relatively well understood experiments from lower energies are performed to look for new phenomena in understandable surroundings. In high-energy photon physics this has been less the case than is usual because of the interest in the new charmed spectroscopy. However, in this thesis we present data on vector meson photoproduction from nuclear targets, analyzed within the framework of a standard optical model. This type of work has been very successful in providing basic information about the ρ, ω, ϕ, and ψ vector mesons in low-energy photoproduction.

Aside from operating with high proton momenta (30-180 GeV), our results are novel in presenting the first A (nucleon number) dependence analysis of ρ' photoproduction. The $\pi^+\pi^-\pi^+\pi^-$ state we call the ρ' is also called ρ' (1600) and ρ'' in the literature. We record both ρ and ρ' production during the same beam exposure in our apparatus to avoid systematic problems. Be, Al, Cu, and Pb targets are used.

We compare the A dependence of ρ and ρ' photoproduction to determine the relative ρ and ρ'-photon coupling constants and the relative ρ and ρ'-nucleon total cross sections, parameters of fundamental importance in understanding the vector mesons and their relationship to the interactions of the photon. In particular, our finding of approximate equality of the ρ-nucleon and ρ'-nucleon total cross sections is in sharp disagreement with the diagonal version of Generalized Vector Meson Dominance (GVMD). We also measure the energy dependence of forward production of the ρ from beryllium (in our new energy range) and find no evidence for energy variation of the forward cross section in the range of 30 to 160 GeV.

The work we describe here represents part of the results obtained from the first high-energy photoproduction experiment performed in the Fermi National Accelerator Laboratory (Fermilab) broad band photon beam. The experiment was performed by a collaboration of physicists from Columbia University, Cornell University, University of Hawaii, University of Illinois, and Fermilab, operating as Fermilab Experiment #87A [Lee et al., 1970]. This experiment was motivated by a desire to understand the interactions of the photon and its relationship to the vector mesons, and the conviction that high-energy photoproduction is both a fertile source of new phenomena and an ideal testing ground for our current theories of the nature of the photon.

CHAPTER II. THEORETICAL BACKGROUND

A. Vector Mesons and VMD

The way in which high-energy photons interact with hadrons is generally well described by vector meson dominance (VMD) [Sakurai, 1969]. In this thesis we present data on the photoproduction of ρ and ρ' vector mesons which is most easily discussed and analyzed in the generally successful framework of VMD. This approach is especially natural because the comparative properties of the ρ and ρ' states play important roles in the various versions of the VMD model.

The photon interacts with hadrons in two ways: electromagnetically and hadronically. For example, when a photon of several GeV energy interacts with a proton by far the most likely occurrence is the production of an e^+e^- pair by the Bethe-Heitler mechanism. This is a QED process that disappears if the hadron is not charged. If one removes these electromagnetic processes from consideration, which we do from now on, one is left with a number of hadronic processes with a total cross section of about 1/200 that of the πp cross section. This behavior is attributed to the photon virtually coupling to hadronic states; these states then interact in typical hadronic fashion. The small cross section is due to the small coupling of the photon to the hadronic states.

The nature of this hadronic component of the photon is suggested by the observation that neutral vector mesons (ρ, ω, ϕ, ρ', ψ, etc.) are diffractively photoproduced. The vector mesons are particles with spin one and odd parity, like the photon itself. If one thinks of the photon acquiring hadronic properties by virtually coupling to hadrons, these particles are natural candidates. The diffractive nature of vector meson photoproduction is especially suggestive.

Diffractive behavior is common to high-energy hadron-hadron scattering and is often viewed geometrically as the strong absorption of the projectile by the target, yielding effects reminiscent of diffraction from a black screen in optics. The scattering amplitude is mainly imaginary (absorptive), the cross section is constant or at most logarithmically rising with energy, and the scattering is peaked sharply in the forward direction, with an approximately exponential falloff with $-q^2$ (squared momentum transfer in the scatter). Other diffractive effects in hadron-hadron scattering are factorization of the target and projectile behavior and vacuum quantum number exchange between the target and projectile (t channel). The polarization of diffracted particles suggests s-channel helicity conservation (SCHC), described briefly in Chapter IV.

VMD has its origins in attempts to understand the nucleon form factors [Nambu, 1957], [Frazer and Fulco, 1960] and in the analogy between photon-electromagnetic current coupling and the conserved currents of the strong interactions [Sakurai, 1960]. This latter idea is that vector mesons exist which couple universally to the isotopic spin, hypercharge, and baryon currents. These mesons can be identified with suitable mixtures of the ρ, ω, and ϕ. A formal statement of VMD that requires this universality of coupling for consistency is the current field identity (CFI) [Joos, 1967], [Kroll, Lee, and Zumino, 1967].

$$j_\mu^{em}(x) \equiv -\sum_V \frac{m_V^2}{f_V} V_\mu(x). \qquad \text{(II.A. 1)}$$

In the CFI j_μ^{em} is the hadronic part of the electromagnetic current, V_μ is the vector meson field, m_V is the mass of vector meson V and f_V is the photon-V coupling constant. The symbol "V" is to be read as any neutral vector meson. We should note that several other notations for the photon vector meson coupling constant exist. The other popular one is $\gamma_V = f_V/2$ and occasionally $g_{\gamma V} = 2(\pi\alpha)^{\frac{1}{2}}/f_V$ is encountered. This latter notation makes some of the formulas look simpler (α is the fine structure constant), and has the intuitive advantage of getting larger as the strength of the coupling between the photon and the vector meson increases. When experimental values of these parameters are quoted, it is generally as $\gamma_V^2/4\pi$ or $f_V^2/4\pi$.

The CFI is for the sum of all neutral vector mesons. At first this included only the ρ, ω, and ϕ, but as additional vector mesons have been established (ρ', ψ) they are included. Also in order to correct certain deficiencies in VMD a spectrum or continuum of additional vector states is hypothesized and included in VMD. We return to these extensions after exploring the predictions of simple VMD in vector meson photoproduction.

To obtain predictions about photon interactions based on the CFI, additional assumptions are made in the VMD model. For example, to apply VMD to vector meson photoproduction, the process is visualized as occurring by the photon coupling to the virtual vector meson, which then scatters from the target, exchanging momentum to become a real particle (on the mass shell). It is assumed that the vector meson mass (off-shell) effects on the scattering are small, so that the photoproduction process is the same as vector meson scattering except for the vector meson propagator and the photon vector meson coupling given by f_V. Similarly the coupling constant itself is assumed to be insensitive to the mass squared (q^2) of the photon. $q^2 = 0$ in photoproduction, but other q^2 regions are accessible using virtual photons from different sources. For example, if an e^+ and e^- collide and annihilate they create a photon with positive q^2. If the e^+e^-

energy was such that $q^2 = m_V^2$, the squared mass of a vector meson of type V, the photon could materialize as the vector meson via its f_V coupling. The assumption is that f_V measured from this process is the same as in photoproduction. For the vector mesons studied up to the present time this appears to be at least approximately true [Leith, 1977]. We are trying to describe photoproduction and one additional VMD assumption is usually used. This is that the various vector mesons do not couple directly to one another. Thus a photon cannot couple to a ϕ, for example, which then transforms into an ω as it scatters from the target to contribute to ω photoproduction. In the past photoproduction experiments involving ρ, ω, ϕ, and ψ have given no direct evidence of these $V \rightarrow V'$ transitions (V and V' are different vector mesons). The assumption that these transitions are indeed negligible is called the diagonal approximation.

Using the above assumptions about the details of photon-vector meson interactions VMD provides the following prediction relating vector meson photoproduction and vector meson scattering.

$$\frac{d\sigma}{dt}(\gamma N \rightarrow VN) = \frac{4\pi\alpha}{f_V^2}\frac{d\sigma}{dt}(VN \rightarrow VN). \qquad \text{(II.A. 2)}$$

In the above $d\sigma/dt$ is the differential cross section for scattering (or production) and $VN \rightarrow VN$ ($\gamma N \rightarrow VN$) is the notation indicating vector meson scattering (photoproduction) from a nucleon. α is the fine structure constant; t is the squared momentum transfer in the scatter or production and is a Lorentz scalar. If P_i and P_f are the initial and final target 4-momenta, then t can be defined as follows.

$$t \equiv (P_i - P_f)^2. \qquad \text{(II.A. 3)}$$

The optical theorem is continually used in simple VMD arguments.

$$\mathrm{Im}\, f(0) = \frac{\sigma_V}{\sqrt{16\pi}}\ , \text{ where } \frac{d\sigma}{dt} = |f(t)|^2 \qquad \text{(II.A. 4)}$$

σ_V is the V-nucleon total cross section and Im f(0) is the imaginary part of the forward scattering amplitude. We can apply the optical theorem to (II. A. 2) to obtain the following VMD result for the t = 0 limit of the vector meson photoproduction differential cross section, $d\sigma/dt|_0(\gamma N \rightarrow VN)$.

$$\left.\frac{d\sigma}{dt}\right|_0 (\gamma N \rightarrow VN) = \frac{4\pi\alpha}{16\pi f_V^2}(1 + \alpha_V^2)\sigma_V^2 . \qquad \text{(II.A. 5)}$$

In the above, α_V is the ratio of real to imaginary parts of the forward vector meson-nucleon scattering amplitude, not to be confused with α, the fine structure constant.

Many more applications of VMD exist, even limiting the discussion to real photons ($q^2 = 0$). In the model of vector meson photoproduction, for example, the outgoing vector meson could recouple to the photon if it stayed at $q^2 = 0$. This would be photon elastic scattering from a nucleon, called Compton scattering. VMD models Compton scattering as the sum of all such processes for all types of vector mesons. This process can be related simply to the photon-nucleon total cross section via the optical theorem. The details and experimental success of these vector meson sum expressions for Compton scattering and the photon total cross section are reviewed in [Leith, 1977]. They basically come up short of accounting for all of the Compton scattering by 20% when (ρ, ω, ϕ, ρ') are included.

Elementary relations in VMD need σ_V, f_V^2, and α_V for the vector mesons. One theoretical source for some useful information is the quark model. For example, a simple prediction [Lipkin, 1966] exists for σ_ρ, the ρ-nucleon total cross section in terms of σ_{π^+} and σ_{π^-}, the π^+ and π^--nucleon total cross sections.

$$\sigma_\rho = \tfrac{1}{2}(\sigma_{\pi^+} + \sigma_{\pi^-}). \qquad \text{(II.A.6)}$$

σ_ρ has been determined by an optical model analysis of ρ photoproduction from nuclear targets to be in the range 28-30mb by low energy ($\leq$ 10 GeV) photoproduction experiments, in good agreement with (II.A.6). Because we use the optical-model approach to determining $\sigma_{\rho'}/\sigma_\rho$ we return to this technique in Section C (and Appendix A). The quark model and ω-ϕ mixing give a prediction for the ratios of the photon-vector meson coupling constants for the lowest lying vector mesons [Freund, 1966], [Gaillard, Lee, and Rosner, 1974].

$$\frac{1}{f_\rho^2} : \frac{1}{f_\omega^2} : \frac{1}{f_\phi^2} : \frac{1}{f_\psi^2} = 9 : 1 : 2 : 8. \qquad \text{(II.A.7)}$$

Except for the ψ the experimental data follow this ratio crudely. The ψ is low and it has been suggested [Leith, 1977] that the q^2 dependence of the coupling constant may be becoming important for the ψ.

Before moving on to generalizations and extensions to VMD we should remark that the ρ alone accounts for much of the photon's hadronic behavior. This is not hard to appreciate from the standpoint of conventional VMD. The σ_ϕ and σ_ψ are approximately 1/3 and 1/15 of σ_ρ so that their photoproduction contribution is suppressed because they do not interact as readily with the target. Beyond that the coupling of the ω, ϕ, and ψ to the photon are suppressed relative to the ρ, so the photon spends less time coupled to them. Thus in accounting for the total hadronic interaction of the photon the ρ alone accounts for about 70% of the VMD contributions.

B. Families of Vector Mesons and GVMD

As we indicated in the last section the low-lying vector mesons (including the ρ') do not saturate the VMD prediction for Compton scattering. About 20% is left and an obvious "out" is to assume this is taken up by higher mass vector mesons, perhaps quite wide, not yet seen experimentally. A possible model for such a mass spectrum is provided by the Veneziano model in Regge theory [Veneziano, 1968], [Shapiro, 1969], and [Berger and Cline, 1969]. This model contains an explicit duality between the s-channel resonances and the t-channel Regge exchanges in describing π-π scattering. One consequence of this type of theory is the existence of lower lying "daughter" trajectories below the first $\pi\pi$ resonance trajectory, the ρ. Each of these has a spin-parity 1-minus member, like the ρ but at higher mass. This family behavior is also known as a meson tower, when viewed at fixed mass and counting the states of higher spin as a family or tower. This type of model predicts the following mass spectrum for the 1-minus ρ daughters,

$$m_V^2 = m_\rho^2 (an + 1), \; n = 0, 1, 2, \ldots \qquad \text{(II.B. 1)}$$

with $a \approx 2$.

Additional motivation exists for creating a GVMD (generalized vector meson dominance) by the addition of a spectrum of high mass vector mesons to VMD. GVMD can give the correct general behavior of photon processes with $q^2 \neq 0$. e^+e^- annihilation explores $q^2 > 0$, because this process is apparently dominated by single photon exchange. If we consider e^+e^- annihilations creating $\mu^+\mu^-$ versus any hadronic final state, the behavior at large s (center of mass energy squared) of the ratio R_V of total hadronic production to $\mu^+\mu^-$ production is independent of s. This is complicated by the threshold of new particle production at $(s)^{\frac{1}{2}} \simeq 3.8$-$3.9$ GeV, associated with charm, but above and below this threshold R_V is flat (both numerator and denominator go as s^{-1}) [Feldman and Perl, 1977]. If R_V is modeled by only a finite number of vector mesons it must eventually fall as s^{-3} when s is sufficiently above m_V^2 of the most massive vector meson [Perl, 1975].

Thus we need an unbounded mass spectrum of vector mesons to make R_V constant at large s. Clearly if the mass spectrum and photon vector meson coupling constants of an infinite number of vector mesons are specified, any behavior can be obtained for R_V. In GVMD the Veneziano type mass spectrum of Equation (II.B. 1) with a = 2 is used. The correct behavior of R_V is achieved with the following relationship between the photon-vector meson couplings in a vector meson family,

$$\frac{f_V^2}{f_\rho^2} = \frac{m_V^2}{m_\rho^2}, \qquad \text{(II.B. 2)}$$

where to be definite we have written the expression for the ρ family. This relation is common to all the GVMD models that we discuss.

A basic distinction between the various GVMD models that have been proposed is their treatment of the diagonal approximation generally used in VMD. The earlier models use the diagonal approximation (i. e., do not allow VN → V'N transitions, with N a nucleon and V and V' any two different vector mesons) [Sakurai and Schildknecht, 1972a, b, c] [Greco, 1973]. We have just outlined how these models confront e^+e^- annihilation experiments where q^2 is positive. At $q^2 = 0$ all the GVMD models predict a simple rescaling of the ρ contribution to the Compton sum rule that accounts for much of the missing 20% from VMD. At $q^2 < 0$ a more demanding challenge exists that puts some fundamental constraints on the model. This q^2 region is accessible in deep inelastic electron scattering. This process is, like e^+e^- annihilation, thought of as a single photon exchange process. The electron emits a $q^2 < 0$ photon which then interacts with the target nucleon. In this regime, however, s and q^2 can be varied independently so that the virtual photon's cross section is a function of both s and q^2. The challenge to VMD is seen in the expression for $\sigma_\gamma^T(s,q^2)$ for the contribution via VMD of one vector meson. $\sigma_\gamma^T(s,q^2)$ is the total cross section for a transverse photon on a nucleon. This can be calculated from the VMD relation for virtual Compton scattering and the optical theorem [Stodolsky, 1967].

$$\sigma_\gamma^T(s,q^2) = \frac{4\pi\alpha}{f_V^2}\left(\frac{m_V^2}{m_V^2 - q^2}\right)^2 \sigma_V^T(s;m_V^2). \tag{II.B.3}$$

For any finite sum of such terms at large $-q^2$ the cross section must eventually go as $1/q^4$. The e^-p scattering data indicate $-1/q^2$ behavior at large $-q^2$ [Kendall, 1971]. By using the Veneziano vector meson mass spectrum along with relation (II. B. 2) diagonal GVMD can give this behavior if the following relation is satisfied for the vector meson nucleon total cross sections in a family of vector mesons,

$$\frac{\sigma_V^2}{\sigma_\rho^2} = \frac{m_\rho^2}{m_V^2}, \tag{II.B.4}$$

where to be definite we have written the expression for the ρ family.

Non-diagonal models give more freedom in modeling the q^2 behavior of photon mediated processes and non-diagonal terms may be necessary to model some of the details of e^-p scattering ($q^2 < 0$)[Chavin, 1976] or to resolve some inconsistencies in the ϕ-photon coupling constant experimental situation [Leith, 1977]. One such model is that of Fraas, Read, and Shildknecht, [FRS, 1975]. In that model only non-diagonal transitions between adjacent states in the same family is allowed. In this model the correct q^2 behavior for ($q^2 < 0$) photo-processes is obtained by the following requirement, which should be compared with (II. B. 4).

$$\frac{\sigma_V^2}{\sigma_\rho^2} = 1. \tag{II.B.5}$$

As the authors themselves point out, the FRS model of GVMD is only one of many possible off-diagonal models, and indeed they feel the nearest neighbor transitions they consider are an approximation for more general behavior. [Zalewski, 1977] has made explicit some of the range of behavior possible in GVMD models with and without the diagonal approximation. Using the standard relations (II. B. 1) and (II. B. 2) he uses the requirement of the proper q^2 behavior for $q^2 < 0$ (e^-p scattering) to derive 3 GVMD sum rules. By specifying the VN → V'N transitions in different ways he shows that behavior of the diagonal model or simple FRS non-diagonal model results. These sum rule results make explicit the existence of countless possible detailed non-diagonal assumptions possible in a consistent GVMD model. It is up to experiments in various photoprocesses to establish the necessity and validity of GVMD in its various non-diagonal forms.

C. Vector Meson Production from Nuclear Targets

As we have seen in the last section, GVMD, in order to accommodate the basic behavior of photon initiated hadronic processes over the range of q^2 both positive and negative, requires some definite relationships between the coupling of the vector mesons in a family to the photon and also between the vector meson nucleon total cross sections in a family of vector mesons. In particular, the ratios of vector meson-nucleon total cross sections within a family is a good indication of whether non-diagonal couplings are required. Historically, two methods have been used to measure f_V, the vector meson-photon coupling constant, and σ_V, the vector meson-nucleon total cross section. The first method is to measure f_V in a colliding e^+e^- beam experiment (at $q^2 = m_V^2$), then to use VMD and the value of f_V to extract σ_T from V photoproduction on hydrogen (at $q^2 = 0$). The other method involves only photoproduction ($q^2 = 0$), but uses a series of nuclear targets to gain extra information. This method has the advantage of being free of many of the assumptions of either VMD or GVMD. We have used the second method to gather information on f_V and σ_V for the ρ and ρ'.

The ρ' is a well established broad structure at about 1500 MeV in $\pi^+\pi^-\pi^+\pi^-$ from photoproduction that is identified as the second daughter of the ρ. We photoproduce this state in sufficient numbers to make possible a comparison of $f_{\rho'}^2/4\pi$ with $f_\rho^2/4\pi$ and $\sigma_{\rho'}$ with σ_ρ.

We explain the technique of extracting $f_V^2/4\pi$ and σ_V from the A (nucleon number) dependence of vector meson production from nuclei in Appendix A, along with a number of elementary examples of the model and sketches of its deviation. The computational aspects of the model we use are covered briefly in Chapter IV. The model we use is called an optical model because some of the approximations in deriving it and its general behavior are reminiscent of the eikonal approximation in optics. The A dependence of the production determines σ_V and then the normalization determines $f_V^2/4\pi$.

One point about the optical model we use should be stressed here. It is basically identical to the model used to analyze all the previous low-energy A dependence photoproduction data. It contains in it the diagonal approximation discussed in the previous section. When the derivation is sketched in Appendix A for the ρ, for-example, we explicitly write the contributions to the ρ scattering in the nucleus and at no time do we allow ($\rho N \rightarrow \rho' N$) transitions or any other vector meson changing transitions. Non-diagonal optical models have been derived, some of which become mathematically cumbersome. These models are reviewed by [Grammer and Sullivan, 1977]. In using the standard optical model for our analysis, we are adhering to the philosophy in the introduction of meeting new data first with established techniques. In fact we find from this analysis an interesting result. The diagonal approximation built into the model is inconsistent with GMVD together with our own result on $\sigma_{\rho'}/\sigma_{\rho}$. Thus a conventional analysis is decisive in ruling out the standard generalized model.

CHAPTER III. EXPERIMENTAL DETAILS

A. The Beam

The photoproduction data we present in this thesis were taken in the broad-band photon beam, located in the Proton East beam of the Fermi National Accelerator Laboratory (Fermilab). The apparatus is that of the Columbia-Hawaii-Illinois-Fermilab Collaboration, operating as Fermilab Experiment #87A. This beam and apparatus have been described in detail a number of times; two sources likely to be available to readers of this thesis are [Sarracino, 1976] and [Cormell, 1976]. Certain details are best covered in [Wijanco, 1976] , including the proportional chambers and track reconstruction. We concentrate here on the pieces of apparatus and details relevant to the analysis at hand and neglect topics dealing with the many other uses to which this apparatus has been put.

The proton beam energy for these data is 300 GeV with an average intensity of 3×10^{11} protons/pulse. The pulse length is about one second at approximately 10-second intervals. The beam itself comes in bunches (called rf buckets) of less than one nanosecond duration spaced every 18.5 nanoseconds. With this fact in mind, all counters exposed to high rates are counted with pulse widths of 10 nanoseconds. The beam is not uniform in time and has many overall modulations such that the instantaneous rate varies widely during the pulse with occasional strong spikes. No reliable way is known to quantitatively measure the effective spill time or duty factor and it can only be monitored semi-qualitatively and tuned to minimize the worst effects by the accelerator operators. The same time structure exists in a secondary beam as in the primary (proton) beam. This means that we cannot examine every interaction in detail and an uncertainty exists about the quantity and quality of undetected events, measured as a dead time.

The photon beam is produced in the following way. Protons collide with a 12-inch beryllium target in our target box, illustrated in Fig. (III. A. 1), producing a large number of secondary particles of all types. The charged particles so produced along with the remaining protons are swept vertically by magnets so that only neutral particles can exit the target box through a hole located at 0° (the initial beam direction). Two classes of particles exit the target box in quantities that are important, neutral particles and muons. The muons form a halo around the beam that fills the whole area of our detector by the time they reach it, due to multiple scattering and deflection in the magnets in the rest of our beam line. They are eliminated in two ways. First, large amounts of earth, concrete, and steel surround the beam line and slowly range out the low-energy muons. Also, special spoiler magnets, as shown in the beam-line schematic Fig. (III. A. 2), with torroidal fields deflect them away from the direction of the beam and our apparatus.

The neutral component of the beam contains many types of neutral particles but after traveling approximately 450 feet to our detector, the only important components that have not decayed are K_L, neutrons, and photons, with most of the power being neutrons if no filtering is done. The photons originate for the most part from the rapid decay in the primary target of neutral pions which are copiously produced and decay to two photons. We filter the neutral beam to increase the relative photon component by passing it through 105 feet of liquid deuterium, the material with the greatest ratio between hadron absorption and photon absorption. This filter enhances the photon component over the neutron component by about a factor of 300 and yields a beam with 99% or better photon purity. The entire deuterium cryostat, which is actually two separate units, is subjected to a 9 kG magnetic field with additional magnets downstream of the filter.

Fig. (III. A. 1)

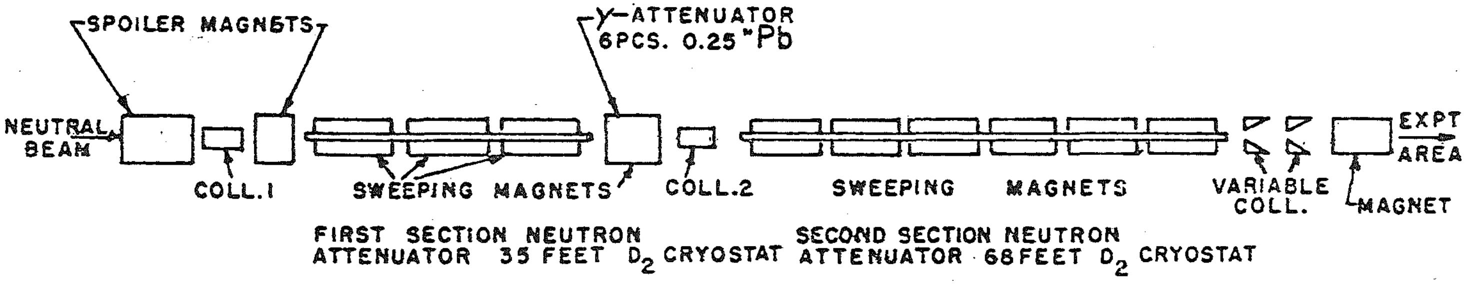

Schematic of Collimators and Deuterium System

Fig. (III. A. 2)

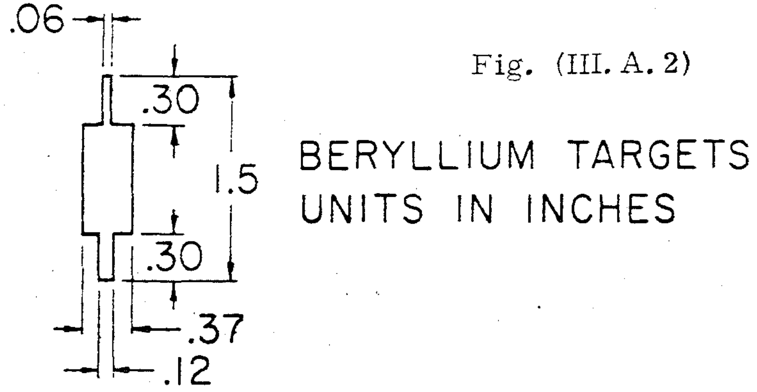

87A Production Targets

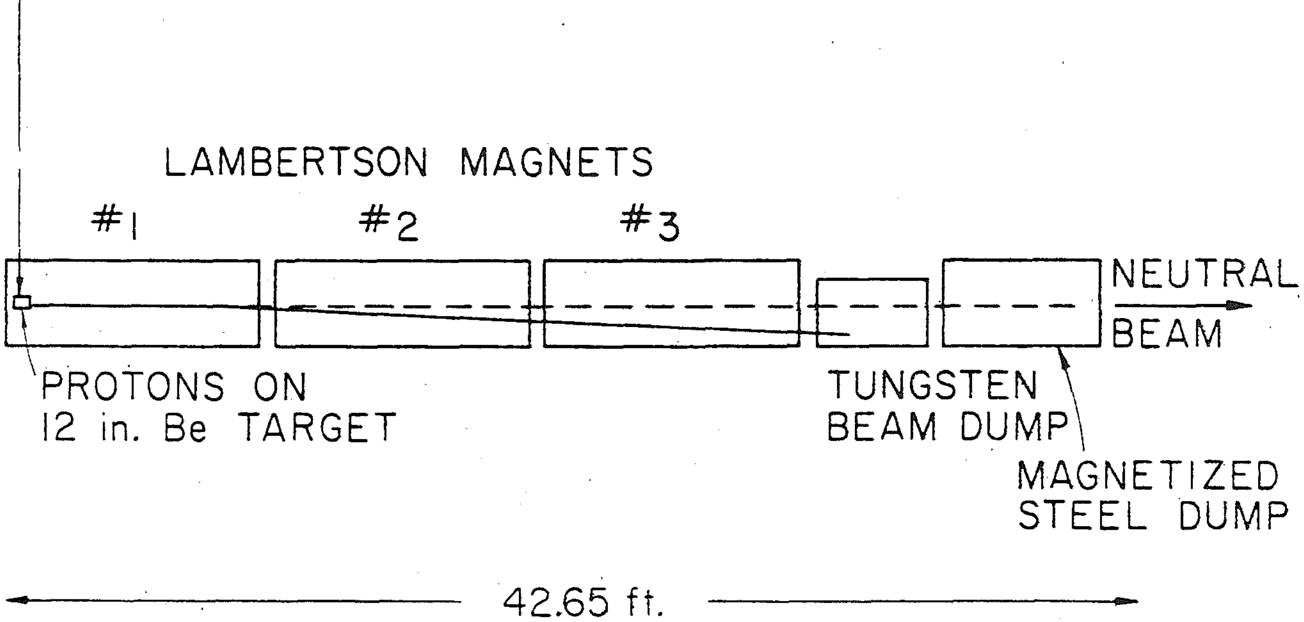

Target Box Side View

These magnets are vital to deflect charged particles produced as the beam is absorbed so the beam remains neutral, and to minimize bremsstrahlung by the Bethe-Heitler pairs, which would add an undesirable excess of low-energy photons to the beam.

The filter system has a number of apertures along it, but these are meant only to clean off beam halo except for the collimators marked COLL. 1 and COLL. 2 in Fig. (III. A. 2). These define the beam size and have five holes that can be used, each of which are matched such that the second collimator accepts a slightly larger solid angle than the first. These collimators are 6 inches of heavy-met (sintered tungsten) followed by 60 inches of steel and define a solid angle of 44×10^{-9} sr.

We do not discuss most of the beam-diagnostic devices in the proton beam and filter area; however, one set of devices is central to monitoring the quality of the photon beam. A secondary emission monitor (SEM) located just upstream of our primary target measures the proton-beam flux and a Wilson-type quantometer at the end of our apparatus measures the photon-beam power. (We shall discuss the quantameter in more detail later.) The proton-beam flux does not enter directly into any considerations about the experiment; however, if the SEM is compared to the integrated quantameter current (Q), a measure of the beam performance is obtained. An unusually low Q/SEM probably indicates mistuning of the beam; the muon background will be higher for a given photon intensity and the spectrum of photons could be altered. A simple example of these problems could be failure to squarely hit the primary target with the proton beam or a collimator misalignment. A more dangerous indication is a large Q/SEM. This almost always means that the deuterium system is not completely filled and the beam will have large hadron contaminations, and perhaps be too intense to allow our detectors to operate. An additional device in the photon beam allows us to check the purity of the beam. A γ-attenuator can be remotely ordered to place from 1 to 6 sheets of lead approximately one radiation length each, into the beam. The sheets are placed in a magnet for the same reason the deuterium system is. If the falloff of Q/SEM is exponential with increasing absorber, the beam is quite pure, but if a significant neutron contamination exists, the falloff will flatten as the lead is added and the photon component disappears, leaving the much slower attenuation of the neutrons to dominate. With the cryostat filled and the beam well tuned, no deviation from the photon absorption can be observed for 6 radiation lengths of lead. The photon spectrum as seen in the spectrometer is shown in Fig. (IV. C. 1) We discuss the determination of the spectrum in Section (III. D).

B. The Spectrometer

The spectrometer is shown schematically in Fig. (III. B. 1) and Fig. (III. B. 2). Not shown upstream of the spectrometer is the vacuum pipe which brings the beam into the pit and a remotely controlled 4% radiation length lead target (inside the vacuum) followed by a horizontal bending magnet. The spectrometer itself consists of a vertical bending magnet and five proportional wire chambers (PWC's). The magnet is a modified BM109 magnet, with a length of 72 inches, and an aperture of 24 inches vertically by 16 inches horizontal. The $\int B \cdot dl$ along the beam axis through the magnet is 595 MeV/c. In our analysis we use an $\int B \cdot dl$ from a field map evaluated at the track position at the center of the magnet.

The PWC's are of relatively standard construction, consisting of a series of alternating high voltage and signal wire planes spaced at 0.25-inch intervals on G-10 epoxy-glass frames and held rigidly in a sealed frame with mylar end

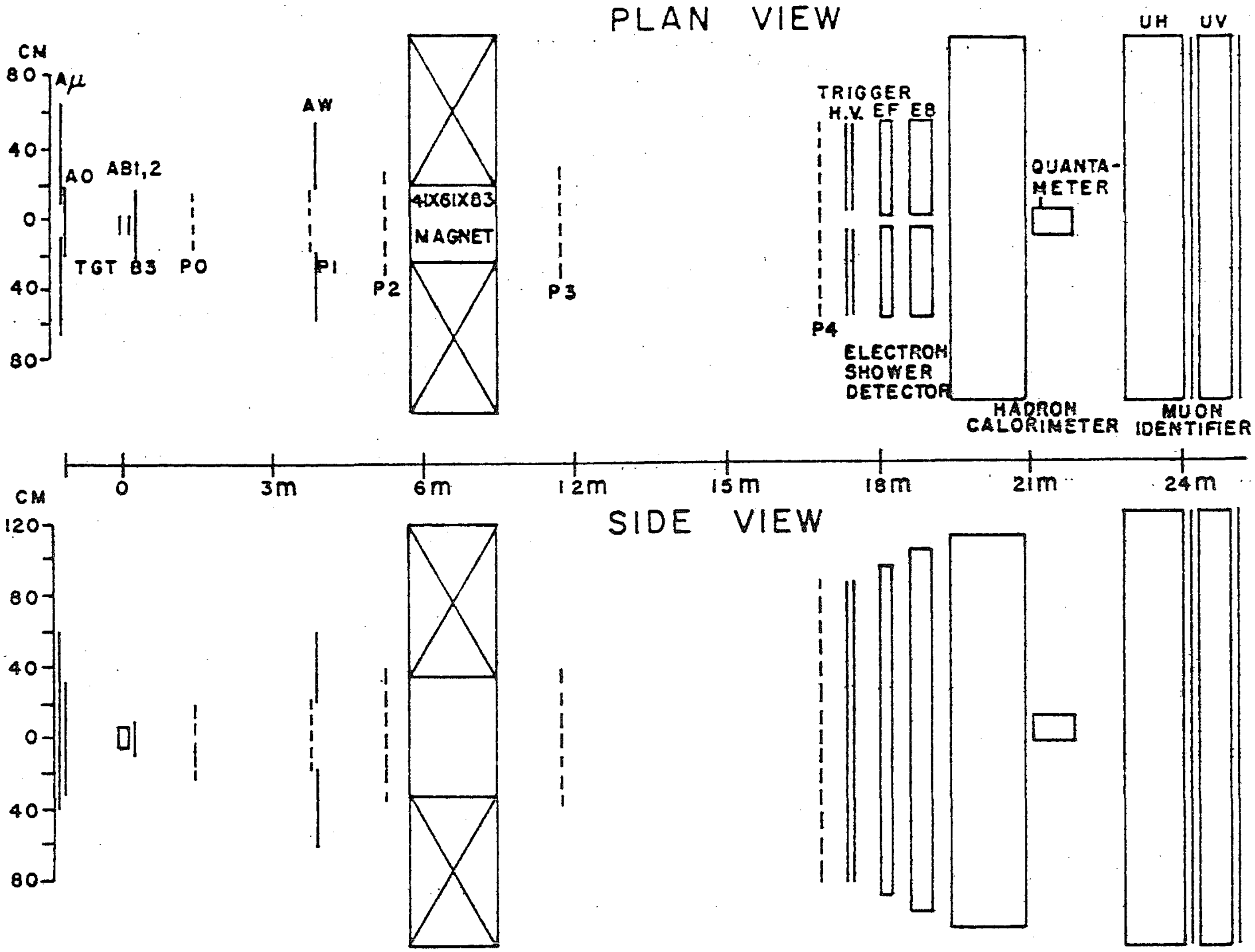

Fig. (III. B. 1) Views of magnetic spectrometer and particle identification system

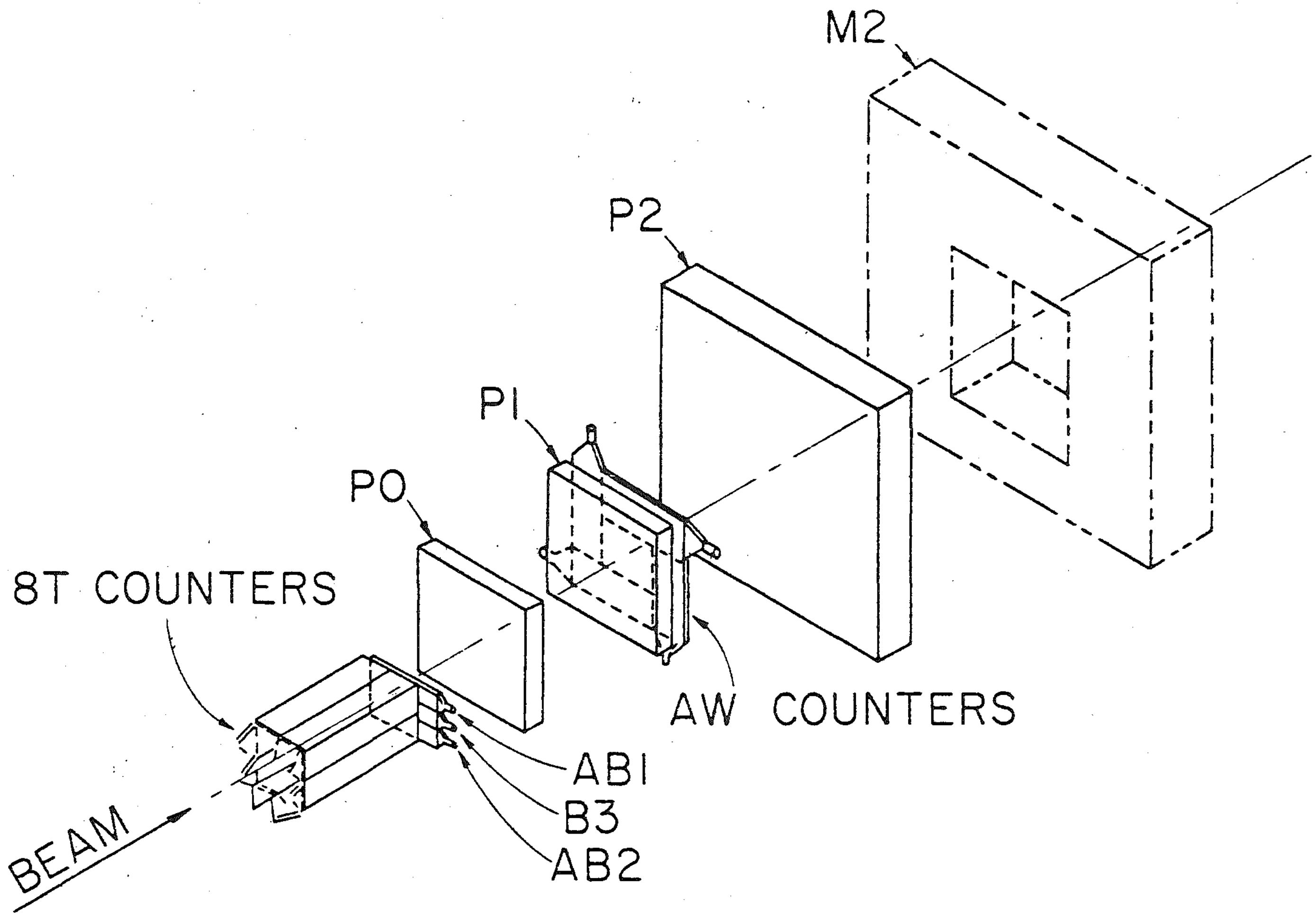

Fig. (III. B. 2) Upstream Proportional and Scintillation Counters (Schematic) windows. Thus each signal plane is 0.5 inch from its neighbor and each chamber holds 3 planes, labeled X, V, and U. The X wires are vertical and the U and V wires are about 11° from the horizontal, the actual angle being the arctangent of 0.2. The spacing between wires in a plane is 0.08 inches except for the X plane of P4 (the largest and last PWC) in which it is 0.12 inches. The chambers are arranged with 3 upstream (P0, P1, P2) and 2 downstream (P3, P4) of the analyzing magnet. P0 and P1 are 10 inches by 14 inches, P2 and P3 are 20 inches by 28 inches, and P4 is 40 inches by 60 inches. These measurements are the active area and the larger dimension is vertical. Figure (III. B. 3) is a schematic of a typical PWC. The momentum resolution of this system is given very approximately by $\Delta p/p = \pm 3.5\%$ at 100 GeV with $\Delta p/p$ directly proportional to the momentum. In our analysis the resolution is modeled in the Monte Carlo using the detailed structure of the apparatus. Helium bags placed between the chambers and in the magnet aperture reduce multiple scattering and beam interactions outside the target.

The PWC's are read out from the edges of the planes. Each signal wire is soldered to a copper strip leading out of the chamber to a connector on the edge of the plane. Amplifier cards connect into these plugs with each plug and card servicing 8 wires. The card contains electronics to amplify and discriminate the signal from its eight wires and send the discriminated signals as logic pulses up a ribbon cable to the electronics hut. Each ribbon cable contains 32 signal paths and services 4 amplifier cards. The amplifier cards also send out a signal if any wire on the card goes over threshold. These signals are combined on a trigger mixer card and sent up to the hut on a coaxial cable or on a ribbon cable if the plane is subdivided into a number of sections each a multiple of 8 wires wide. This information is used to form a PWC trigger requirement, see Section (III. J).

Fig. (III. B. 3) Schematic of a PWC. For clarity only a few of the trigger mixers, amplifier cards and signal wires are shown.

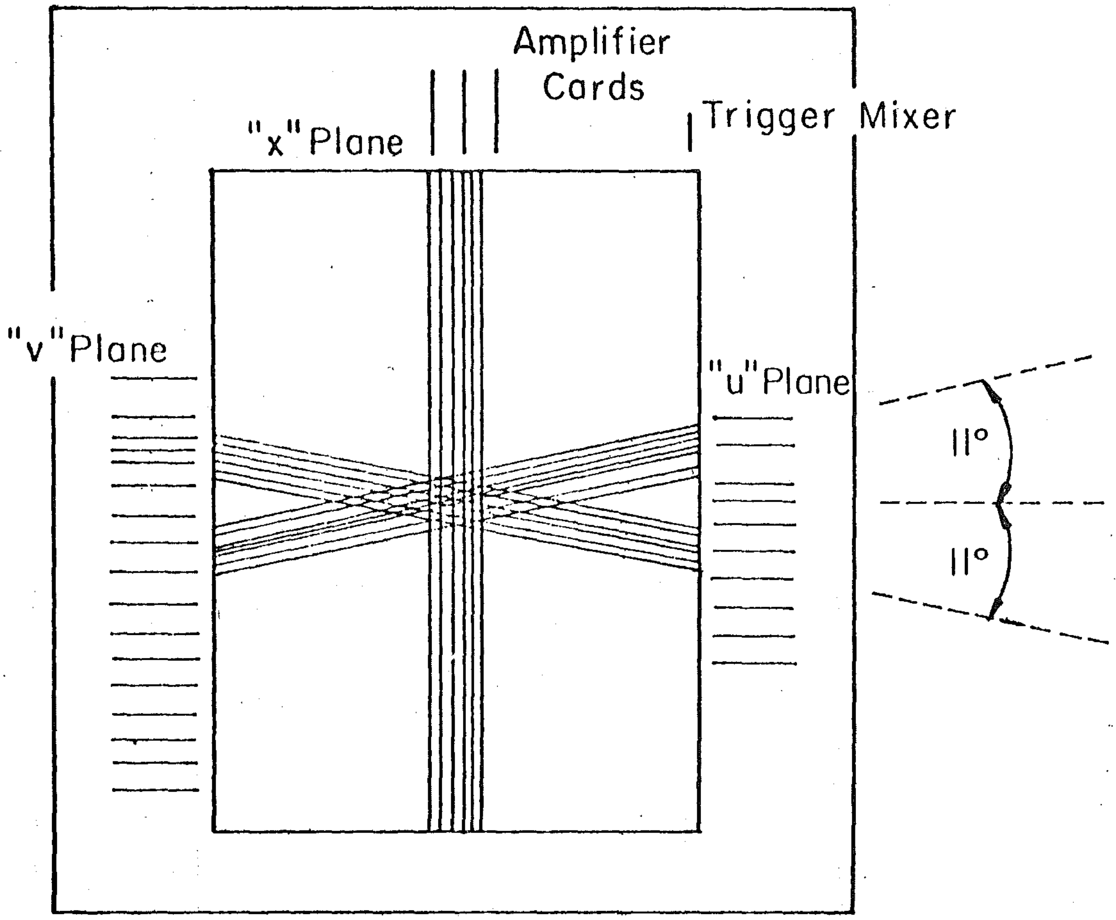

C. Scintillation Counters

The counters are all of conventional design, using 12-stage photomultipliers viewing plastic scintillator through lucite light pipes. Most of the counters use 1/4-inch scintillator, with the exception of A0 which uses 1/16 inch, because it is in the beam. The layout and dimensions of the counters are illustrated in Figs. (III. B. 2), (III. C. 1), and (III. C. 2). The counter array in Fig. (III. C. 1) is located about 10 inches upstream of the target to veto muons and upstream beam interactions. A0 is the counter in the middle. Notice that the trigger counters have a vertical gap. This gap allows the e^+e^- pairs (all very forward) to pass without generating a trigger. This gap limits our acceptance of high energy, low mass states produced at small angles, simply because the decay products do not have sufficient transverse momentum to reach the trigger counters.

All counters in high rate environments are provided with "after burners." This means that external power supplies are added to stabilize the voltage on the last few dynodes of the photomultipliers so that the resistor divider that normally supplies these voltages will not "sag" when large currents are drawn.

Each counter has been plateaued and tested for efficiency before installation and the trigger counters particularly are monitored for efficiency in special runs where we trigger from upstream muons. All counters have test efficiencies of 99% or better. As a further attempt to monitor the counter performances, the trigger counters have their final dynode signals sent up to the hut as well as their anode signals. These dynode signals are digitized for each event and monitored on-line to check for shifts in behavior. During periods between running when no beam is available, Co^{60} sources are placed on all the counters and rates taken and recorded as an additional test of long-term stability.

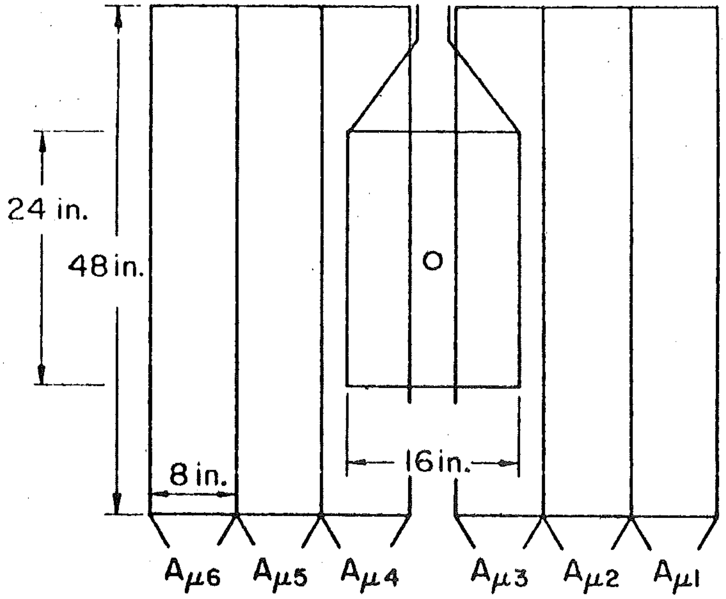

Fig. (III. C. 1) Upstream View of Muon Anti Counters

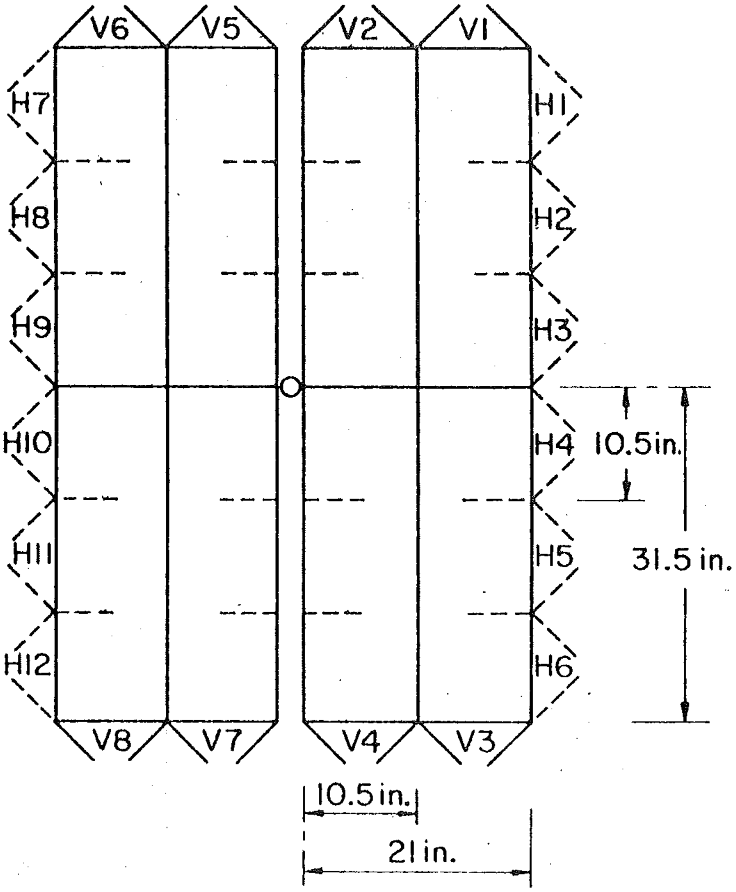

Fig. (III. C. 2) Downstream View of Trigger Counters

D. The Spectrum Measurement

The photon spectrum is measured using the spectrometer and the trigger counters just described. Bethe-Heitler e^+e^- pairs of opening angle ≤ 2 mrad are used for the spectrum measurement. These events are obtained by removing our usual target and moving in the 4% radiation length lead target mentioned earlier. The upstream horizontal bending magnet bends the pairs out into the trigger counters, and events are taken if at least 3 counters are on in the trigger counter system, not all H's or all V's, and 2 out of 3 planes in P1 have a trigger mixer output. The zero-degree pairs have a unique signature in the system and essentially no background. Absolute normalization of the spectrum is not necessary so only an acceptance correction must be made to obtain an unnormalized spectrum.

Only one real difficulty presents itself. No single setting of the magnet currents in M1 and M2 (the first and second magnets) will allow the entire energy range to be accepted into the spectrometer. Either low-energy pairs are bent out of the system or high-energy pairs do not get bent into the trigger counters from the gap, or both. This means that the spectrum must be measured in two runs with different magnet settings, then the two halves of the spectrum must be matched in relative normalization. This is done using the same method of deadtime correction, etc., as is used in Chapter IV for our analysis and the quantameter Q, or, alternately, the SEM. The two pieces are adjusted to have the same relative normalization and then a complete spectrum is available.

E. The Particle Identification System

The particle identification system is shown schematically in Fig. (III. E. 1) and its place in the apparatus can be seen by referring to Fig. (III. B. 1). This

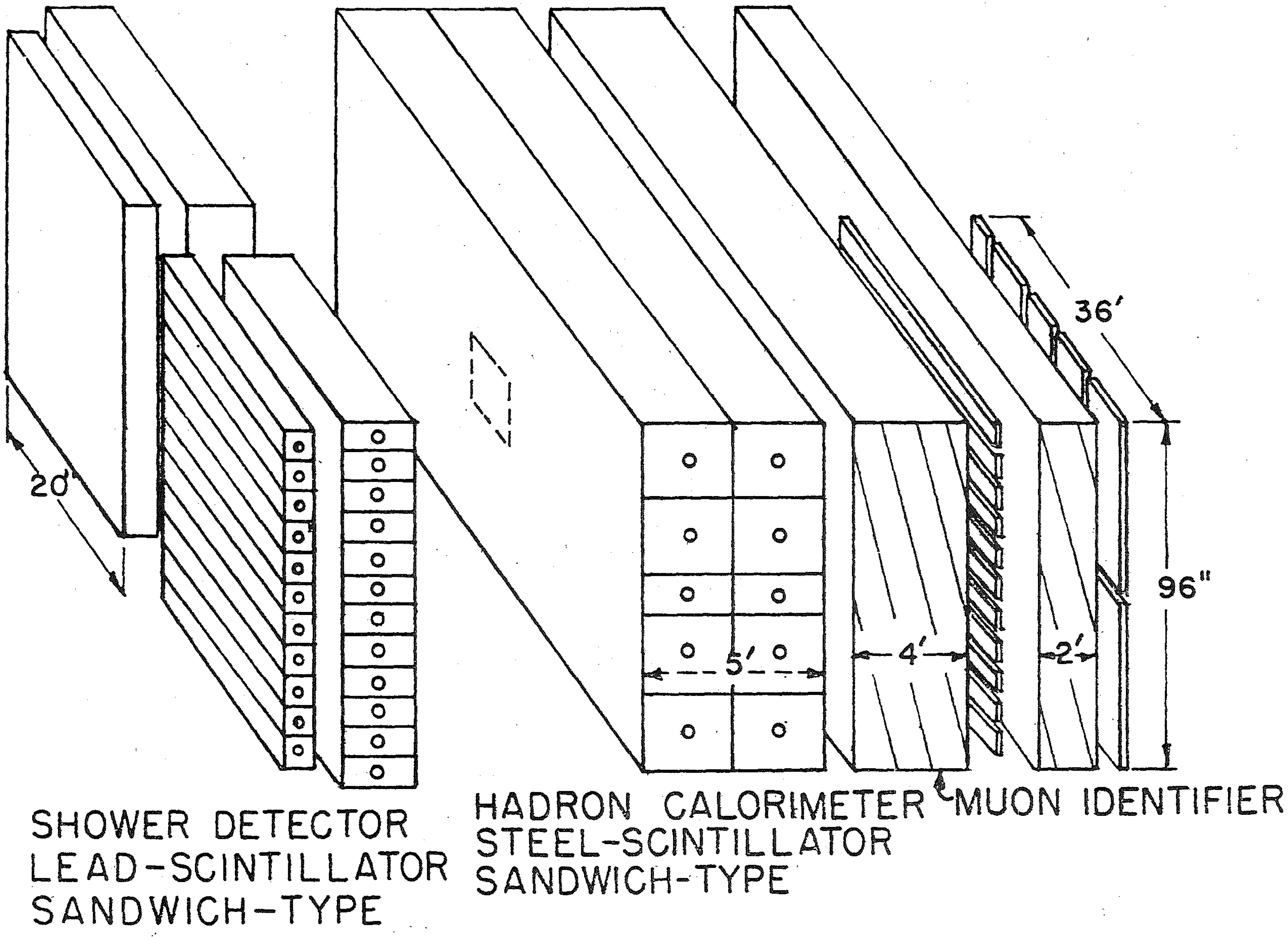

Fig. (III. E. 1) Schematic of Particle Identification System

system follows the H and V trigger counters which in turn are directly behind P4, the last PWC in the spectrometer. Not shown in the figure is a vertical lead column that fills the vertical gap directly behind the shower counters. This gap is left open vertically 6 inches to allow the beam to pass through. Also hidden from view is the quantameter, shown in Fig. (III. B. 1). A six-inch square hole goes all the way through the hadron calorimeter (HC) to allow the beam to reach the quantameter unobstructed. The muon identification system plays no role in our analysis whatsoever.

As far as this experiment is concerned, the only important part of the particle identification system is the HC. The shower detector system contains 22 radiation lengths of lead which serve the purpose of shielding the HC from electromagnetic energy (electrons, positrons, and photons). This is only slightly over one nuclear absorption length so that most of the energy of a hadron will enter the HC, whose purpose it is to measure the amount of energy carried by hadrons from an interaction. The HC is illustrated in Figs. (III. E. 2) and (III. E. 3) and consists basically of a sandwich of lead and plastic scintillator, with the 58AVP photomultiplier tubes (5 inch photocathode diameter) viewing each set of 12 scintillator leaves. There are 20 modules in the HC altogether but as far as we are concerned the front 10 are the only ones of interest. Notice the center counters, labeled 3 and 8, are only 6 inches tall and are slid out 3 inches each to leave the 6× 6-inch hole in the steel sheets unobstructed.

To assure reasonable light-gathering efficiency from the large scintillator leaves, they are wrapped in aluminum foil under a PVC tape light shield, as is standard procedure with large counters. In addition, a yellow filter (Wratten # 4) is placed over the phototube face. This serves to filter out the blue and near UV light that has the most rapid absorption in the scintillator and hence gives the

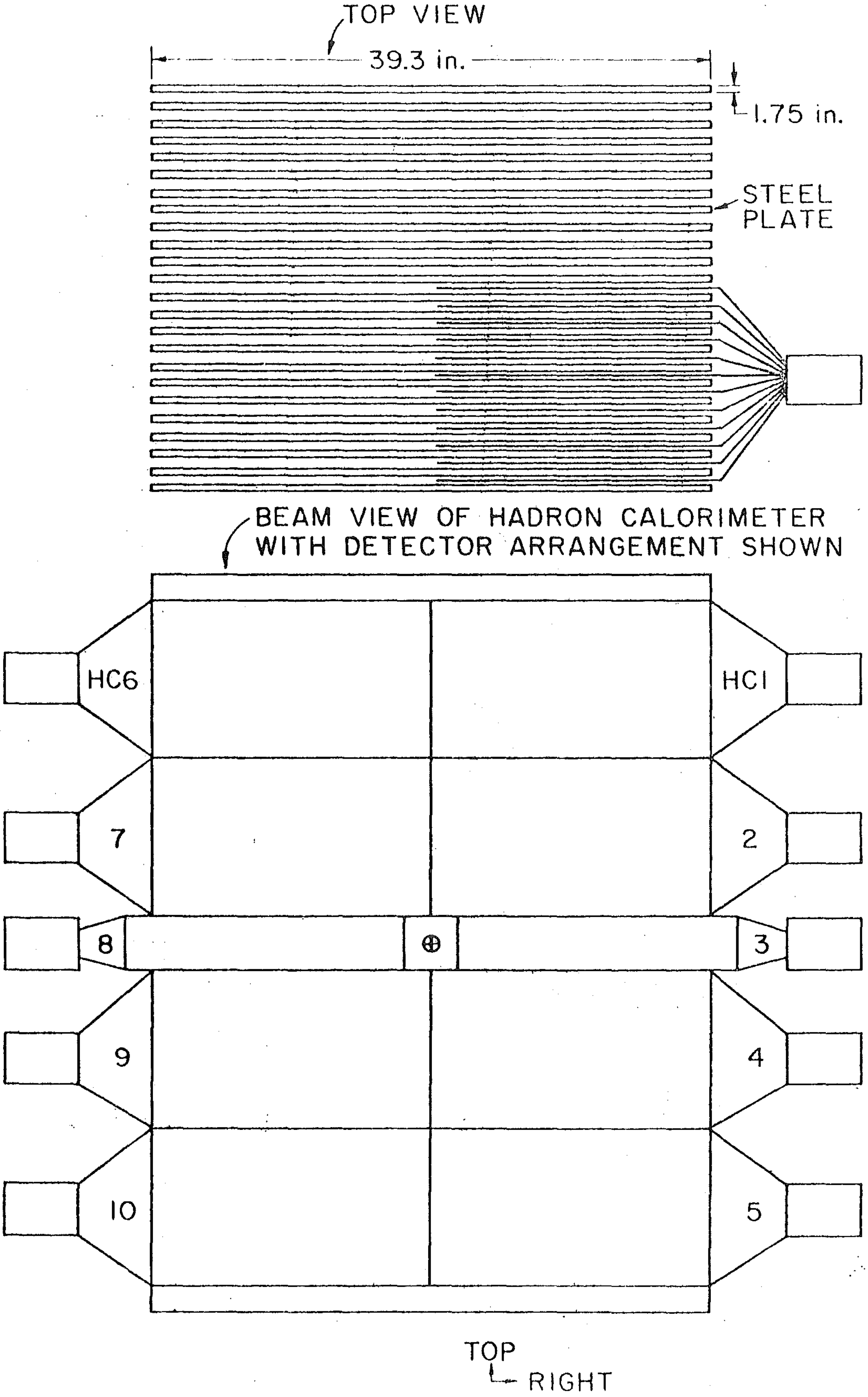

Fig. (III. E. 2) Hadron Calorimeter

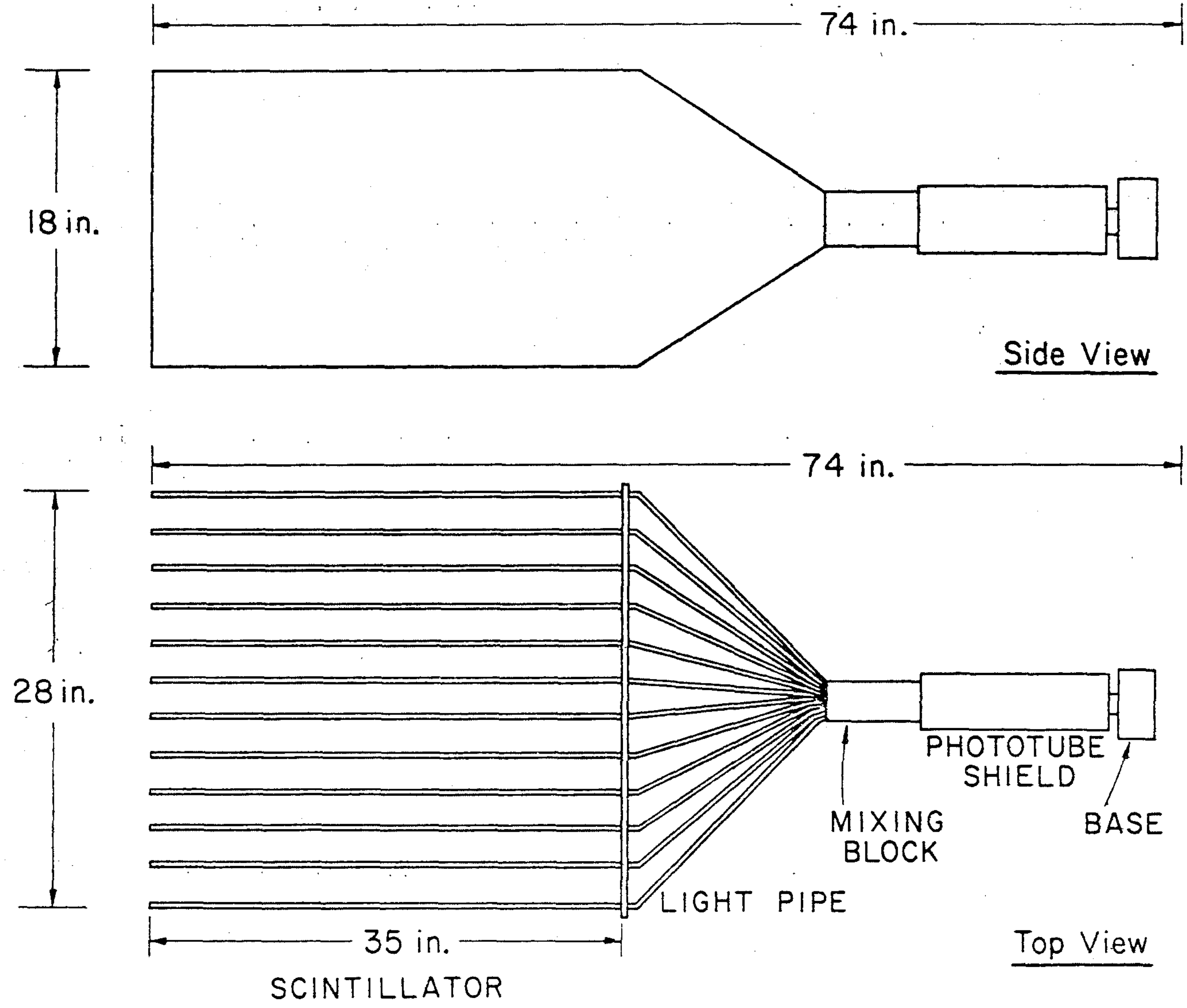

Fig. (III. E. 3) Details of Large Hadron Calorimeter Counter largest contribution to a position dependence of light collection. The resolution of these devices, when used two deep, is about 30% FWHM for 50-GeV pions [Knauer, 1975]. As will become clear, we do not use them in this analysis in a way that exploits their intrinsic resolution.

The use made of the HC system is only in the trigger. All ten of the front HC counter final dynode signals are added together and discriminated by pulse height to form an HC energy requirement, which is adjusted to give an estimated energy cut in the neighborhood of 20 GeV. Several effects mitigate against this arrangement having a sharp energy threshold. The lead in the shower detector absorbs a variable amount of energy. Using only one module in depth in the HC allows large variations in the amount of energy escaping the rear of the module. The signal we trigger on is pulse height and we know the energy in the counter to be related to pulse area. This is aggravated by timing jitter in the cases where more than one module signal must be superimposed (this happens for most events). Finally, the gains of all individual modules should be the same, but in practice it is difficult to check their gain and they are not adjusted equally. This means that the system gives variations in measured energy approaching 50% depending on the counter modules hit by the hadrons in an event. We have probably not exhausted the sources of uncertainty in the use of the HC in an energy threshold trigger, but they add up to give a resolution that is probably 100% FWHM in the turn-on region of 20-30 GeV.

The foregoing discussion suggests an unjustified mistrust in the use of the HC in the trigger. If we go far enough above the HC threshold and require the tracks in an event to point to the HC, eventually the efficiency of the trigger should rise and our price is the unusability of the events triggered in the energy region where the HC efficiency is unknown and varying. As we shall see in

Section IV, a comparison of data taken with and without the HC trigger indicates 95% efficiency for the HC above 50 GeV. In return for losing the use of accepted events below that energy, we are paid back by a relatively large number of events from the better acceptance, high energy part of the photon spectrum and a rejection of false triggers from the e^+e^- pairs which can dilute the good events on our tapes.

F. The Targets

The target properties are listed in Section IV [Table (IV. F. 2)]. The targets are approximately 2 inches wide and 3 inches high, allowing some room for error in positioning without allowing any beam to sneak past them. They sit on a platform that can be remotely moved vertically out of the beam. Target changing is not frequent and is done by hand, using guides on the platform to aid positioning. Checks of vertex distributions for $\rho \rightarrow \pi^+\pi^-$ events verify that in the runs we use the targets are not significantly misaligned.

G. The Quantameter

The beam power is integrated for each spill in a Wilson-type quantameter. The quantameter absorbs the beam and is placed after all the active parts of the detector. The performance and design is discussed by [Harris and Yount, 1974], based on tests of our present quantameter in an electron beam at SLAC.

The quantameter can be thought of as a type of calorimeter. It consists of 44 plates of copper, each 9/16-in. thick separated by a layer of pure hydrogen gas. The gas is under a 1 kV potential and the ionization is collected when a photon or electron showers in the device. This current is integrated over the spill (one second) on a precision current integrator and is encoded and read into the computer. When properly scaled this number is the charge collected, in

Coulombs, which is proportional to the integrated beam power. The experimentally determined conversion factor is 416.1 ions/GeV. Alternately we can use the number of integral charges in the Coulomb to write this as 1.500×10^{16} GeV/Coulomb.

The quantameter is a continuously integrating device and due to the ionization collection time and the difficulty of gateing the precision current integrator, the quantameter sees the entire spill. Thus photons coming when the apparatus cannot accept a trigger are included in the quantameter response and will indicate that we have more beam than was seen by the rest of the detector as accepted triggers. Too much beam for a given number of events and a given target thickness translates into a cross section that is systematically low. Thus we correct for this effect by scaling the number of interactions of certain types in our apparatus, both when the detector is ready to accept a trigger and when it is not. The fraction of interactions occurring when the apparatus is "live" (ready to accept a trigger) must then be multiplied times the quantameter reading to get the amount of beam power we use to normalize our cross sections. This correction is called both a "livetime correction" and a "deadtime correction" by various people who think about the problem in slightly different ways. The sources of the deadtimes will be shown in the discussion of our electronics and the livetime fraction is calculated explicitly in Section (IV. E). We want to emphasize that what occurs during times when the apparatus is dead is truly unknowable, only estimates based on counting rates and the assumption that the interactions occur similarly whether the detector is "live" or not can be used to estimate the livetime fraction. This introduces a systematic error that can lower cross-section results and is of unknown magnitude. Some of our results are independent of overall normalization. For other results we will quote ratios of numbers for the ρ' and ρ as have some previous workers. This exploits the fact that with both ρ and ρ' data taken in the same apparatus and at the same time, systematic normalization errors cancel out when ratios are taken.

H. Trigger Electronics

In discussing the electronics we emphasize the philosophy of the experimental design with sufficient detail to give an appreciation of its operation, such as event-rate capability and deadtime generation. Figure (III. H. 1), which is an abbreviated schematic of the triggering and data acquisition system, may be of some help in following our discussion of the electronics. The type of events we are trying to collect here have 2 or 4 charged particles, all of which fall inside our spectrometer. We wish to avoid triggering on the copiously produced Bethe-Heitler e^+e^- pairs or the muons and debris from upstream interactions in our beam line. Beyond this we have designed a system that does trigger decisions and data read out quickly to keep deadtime small, but which still allows easy implementation of new triggers. To implement the trigger we require at least 2 tracks outside the beam using PWC information and the H, V trigger counter hodoscope located downstream of the spectrometer. Veto counters (called "anti" or A) are positioned to exclude events, with tracks outside the spectrometer or with muons from upstream sources. The "dc" feature of the trigger electronics allows easy trigger modifications without re-timing and allows us to conveniently scale trigger rates during event readout to monitor deadtime. In order to achieve high data transfer rates during event readout, this process is handled by an automatic system (ACE) using its own data memory with no intervention from the on-line computer. The system can read-in about 200 events during a one-second beam spill, taking about 150 μsec for each event. The trigger decision time is

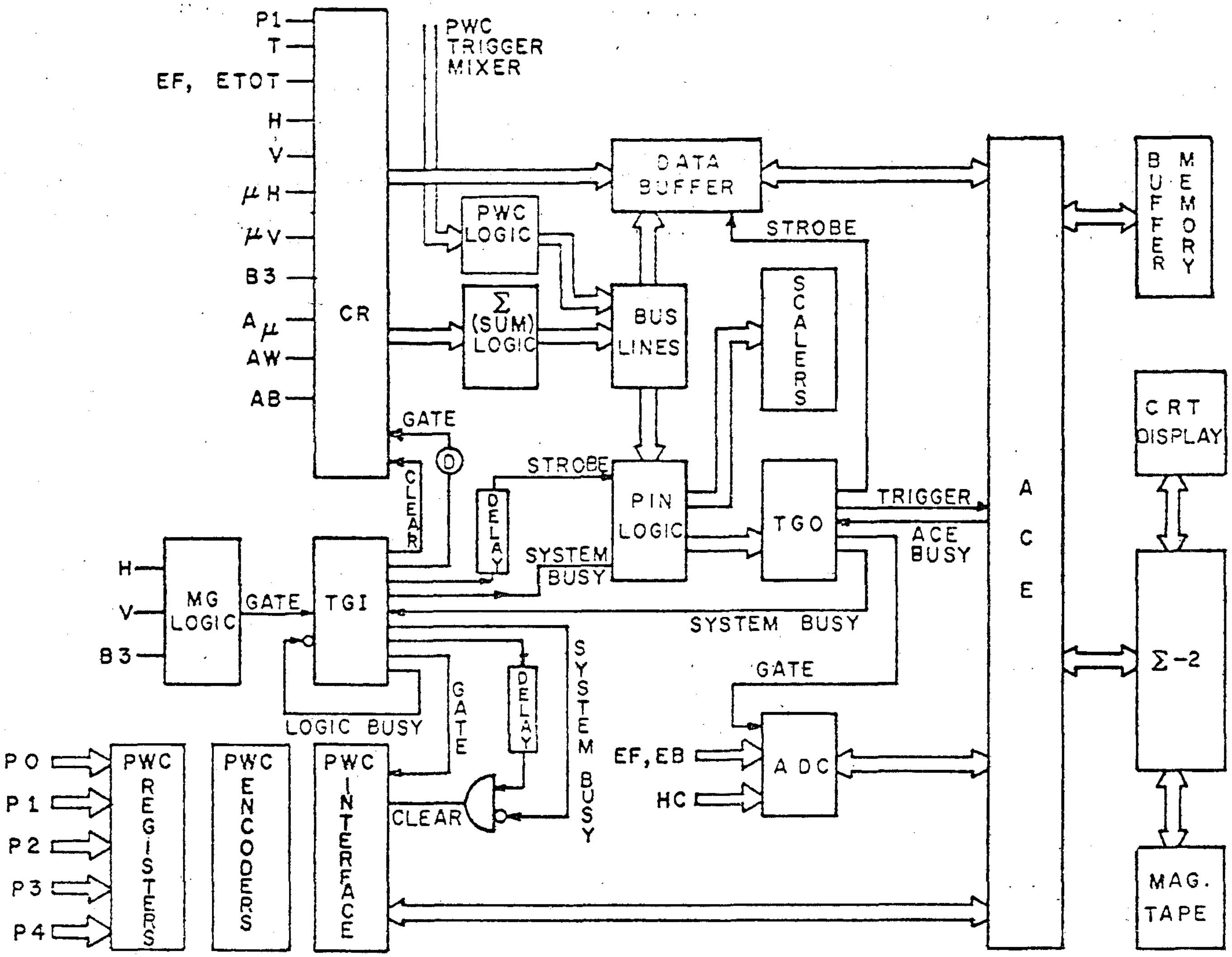

Fig. (III. H. 1) Block diagram of electronics, blocked by function.

300 nsec. Chapter IV does not require a detailed knowledge of our electronics except for the deadtime correction. For readers desiring a more detailed understanding of the electronics a "guided tour" style discussion follows, beginning with the logic gate (LG), a high rate pretrigger for the logic.

The trigger hodoscope (H and V counters) have a short cable run to the hut and are discriminated (as are all scintillation counters) and formed into a so-called logic gate (LG). The B3 counter is not in the LG. To generate a LG a minimum of 3 counters are required corresponding to the minimum number that would be hit by a well separated 2-track event. Not all the geometrical information is used as can be seen by looking at Fig. (III. C. 2). A LG is generated if > 1 H and > 0 V counters fire or alternately if > 0 H and > 1 V fire. In the argot of the experiment this is called $(L\times R) > 1$. The time coincidence required for the signals forming this LG must be within about a 15 nsec window, thus this LG is sensitive to the highest possible rate of 50 mHz from the 20 nsec rf beam structure. This LG signal is scaled and the total read by the computer after each beam pulse. Quite appropriately the LG is used to gate the rest of the logic. If the logic is busy processing a previous LG then the LG is ignored. The number of LG's accepted by the logic is scaled and read by the computer after each beam pulse.

Let us assume that the logic is not busy and follow what happens when a LG arrives. First, several gate signals are sent out to latch data into registers. The latch register for all scintillation counters is part of the logic rack and is a total of 8 16-bit words (enough for 128 counters) called coincidence registers (CR). The CR's are cleared and then a gate is sent that opens them to input data. The counters have all been sent through sufficient cable that in-time signals will arrive simultaneously to be gated in. The gate plus input pulse width to the CR's is about 15 nsec so that the resolving time of the CR's is smaller than the 20 nsec beam structure. The CR's are gated in groups of 8 so that if a group of counters arrives late the gate to the CR for that group can be delayed, instead of delaying all counters to arrive when the latest ones do. Information other than scintillation counts is used in the trigger and all of it except for part of the PWC trigger mixer information is latched into the CR's.

The other gates sent out when a LG enters the logic are for the PWC system. Just as counter signals are in transit in their cables while the LG is being generated, so are the PWC signals "stored" in the cable delay coming up to the hut. Each ribbon cable carrying 32 channels connects to a register card containing 32 latches which strobe in the data on the cable when the PWC gate arrives. Due to the intrinsic time resolution of the PWC its gate cannot positively resolve one 20 nsec beam interval so that in principle stale hits from earlier intersections or room muons from upstream can be recorded. This effect has been observed but is not believed to be important for the data we analyze here. At the same time that the PWC gate is generated, a PWC clear pulse is started and is delayed such that the clear is vetoed if the logic generates a trigger.

One other signal is started at this time and is electronically delayed by 300 nsec. This is the strobe signal that forces the logic to emit a trigger if the conditions are satisfied. When we encounter it again we will call it the STROBE. This 300 nsec during which the logic is making up its mind is the logic deadtime associated with any LG generated when the logic is not already busy. The trigger logic is dc. This means that no timing is required in connecting it up so that changes are easy to make and cable lengths are not critical in most places.

The dc feature of the logic is accomplished in the following way. The CR outputs latch up the counter information and provide a steady output. These outputs are combined in various logic elements or perhaps for some cases such as the HC threshold signal just used immediately. We wait for these signals to ripple through any logic elements until the outputs settle down. In this way we form up to 16 signals from individual CR bits or from logical combinations and require that the formation delay be short enough that they have all stabilized 300 nsec after the LG was received and the STROBE occurs. These 16 signals are placed on a 16-channel parallel bus into which "pin logic" cards are connected. Up to 16 pin logic cards can be accommodated on the bus.

Each pin logic card sees the 16 logic levels on the bus lines and compares the bus lines to 16 requirements set by jumper wires inside the card. Each of the 16 lines can be compared to "on," "off," and "don't care." A pin logic is satisfied if the bus lines agree bit by bit with its internal requirements on the bits not set to "don't care." After the pin logic cards have the bus line signals for the few nanoseconds required for them to perform the compare the system is ready for the STROBE, which is sent to all pin logic cards. Any card that is satisfied and is not prescaled passes the STROBE out into one of 16 inputs to a "trigger store" register which latches a bit for each pin logic satisfied and passes on the STROBE to the output gate generator. If this occurs during a time that the readout system is not busy we call this a "trigger" and the event that caused it will be read out and put on magnetic tape to be analyzed. The output gate generator issues pulses which block the clear of the PWC register cards and gate the ADC's (analogue-to-digital converters) to receive signals which have been traveling in long cables up to the hut during the logic-decision time.

A number of other things happen at the output end of the logic if a trigger is generated and the reading of a previous event is not in progress so that the "system" is not busy. A signal is sent to the event readout system to start the readout process. A signal is sent to the CR buffer to store 10 16-bit words, which come to the buffer in parallel from various places in the logic rack. The first word in the buffer is just the 16 bus lines, the next 8 words are the CR's themselves, and the last word is the 16 bits of trigger-store information (TSB). The order of bits in the trigger store register associated with a pin logic card is the numbering scheme we use for distinguishing pin logic requirements. Thus, after a STROBE which one or more pin logic cards has passed to the output gate generator during a period when the readout system is ready, both the pin logic (or logics) responsible for the trigger and the bus lines seen by the pin logics as well as the CR's are saved in the CR buffer. At this point the readout system starts to read the event out.

Suppose a readout operation is in progress when a LG enters the logic system. A "system busy" signal is sent out by the readout system when it is working on an event, and this is distributed in the logic rack. In this case no gate is sent to the PWC registers because they contain information that is being read out from the event in progress. The system then behaves normally until the pin logic level. We did not mention previously that each pin logic card is connected to two scalars that are read at the end of each beam spill. One of these scalars counts all accepted STROBES for the pin logic card and the other counts only STROBES accepted when the system is not busy. These scalars are used in the deadtime correction [see Eq. (IV. E. 8)] . No gate is sent to the ADC's and the CR buffer is left undisturbed. Thus the logic rack can accept LG's and cycle away, scaling the number of pin logics that pass the logic requirement when the readout is in progress, thus monitoring what is going on during readout (system) deadtime.

We have one remaining feature of the pin logic cards to explain. Each pin logic card can be connected to a prescalar module that blocks the STROBE output from the card unless the prescalar has counted up to a limit that is externally set (limited to a power of 2). We call this factor PS for prescale. Thus if PS is 512 for TSB #14 only one accepted event in 512 will be able to initiate a trigger. This PS factor does not affect the scalars connected to the pin logic card; they count all accepted STROBE's, regardless of whether the STROBE is then blocked by the prescale. The prescale is used to reduce the fraction of triggers from a pin logic that goes at a very high rate because its requirements are loose. These triggers can be useful but they are not allowed to fill the tapes to the exclusion of lower rate but more interesting triggers.

J. Trigger Definition

Triggers are defined by making logical combinations of CR outputs to form bus lines, then a pin logic card is set to test for some combination of the defined bus lines. There are two extensions to this method, one of which is the possibility of adding information at the bus line level that does not originate in the CR's. The PWC trigger for P2 and P3 is handled in this way and we describe it momentarily. The other complication is the existence of two forms of output from the CR's. The CR's are implemented in 8-bit (or channel) modules and we use two different types. Both have an 8-bit output used to load the CR buffer when a trigger is accepted, however, the outputs to be used in the logic are different. One type of CR just has 8 logic outputs, one for each counter connected to it. The other type of CR has two outputs with 4 counters feeding each one. This type of output is a multilevel output able to represent 0 to 4 as five increasing voltage levels. This multilevel output is only accepted by a special logic module called a sum (Σ) module. Up to 8 multilevel inputs can go to a simple Σ module, representing up to 32 counters. The Σ module gives ordinary (on-off) logic outputs through different spigots producing ($=0$), ($=1$), ($=2$), (>0), (>1), and (>2) outputs. The Σ

logic outputs have been used to produce some fairly sophisticated hodoscope triggers that we do not discuss here.

We now define the PWC logic formed from trigger mixer outputs. These outputs are brought up to the hut with one signal from each of the 3 planes of P1 (the second PWC in the spectrometer). Using standard logic we form a requirement that at least 2 of the 3 planes of P1 must have a signal. We call this P1(2/3) and put it into a CR. The trigger mixer outputs from P2 and P3 (PWC's that bracket the magnet M2) are subdivided into bands in each plane and the resulting signals are brought up to the hut on a 32-channel PWC ribbon (flat) cable. The cables go to slightly modified PWC register cards where the signals are stored by a separately timed gate, derived from the LG signal. Table (III.J.1) gives the number of 8 wire groups that compose each of the bands in P2 and P3. Note that the center of each plane is between bands 4 and 5 and that the subdivision is symmetrical. The PWC register card holding the latched trigger mixer information feeds directly to a logic card that produces the following logic outputs: $(>0)^3$, meaning > 0 bands on in all 3 planes; $(>1)^2$, meaning > 1 bands on in at least 2 planes, (XR), meaning at least one band on in the right of the X plane; and

Table (III.J.1). Plane Subdivision Scheme in PWC's P2 and P3 Used to Form Trigger Mixer Signals. The Number of 8 Wire Groups in Each Band Is Given. NC Means "Not Connected."

	NC	1	2	3	4	5	6	7	8	NC
P2 X	4	6	4	1	1	1	1	4	6	4
P2 U, V	5	12	4	2	1	1	2	4	12	5
P3 X	-	8	6	1	1	1	1	6	8	-
P3 U, V	-	12	6	4	2	2	4	6	12	-

(XL), for the left of the X plane. (XL) and (XR) do not include bands 4 and 5 so as not to trigger on particles that stay in the beam region. Using simple "and" (·) and "or" (+) gates we then form the following requirement.

$$\mathrm{PWC}(\mathrm{P2},\ \mathrm{P3}) = \left[(>1)_{\mathrm{P2}}^{2} \cdot (>1)_{\mathrm{P3}}^{2}\right] \cdot \left[(\mathrm{XR})_{\mathrm{P2}} \cdot (\mathrm{XR})_{\mathrm{P3}} + (\mathrm{XL})_{\mathrm{P2}} \cdot (\mathrm{XL})_{\mathrm{P3}}\right] . \qquad (\mathrm{III.J.1})$$

This logic signal stabilizes within the 300 nsec allowed to put it into the logic as a bus line. It is "dc" because the two special PWC register cards have latched the trigger mixer data. This logic counts the number of bands that have hits and two or more tracks in one band still only count as one hit. For this reason, we model the behavior of this trigger exactly in our analysis to guarantee that the tracks in the data and Monte Carlo both satisfy the trigger.

We now define the bus lines used in our triggers.

(a) Bus line #2 has the 4 AW counters surrounding P1 and the 2 AB counters above and below B3 in one Σ module. If any of these counters fire, this line is on.

(b) Bus line #4 is PWC (2,3) as defined in Eq. (III.J.1). Basically, this requires 2 tracks in the chambers, with at least one out of the beam region.

(c) Bus line #15 is P1(2/3).

(d) Bus line #16 is $\mathrm{A0} + \mathrm{A}_{\mathrm{u}}\ (>2)$. If the A0 beam counter fires or if more than 2 of the halo counters fire this line is on.

We have taken data with 3 triggers, but the analysis uses only the trigger associated with trigger store #14 (TSB #14). This is defined by requiring bus #2 off, bus #4 on, bus #15 on, and bus #16 off. This is a so-called "diffractive" trigger. This is only used to mean that by vetoing on bus line #2 we have required that most of the events have tracks confined to our spectrometer aperture.

K. Data Collection System

We write our data on 800 BPI 9-track magnetic tape. One run takes about an hour of "wall time" and fills a 2400 foot tape. In this time we collect about 50 K events from approximately 350 beam spills, each of one second duration. Thus we accept 125 to 200 events per second while we are taking data. The computer used in the electronics hut is a Xerox (SDS) Sigma-2. It has 16 K of core memory, 8 external interrupts, a scope display for plots and text and a 3/4 megabyte fixed head disk (RAD). The computer reads the scalars after each spill, and writes all scalars and events on the data tape, but paradoxically has no part in event read-in! The computer performs a number of diagnostic and house-keeping functions and provides a range of test systems and outputs which we do not discuss because they are not in the direct line of data taking.

The data are collected through a 16-bit parallel digital communications system consisting of "black bins" (bins) and a multiplexer (multi). Each bin is located at the end of a cable branch from the multi. The multi is at the center of the system and has a number of devices it can communicate with. The multi communicates with the following devices:

(a) Sigma-2 computer via direct CPU access

(b) Black bins

(c) ACE controller (really a part of the multi)

(d) Address bin

(e) Buffer memory bin (32 K × 16 bit)

ACE is the control unit for automatic event read out. The system would be very difficult to explain in detail so we describe its operation in general terms.

Before the spill starts the Sigma-2 receives an interrupt that warns it to initialize various devices in the system by communicating through the multi to the bins. Its last act is to put ACE in control of the multi and from that point until the spill is over the Sigma-2 is free to do such things as analyze events saved on the RAD from previous spills or format histograms for the display scope. When the spill starts, a trigger will eventually be generated and the signal will be sent to the multi to start ACE. ACE begins to read in the event by getting addresses from the address bin and accessing the data located at that address. The address bin has a series of modules with switches that define the address of the various parts of the event. The address is a bin number and slot within a bin. Each bin has 31 slots, with 2 addresses per slot, and there are 4 bins in the system besides the two dedicated to addresses and memory. Thus the address bin provides in sequence the addresses in the system of the scalars and special interface modules from which the event can be read. As each word is accessed, it is stored in a 32K× 16 bit buffer memory and a pointer is kept for the next open word in the memory. The word access is less than 1 μsec which is 2-5 times faster than most CAMAC systems achieve in practice. This means that for a given amount of information in an event, the deadtime is 2-5 times less than other systems in common use. At the end of an event an entry is made in a table in the buffer memory marking the position of the event. The map thus formed is at one end of the memory and the events are stacked in from the other. If the two meet, a flag is set and the remaining data are dumped to avoid overwriting the event map.

The length of an event is at least 102 words, this being mostly CR's and ADC's. A clean two-track event would produce 30 hits in the PWC's (2 in each of

15 planes). Thus the event length, for a $\rho \rightarrow \pi^+\pi^-$ for example, is about 132 words. Clearly event lengths vary depending on how many tracks enter the various PWC's. When the event is read, the CR's are read first, then the PWC's. The PWC's are read through a special system with an "encoder" for each plane of register cards. The result is a 16-bit word for each hit wire containing the plane number and wire number. Two "adjacency" bits allow up to 4 adjacent hit wires to be combined into one address; this is a switch selectable hardware option. The ADC's are read last in the event so they will have time to digitize. They digitize using a 50 mHz clock and by the time the first one is read they have had enough time to count to about 4000, while signals are adjusted to produce counts no larger than 1000.

At the end of the spill a signal from the accelerator (PRE-DET) is used to return control of the multi to the Sigma-2 and to interrupt the Sigma-2 to initiate event transfer. The Sigma-2 reads events from the buffer memory and writes them on tape. When this is done the Sigma-2 reads the various spill scalars and the quantameter and puts this information on tape as well as accumulating it internally. The Sigma-2 then begins accessing the memory for events to be used for online analysis and continues this until the interrupt occurs to initialize for the next spill.

CHAPTER IV. ANALYSIS AND RESULTS

A. Overview

The primary results we present are the comparison of the A dependence of high energy ρ and ρ' photoproduction. The state we call ρ' is called $\rho'(1600)$ and ρ'' quite commonly in the literature. Additionally, we present results on the energy dependence of ρ photoproduction. We present the energy dependences first, in sections B through E, as it illustrates how we analyze, bin, and correct the data for acceptance. In particular, we discuss our absolute normalization in terms of these data. These data were taken with the "diffractive" trigger described in Chapter III. This trigger requires at least two particles outside the beam region horizontally in our spectrometer and no particles outside the spectrometer. It favors diffractive photoproduction events but the continued use of the name "diffractive" should not be confused with the physical process of diffractive production discussed in Chapter I.

The remainder of our analysis, both ρ and ρ' A dependence, relies on the previous discussion of our analysis techniques from sections B through E. In addition, we use the optical model of photoproduction from nuclei developed in Appendix A. The A-dependence data for both the ρ and ρ' were taken simultaneously through a single trigger. We refer to this trigger as the HC-diffractive trigger because it is identical to the diffractive trigger except for the additional requirement of the hadron calorimeter (HC) energy threshold described in Chapter III. Comparison of data taken under the diffractive and HC-diffractive triggers allows us to understand the systematic bias introduced by the HC.

B. Data Selection and Reduction for ρ Energy Dependence Analysis

For the ρ photoproduction energy dependence we select a sample of data taken under the diffractive trigger. The counting rates and deadtime are low for this running. The sample consists of 30 runs collected in an almost uninterrupted three-day period. Thus the effect of long-term beam and apparatus drifts is minimized. The beryllium target used was 4% of a radiation length, sufficient to avoid non-target background, but thin enough to avoid problems from secondary interactions.

The data from this running period are on 30 tapes, each of which contains about 45K events. In an initial condensing pass through these tapes we have extracted the two-track events from all triggers (as well as the 3-5 track events for separate study). This and all subsequent analysis is performed on events that have passed through a track reconstruction program which does the pattern recognition to find the tracks and fit them, giving momentum and position vectors [Wijanco, 1976]. Additional requirements are made on the 2-track events to choose those suitable for analysis as ρ candidates. The tracks are required to have opposite charge and to pass within 0.2 inches of each other at some point. In addition, this point, the vertex position, is required to be between 244 inches and 276 inches upstream of the magnet center. The target is nominally 260 in. upstream of the magnet center. Figure (IV.B.1) shows the distribution of vertex positions along the beam line. The target and the B3 trigger counter are visible as clearly separated peaks. Also shown on the figure are the cuts used to exclude non-target interactions. Inspection of the figure shows that inside the cut interval we obtain the signal from the target with little loss or contamination. After throwing out uninteresting event topologies using the criteria just described, we are left with 141K events to input into the ρ analysis.

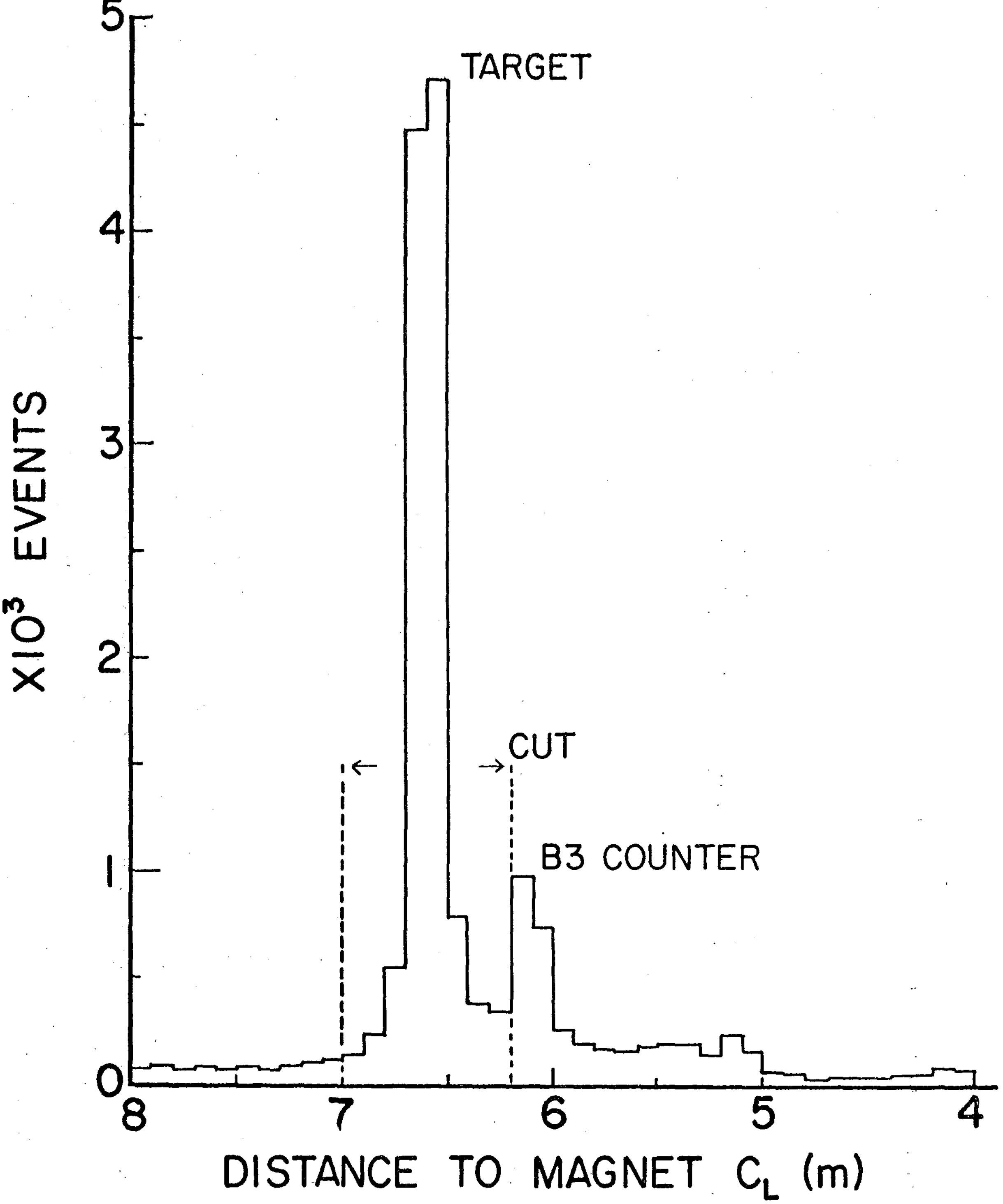

Fig. (IV.B.1) Distribution along the beam axis of the two track vertex positions. Events outside the cut region are excluded from the analysis.

The basic analysis consists of three stages, all done in one pass through the data. Geometric cuts are made on the events to insure a well-defined acceptance region. Various kinematic quantities are calculated and binned for those events passing the cuts and this information is stored on the computer disk for later use. The numbers of events and their disposition as well as the scalar rates and total quantameter readings are extracted from the tapes and tabularized for use in calculating the overall normalization.

The geometrical cuts are of two types, but both depend upon the survey data for the Z (beam) coordinate measurements of the chambers and counters. For the devices of interest to the ρ analysis these positions are known to better than 0.5 inch. One type of geometrical cut involves enforcing the PWC logic requirements. This is done by simply making sure that the hits in the PWC <u>associated with the tracks</u> satisfy the requirements described in the logic discussion, Section III. J. The Z information enters here because the track finding done by the reconstruction program depends on accurate chamber positions. The good track fits obtained are evidence of accurate survey information. The reconstruction program also needs offsets of the PWC's from a line in space so it can get good fits to tracks. In practice, the PWC reconstruction axis is not well known at surveying time and the X and Y (transverse to beam) positions are harder to measure than the Z positions for most devices anyway. Thus, the second set of geometrical cuts, the counter and aperture cuts, are made with respect to the PWC reconstruction axes and are only checked for consistency with the survey data. This is done by plotting the position of tracks at the various apertures and counters and either noting the position where tracks stop for apertures or where counter efficiencies reach a plateau. The counters can be checked by using the coincidence register data in the events. In this way, effective geometrical apertures are obtained which are then reduced by 0.25 inch to 1.0 inch to avoid any edge effects.

The apertures that must be satisfied are the following: vertical beam opening, and top and bottom of the trigger hodoscope; top and bottom of P4 and all edges of the magnet aperture. The PWC logic requirements are enforced in P2 and P3. These requirements are already redundant and the PWC requirements that are invoked last reject almost no events. Further requirements of the apparatus are redundant with these and are not invoked.

The events that pass the acceptance cuts are then binned by t, m_ρ, and E_ρ. All three quantities are calculated for the $\pi\pi$ pair. Assuming both particles are pions the invariant mass of the pair is m_ρ and E_ρ is the energy. To calculate the invariant momentum transfer (t) of an event, it is not sufficient to know only the four-momentum of the two presumed pions. t is defined in the following way:

$$t = (P_\gamma - P_\rho)^2 = (P_i - P_f)^2, \qquad \text{(IV.B. 1)}$$

where P_γ and P_ρ are the photon and ρ four-momenta and P_i and P_f are the initial and final target four-momenta. The information that we know in photoproduction with a broad-spectrum beam is $\hat{k}$, the incident photon direction, and the ρ four-momentum, that is E_ρ and $\vec{P}_\rho$. This brings us up short one scalar quantity of knowing enough to calculate t. If we knew the photon energy, for example, we could use the first part of relation (IV.B. 1). Since we are interested in the diffractive production of the ρ off a nucleus, however, we can assume that at least for small t we know the target mass M_A, which is just the mass of the whole nucleus. This is sufficient to calculate t.

$$t = [m_\rho^2 - 2E_\rho(E_\rho - \hat{k}\cdot\vec{P}_\rho)]/(1 + \hat{k}\cdot\vec{P}_\rho/M_A - E_\rho/M_A). \qquad \text{(IV.B. 2)}$$

$$E_\rho^2 = \vec{P}_\rho \cdot \vec{P}_\rho + m_\rho^2. \qquad \text{(IV.B.3)}$$

We should also note that the minimum possible t (most positive actually) is achieved when $\hat{k} \cdot \vec{P}_\rho = |\vec{P}_\rho|$. This value of t is called t_{min} and occurs for zero-degree production.

When t, m_ρ, and E_ρ have been calculated, they are binned in the following way. The event is placed in one of ten bins in E_ρ from 20 to 160 GeV. The first 6 bins are 10-GeV wide and the last 4 bins are 20-GeV wide. In addition, the m_ρ is binned in 24 bins from 0.4 GeV to 1.0 GeV. The t is binned in 60 bins, the first 20 covering from 0.0 to 0.04 $(\text{GeV}/c)^2$, the second 20 covering from 0.04 to 0.2 $(\text{GeV}/c)^2$, and the last 20 covering 0.2 to 0.68 $(\text{GeV}/c)^2$. Thus we have a data matrix of $10 \times 24 \times 60$ at the conclusion of the cutting and binning step, which contains 66,852 events, not counting events falling outside the binning range.

C. Monte Carlo

The next stage of the analysis is the generation of Monte-Carlo events. We try to model the actual data as closely as possible in the Monte Carlo in the variables we integrate over. By this we mean that the parameters such as those having to do with resolution and angular distribution, which do not appear explicitly in our cross section, are summed over and must be well modeled to start with. The parameters E_ρ, $|\vec{k}|$, t, and m_ρ are handled explicitly and their distributions can be modified after the Monte-Carlo generation is done. Thus in these variables we chose distributions that approximately model the data but are convenient to sample from.

The beam momentum is sampled from a table of spectrum data in 5-GeV intervals as it appears in Fig. (IV.C. 1). Within each 5-GeV interval the energy is distributed as $\exp(-0.0256\,|\vec{k}|)$, which is an approximate slope for the entire

Fig. (IV. C. 1)

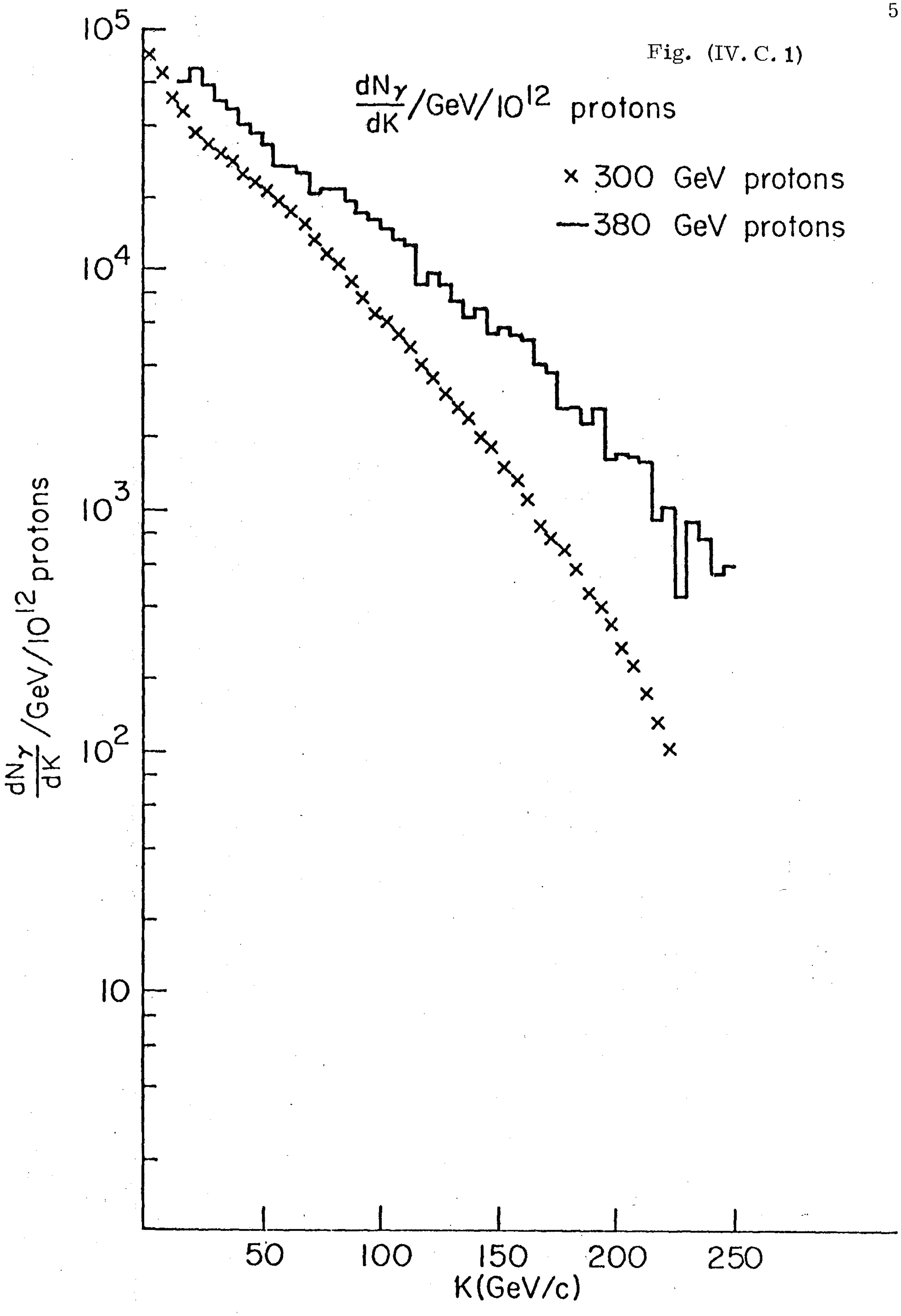
$\frac{dN_\gamma}{dK}$/GeV/10^{12} protons
× 300 GeV protons
— 380 GeV protons
$\frac{dN_\gamma}{dK}$/GeV/10^{12} protons
10^5
10^4
10^3
10^2
10
50
100
150
200
250
K(GeV/c)

spectrum. Notice that these data and spectrum are for 300-GeV protons incident on our beam-producing target. In order to generate sufficient events to insure that the Monte-Carlo statistics after cuts are better than four times that of the data in most of the region of interest and to avoid really unwieldy data sets, the Monte Carlo is run in four regions of energy. These regions, in GeV, are 15-45, 35-75, 65-105, and 95-165. Notice that all bins overlap and extend beyond the region of interest by 5 GeV. These are guard bands so that events that are moved in energy by resolution effects are gained and lost from each bin in appropriate numbers; this also allows us to bin in E_ρ instead of $|\vec{k}|$. In each region 100 K events are generated, of which typically 50% are lost to apparatus cuts.

The t value is sampled from a sum of two exponentials with slopes of 50.0 and 7.0 $(\mathrm{GeV}/c)^{-2}$. -t must be greater than or equal to $-t_{\min}$ and is divided between the two exponentials in a ratio such that as $t \to 0$ they are in the ratio (72/9). The two distributions are supposed to represent the coherent and incoherent scattering and the target recoil mass used is that of the beryllium nucleus and the proton respectively. The mass m is generated from a sum of a simple Breit Wigner of constant width Γ_ρ and a linearly falling term that goes to zero at the ρ mass.

$$\frac{d\sigma}{dm_{\pi\pi}} = \frac{m_{\pi\pi} m_\rho \Gamma_\rho}{(m_\rho^2 - m_{\pi\pi}^2) + m_\rho^2 \Gamma^2} + b\left(1 - \frac{m_{\pi\pi}}{m_\rho}\right). \qquad \text{(IV.C. 1)}$$

$m_{\pi\pi}$ is the generated mass and the second term is defined to be zero for $m_{\pi\pi} > m_\rho$. We use $m_\rho = 0.760$ GeV and $\Gamma_\rho = 0.175$ GeV here. b is set implicitly by requiring that the non-Breit Wigner part of $d\sigma/dm_{\pi\pi}$ be 25% of the total in the region of generation $(0.3 < m_{\pi\pi} < 2.0)$. Please note that these parameters are not meant to reflect the true mass or t dependence of the process but are merely weighting factors that concentrate the events where they are needed to match the statistics of the data and at the same time the parametrization yields speedy samples. For example, a flat distribution in mass is very easy to generate but the total number of events needed would be dictated by the statistics in the ρ mass peak and needlessly large numbers of events would be generated in other regions. This is even more true for the t distribution which is so sharply peaked that the Monte Carlo must distribute its events similarly to the data or be disastrously wasteful.

The interaction point is distributed uniformly in the target in all three dimensions, though only the transverse dimensions are important. The size of the interaction region transverse to the beam is adjusted to be equal to that seen in the real data and the beam direction is that given by the average direction of Bethe-Heitler electron pairs used in spectrum measurement in runs taken immediately after these. The precise beam divergence is hard to determine and is not an important effect, as the beam direction is. It was set to be that of a point source located at about our beam production target 5040 in. upstream of the photoproduction target.

The $\rho \rightarrow \pi^+\pi^-$ decay angular distribution is known to be s-channel helicity conserving (SCHC) from detailed experiments of ρ photoproduction in polarized photon beams [Ballam et al., 1973]. The decay of a spin one odd parity state to two spin zero odd parity states is described by a $\sin^2\theta$ distribution in the decay center of mass about some axis. The SCHC hypothesis fixes this axis to be the direction of the recoil in the ρ rest frame. Since the beam and target are not polarized the recoil azimuth is randomly distributed about the beam direction and the decay axis in the ρ rest frame is randomly distributed in azimuth about the recoil direction. This information, then, completely specifies the distribution of the two pions in the lab frame, when combined with some elementary kinematics, rotations and Lorentz boosts to move through the various frames where the different parts of the process are described simply.

The Monte Carlo at this point has generated events that can be used to model the physics of the ρ production and decay, including the beam parameters. In order to model the effects of the apparatus the tracks generated by the Monte Carlo are propagated through the apparatus and PWC addresses are generated and sorted as they would be by the hardware itself. The result of the Monte Carlo is a data tape written in the same format as the original data tapes written on-line as the data is taken, with one exception we shall explain momentarily. When this is done, multiple scattering is not included as a separate effect, however, the appearance of such things as target vertex distributions which closely match those of the data convince us that PWC granularity dominates the measurement error. The magnet is modeled by a box field with an integral that varies according to a track's average position transverse to the beam line as determined from a field map of our magnet. Because most of the information in the coincidence register block is not used in the analysis no attempt is made to project tracks to counters and set the appropriate bits for the counters and bus lines. The geometrical cuts made at analysis time on the projected track coordinates at counter planes and PWC's serve to enforce the counter trigger requirements. The exceptions to this are the coincidence register bits for B3 (the target counter) and the trigger store bits. B3 and all trigger store bits are set so that when the analysis checks an event for the target counter and any trigger type it will be satisfied.

The ρ analysis (and all others we discuss here) makes no use of the ADC (analogue-to-digital converter) information in the events. The major difference between a real event on tape and one generated by the Monte Carlo is that the Monte-Carlo program makes no attempt to place meaningful pulse heights or pedestals in the ADC event field, but uses this region to hide two types of information for later use.

One class of information is mainly diagnostic and consists of the packed and encoded output that the reconstruction program would generate for the event in question for the case of ideal resolution. Thus, when the Monte-Carlo data tape is passed through the reconstruction program (just as a normal tape is) we can check to see what success the reconstruction program has had identifying and fitting the tracks compared to what was generated, on an event-by-event basis. For two-track events the success is 100%, which is not surprising due to the simplitiсy of the track-identification problem. In a test run earlier on a class of two-track events slightly different than the ρ in kinematics we have verified that with random single-hit deletions the reconstruction is still 100% efficient in track finding. For the more complicated case of four-track events that come from a simulation of $\rho'(1600) \rightarrow 4\pi^{\pm}$ decay, reconstruction topology failures are < 1%.

The other information hidden in the ADC region of a Monte-Carlo event is more crucial and consists of four floating point numbers. The quantities are the photon energy, target mass, -t, and parent mass (m_{ρ}). These are the generated quantities that suffer from no resolution or beam-divergence effects and are sufficient to determine all parameters of the event that are not being integrated over in the Monte Carlo. Their purpose will become clear later, but bear in mind that for these quantities the generated and final "smeared" values are available on an event-by-event basis after the Monte-Carlo data tape is reconstructed.

D. Determining the Mass and t Dependence of the Data

We produce as our resultant cross section $d\sigma/dt$ at $t = 0$, $(d\sigma/dt|)_0$. In order to determine that quantity, it is necessary to model both the ρ mass and production t dependence for a fairly wide range of mass but only for small t. By $t = -0.04\ (\mathrm{GeV/c})^2$, for example, most of the coherent production from beryllium is gone and naturally for the elements of higher A (total number of nucleons) the coherent t peak falls even faster with increasing (-t). Because of the narrow t interval that we cover in particular we can factor the double differential cross section in the following way.

$$\frac{d^2\sigma}{dtdm} = T(t) \times M(m). \qquad \text{(IV.D. 1)}$$

While this factorization is not essential to our approach, it simplifies the fits as we shall see. The assumption has been checked by looking for a difference in the mass fits as a function of t, and no significant variation occurs in the modest range used in the analysis.

In all previous analyses of ρ photoproduction, difficulty has arisen with the parametrization of the mass distribution. The problem appears to be due to interfering non-resonant 2-pion photoproduction that skews the ρ peak and confuses the normalization at the 10 to 15% level. This 2-pion photoproduction is thought of as occurring by the photon virtually dissociating into a $\pi^+\pi^-$ pair, one or both of which interact with the target. This is a strong-interaction problem that has not been solved satisfactorily. The early approaches are due to [Söding, 1966] and [Ross and Stodolsky, 1966], more recently [Bauer, 1971] has extended the Söding approach significantly. In a review of this problem [Spital and Yennie, 1974a] have concluded that at the present time no satisfactory theoretical solution exists and advocate and test on data from two experiments a phenomenological approach. Their results lead us to use an abbreviated form of their prescription for the ρ mass distribution problem.

Motivated by the discussion of the ρ mass shape by Spital and Yennie we choose the following mass distribution.

$$M(m) = \frac{m m_\rho \Gamma(m)}{(m_\rho^2 - m^2)^2 + m_\rho^2 \Gamma^2(m)} \times \left[1 + C_5\left(\frac{m_\rho^2 - m^2}{m^2}\right) + C_6\left(\frac{m_\rho^2 - m^2}{m^2}\right)^2\right] \quad \text{(IV.D. 2a)}$$

with

$$\Gamma(m) = \frac{\Gamma_\rho m_\rho}{m}\left(\frac{m^2 - 4m_\pi^2}{m_\rho^2 - 4m_\pi^2}\right)^{3/2} . \quad \text{(IV. D. 2b)}$$

We fix $\Gamma_\rho = 150$ MeV and $m_\rho = 770$ MeV and allow C_5 and C_6 to vary in the fits to model the interference of the ρ and non-resonant $\pi^+\pi^-$ production in a phenomenological way. Then we determine dσ/dt by

$$\frac{d\sigma}{dt} = \frac{\pi\Gamma_\rho}{2} \left.\frac{d\sigma}{dtdm}\right|_{m = m_\rho} . \quad \text{(IV.D. 3)}$$

The t dependence is modeled by the sum of two exponentials. The second one is meant to represent the incoherent production of the ρ and we expect that in the region where it is important its slope to be that of the hydrogen data. The first exponential represents the coherent production and is an approximation of more complicated behavior as discussed in Section II and Appendix A.

$$T(t) = C_1[C_2 \exp(C_3 t) + \exp(C_4 t)] . \quad \text{(IV. D. 4)}$$

The m and t fits are not done simultaneously; this simplification is possible due to the factorization of the mass and t dependence of the cross section.

The fits are performed in the following way. First the Monte-Carlo data described earlier is reconstructed and passed through the same analysis program as was used for the data. In the case of the actual data, the cut and binned accumulated numbers of events are saved as tables on the computer disk as described earlier. For the Monte-Carlo data, after the cuts are made, the actual events are saved on the disk in a very compressed form containing only the four numbers hidden in the events by the Monte Carlo and the three numbers (m, -t, and E) that can be calculated from the data. E is the energy of the presumed $\pi^+\pi^-$ pair. The fit is made by feeding the tabulated binned data and the abbreviated Monte-Carlo events to an iterative fitting routine that reweights the Monte-Carlo events to match the data. The constants C_i are determined by choosing them such that χ^2 is minimized for the Monte-Carlo events weighted by M(m) and T(t) containing as parameters the C_i. χ^2 is the summed square deviations of the data from the Monte Carlo weighted by the expected error, added up for the bins in the region being fit. The fit region for the mass is from 600 MeV to 1000 MeV, and the bin width is 25 MeV as mentioned earlier. The t fit is made over several intervals, with the final results from a fit for $-t_{min} < -t < 0.2\ (\text{GeV}/c)^2$ and including events only in the interval used for the mass fit.

Figure (IV. D. 1) shows the raw dN/dM that is input to the fitting for the 80- to 100-GeV bin in $E_{\pi\pi}$, presumed to be E_ρ. Figure (IV. D. 2) is the raw dN/dM in the low t region with the fit Monte-Carlo distribution overlaying it. Standard values of C_5 and C_6 were used, $C_5 = 3.0$, $C_6 = 3.0$. Notice that the uncorrected dN/dM and dN/dt are always the input to the fitting procedure and that the result of the fit is a model for these uncorrected results for best values of the parameter, C_i.

The t distribution for this same energy interval is shown in Fig. (IV. D. 3), with some bins left out at low t for clarity. The same data are shown in Fig. (IV. D. 4) along with the Monte-Carlo model of the distribution. The statistics of the Monte-Carlo points are better than the data, as discussed earlier. This figure shows in the t interval of interest to us that the exponential t fit is an

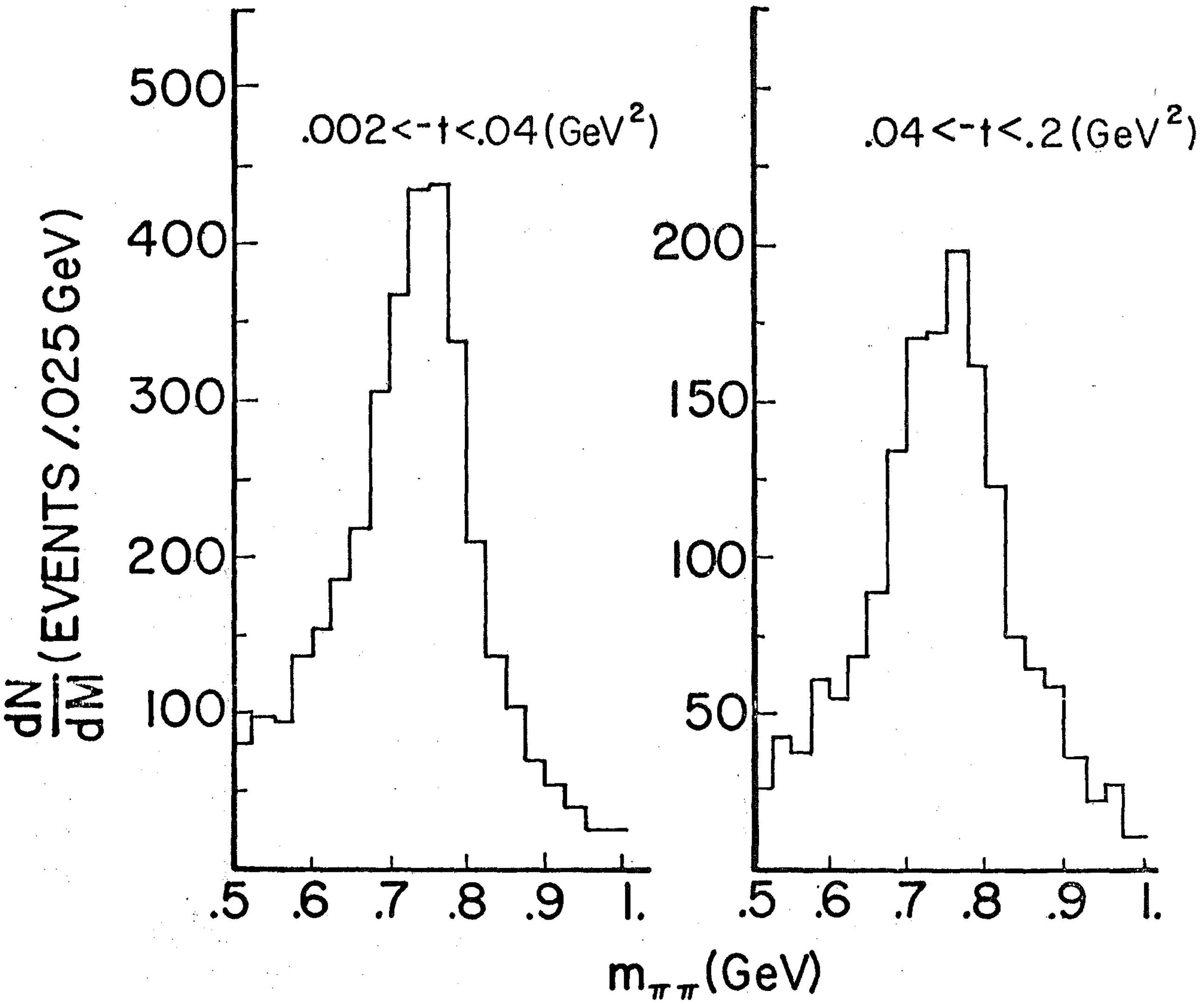

Fig. (IV.D.1) dN/dM uncorrected for acceptance or resolution. $80<E_{\pi\pi}<100$ Gev.

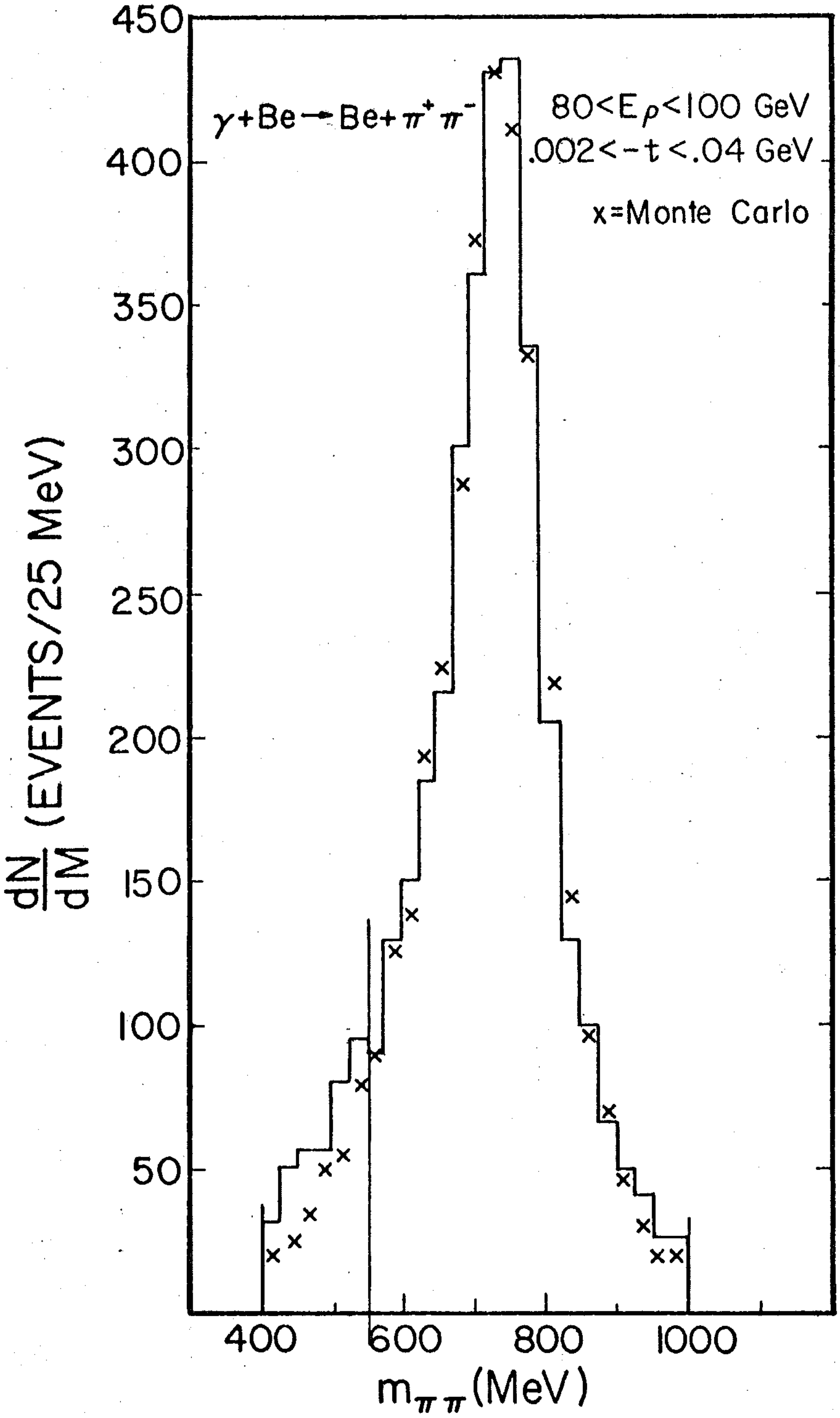

Fig. (IV.D.2) Monte Carlo model of uncorrected dN/dM compared to data.

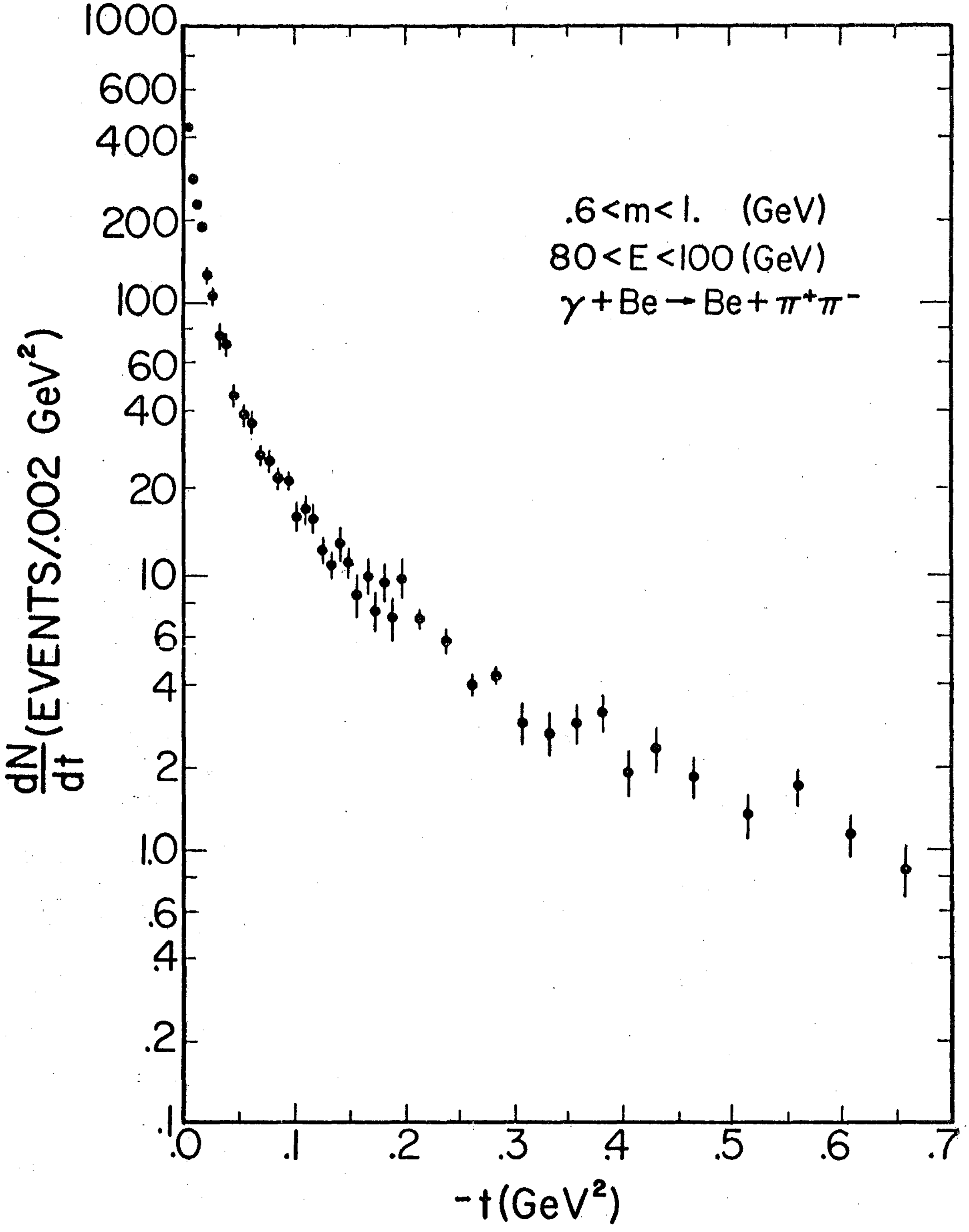

Fig. (IV.D.3) dN/dt uncorrected for acceptance or resolution.

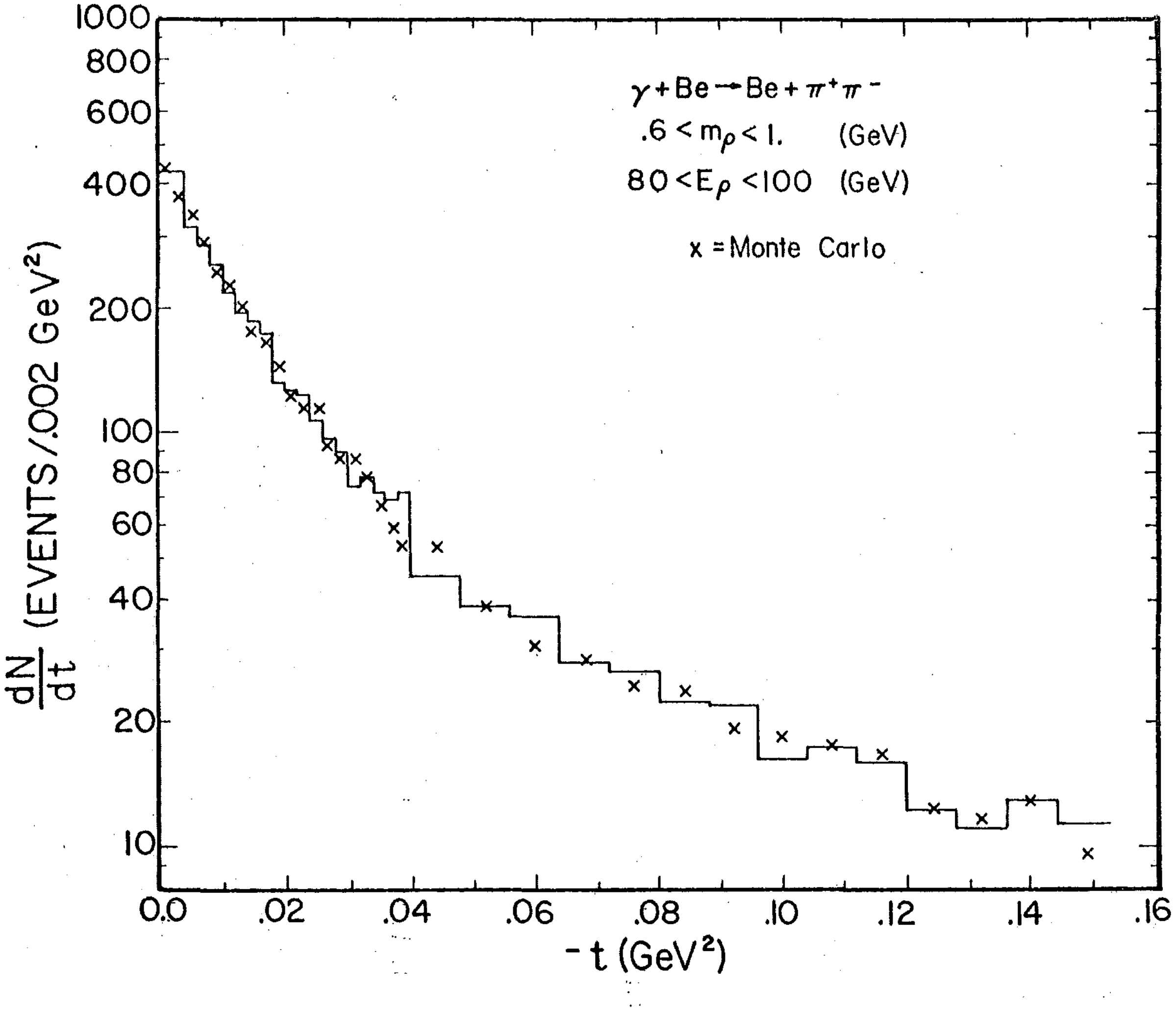

Fig. (IV.D.4) Monte Carlo of uncorrected dN/dt compared to the data.

excellent representation of ρ photoproduction from beryllium. The parameters and normalization of this fit are just those shown in the later figures and tables for this energy bin. The values of the parameters C_3 and C_4, the coherent and incoherent t slopes, are shown in Figs. (IV. D. 5) and (IV. D. 6). The errors shown are purely statistical here and on other figures and tables unless otherwise noted. The E_ρ bin from 20 to 30 GeV does not appear in any of our results because the mass acceptance eliminates most of the ρ region. This is primarily due to the aperture restriction of the magnet, and no fits are attempted below 30 GeV in E_ρ.

The value and behavior of parameter C_4 should not be taken too seriously. The incoherent scattering cannot really be exponential down to very small t. Also we do not go to a large enough t to pin down the second slope in the lower statistics high-energy bins. The double exponential fit is a good representation of the data, but the two individual components cannot be easily interpreted as entirely coherent and incoherent production when separated. [Spital and Yennie, 1974b] find that in the low t region, optical-model fits reject a simple incoherent background under the coherent peak. Thus we view our t fit as an interpolating function that allows us to obtain $d\sigma/dt|_{t=0}$.

E. Absolute Normalization

Before presenting the remaining results of the fits just described we exhibit the method of the absolute normalization so that $d\sigma/dt$ instead of dN/dt can be presented. Because the photons cannot be counted in our incident beam, the calculation of a cross section is slightly more involved and less direct than in a charged beam. With the acceptance and resolution taken into account by the fit to provide a true dN/dt, the cross section is determined in the following way.

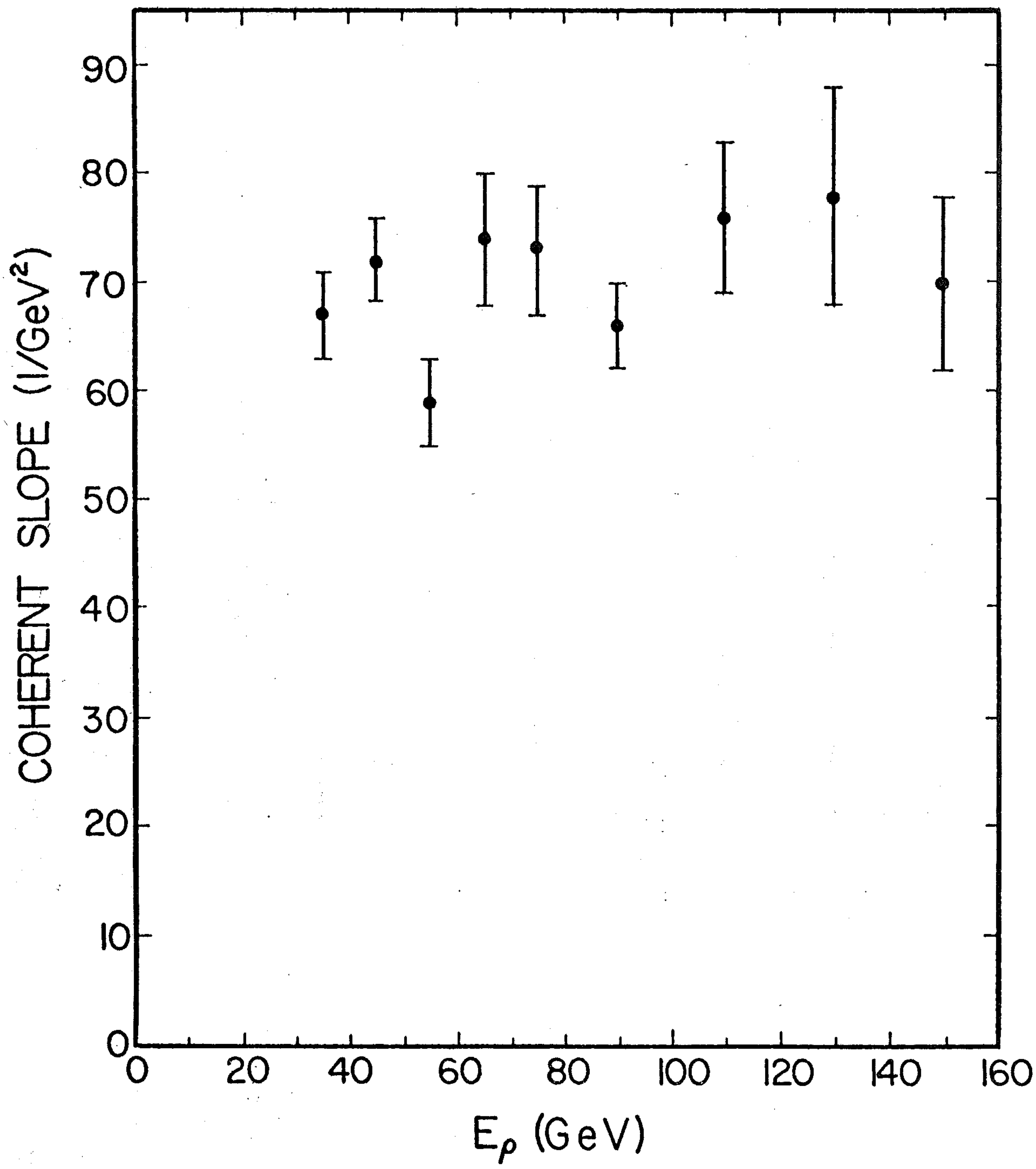

Fig. (IV.D.5) $\gamma+Be\to\pi^+\pi^-+X$, coherent t slope from an exponential fit (parameter C_3).

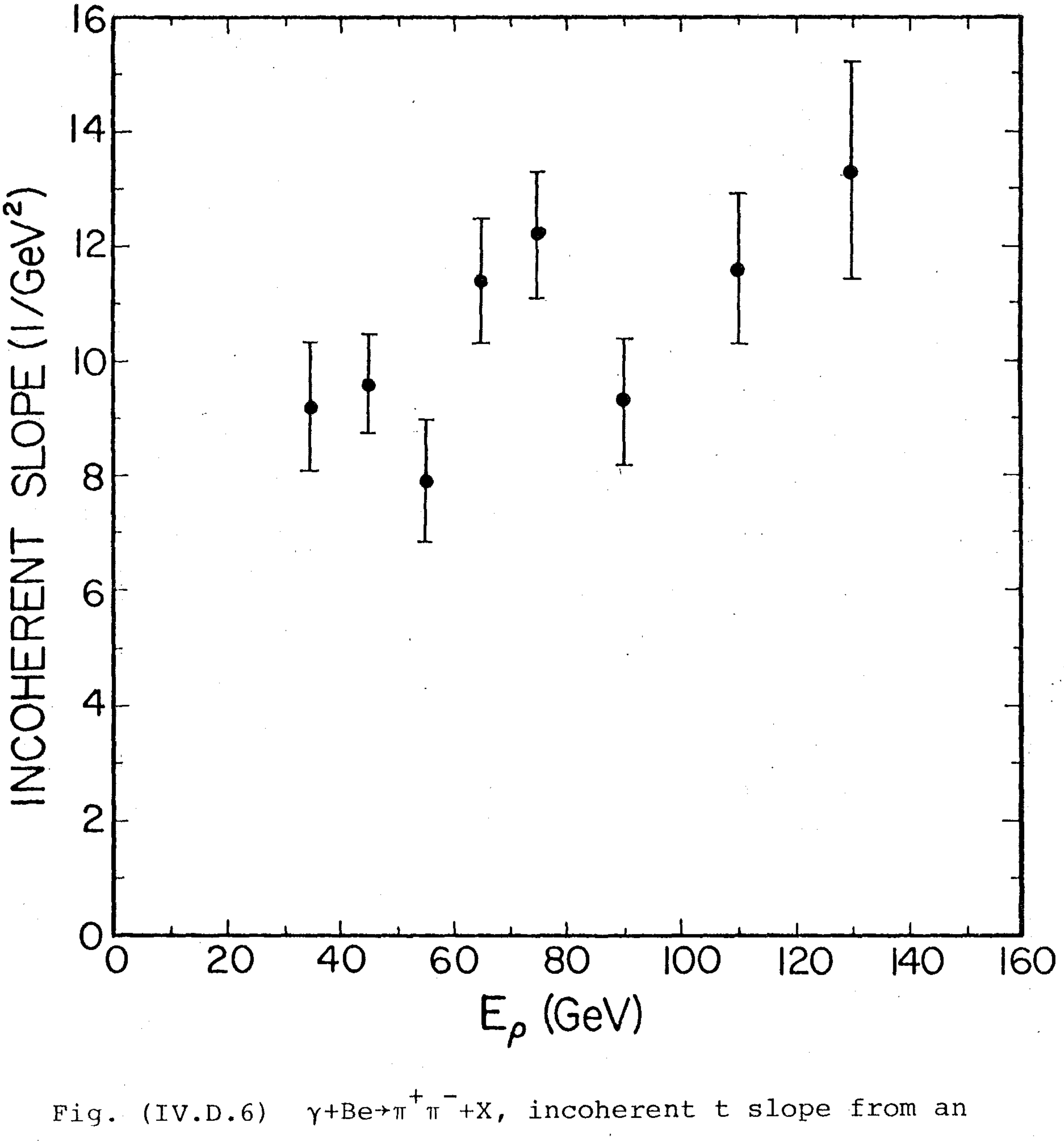

Fig. (IV.D.6) $\gamma+Be\rightarrow\pi^+\pi^-+X$, incoherent t slope from an exponential fit (parameter C_4).

$$\frac{d\sigma}{dt} = \frac{1}{N_f \rho_s \ell} \frac{dN}{dt} . \qquad \text{(IV. E. 1)}$$

In the above, N_f is the number of incident photons in the energy range in question, ρ_s is the volume density of scatterers (nuclei) in the target, and ℓ is the target length.

For our beryllium target, $\ell = 11/16$ in., and the density of beryllium is $1.848\ \mathrm{g/cm^3}$. This means that ρ_s is 1.235×10^{23} nuclei/cm^3. Thus, in nuclear units, (1 barn $= 10^{-24}\ \mathrm{cm}^2$), the target factor from the normalization is

$$\frac{1}{\rho_s \ell} = 4.64 \text{ (barns/nucleus).} \qquad \text{(IV. E. 2)}$$

In order to determine the flux we use the integrated beam power as measured each accelerator pulse in the quantameter. To convert the quantameter reading in Coulombs to energy in GeV we use the experimentally determined conversion factor 1.500×10^{16} (GeV/Coulomb). If C $(dN/dk)_{UN}$ is the energy spectrum of the photon beam as measured by the apparatus, where C is an undetermined overall formalization factor, then N_f is defined as follows

$$N_f = C \int_{E_1}^{E_2} \left(\frac{dN}{dk}\right)_{UN} dk. \qquad \text{(IV. E. 3)}$$

E_1 and E_2 are the limits of the photon energy range in question. Q_e is the total beam energy defined by the following:

$$Q_e = C \int_0^{E_{max}} \left(\frac{dN}{dk}\right)_{UN} k\, dk. \qquad \text{(IV. E. 4)}$$

E_{max} is the effective spectrum endpoint. Since Q_e is the result of the quantameter measurement, we can use it to eliminate the unknown normalization C. Combining the two above relations with the conversion factor for the quantameter we obtain an expression for the flux in terms of the unnormalized spectrum and the net quantameter charge Q.

$$N_f = 1.500\times 10^{16}\times Q(\text{Coulombs})\times \frac{\int_{E_1}^{E_2}\left(\frac{dN}{dk}\right)_{UN}dk}{\int_0^{E_{max}} k\left(\frac{dN}{dk}\right)_{UN}dk} \qquad \text{(IV.E. 5)}$$

Two types of corrections must be made to these flux factors before calculating the cross sections. One of these is the beam absorption effect and the other is the live-time fraction, both of which are most conveniently put in as an effective charge, Q_{eff}, from the quantameter. The beam absorption correction is from two sources. First, the quantameter is located downstream of the analyzing magnet so that only very high energy pairs created upstream of the magnet can reach it; thus the beam power measured in the quantameter is not the beam power incident on the target. A second partially compensating effect is the shielding of the target itself. These effects together yield the following multiplicative corrections to the quantameter charge Q.

$$\text{Target Beam Conversion: } e^{\mu X_t} \qquad \text{(IV.E. 6a)}$$

$$\text{Target Self Shielding: } \frac{1}{\mu X_t}\left(1 - e^{-\mu X_t}\right) \qquad \text{(IV.E. 6b)}$$

$$\text{Other Beam Conversion: } e^{\mu X_{US}} \qquad \text{(IV.E. 6c)}$$

X_t is the target length in radiation lengths and X_{US} is the amount of other material upstream of the magnet in radiation lengths. μ is a correction factor from electron energy loss to photon pair conversion and is about 7/9 (0.773). $\mu X_t = 0.038$ and $\mu X_{US} = 0.028$, yielding just under 5% decrease in the calculated cross section. For some of the targets used in the A dependence analysis of Sections F and G these effects are slightly larger. All of our quoted cross sections include these and the following livetime corrections.

The livetime correction is also from two sources. One of these is a prescale (PS) that was set on the trigger type measured here of either 1 or 2 depending on which of the 30 runs one examines. The prescale of 1 means all events are kept, 2 means that every other one is discarded and never appears on the data tape. This correction and the other livetime correction are made on a run-by-run basis. The other correction is for interactions that were not observed either because the trigger logic was busy making a decision on an earlier event or because read in of an accepted event was already in progress. The fraction of interactions that occur during a time when the logic is ready to process them is the ratio of the scaled quantities "logic gate * logic not busy ÷ 16" and "logic gate : 16." We write this in the following way:

$$\frac{(LG * L\ \overline{BUSY}/16)}{(LG/16)} . \qquad (IV.E.7)$$

Of the interactions that are processed by the logic, the fraction that occur for the diffractive trigger (TSB # 14) during a time when they can be read into the memory is the ratio of "TSB # 14 * system not busy" and "TSB # 14 * logic not busy." We write this in the following way.

$$\frac{(\#14 * S\ \overline{BUSY})}{(\#14 * L\ \overline{BUSY})} . \qquad (IV.E.8)$$

Thus the livetime fraction (LTF) that is to multiply the observed Q is the following.

$$LTF = \frac{(LG * L\ \overline{BUSY}/16)}{(LG/16)} \times \frac{(\#14 * S\ \overline{BUSY})}{(\#14 * L\ \overline{BUSY})} \times \frac{1}{PS} . \qquad (IV.E.9)$$

The Q accumulated during these runs is 14.041×10^{-6} at PS = 1 and 23.927×10^{-6} at PS = 2, thus the $Q_{\text{effective}}$ with prescale correction only is 26.00×10^{-6}

Coulombs. After applying the remaining corrections, the final Q_{eff} is 23.75×10^{-6} Coulombs, which is then used in the normalization in place of Q in Eq. (IV. E. 5). The other major fixed input to Eq. (IV. E. 5) is the spectrum as represented in the 300-GeV plot in Fig. (IV. A. 3).

With the above information available, the normalization is carried out by the same program that does the fit. It has the spectrum table and the endpoints of the energy bin being fit. The total number of generated Monte-Carlo events in the energy bin, the $Q_{effective}$ in Coulombs and the target factor in barns/nucleus, are also input so that at the end of the fitting step the normalization and statistical error calculation are done. The result of this for the total $d\sigma/dt$ at $t = 0$ are shown in Fig. (IV. E. 1a).

In Fig. (IV. E. 1a) $d\sigma/dt$ is defined by Eq. (IV. D. 3) as it will be at all points in our discussion. The results of the fits to diffractive ρ photoproduction from beryllium, binned by ρ energy, are summarized in Table (IV. E. 2). For reasons we have discussed, values of C_2 and C_4 must be interpreted cautiously. In Fig. (IV. E. 1b) we compare our results for $d\sigma/dt|_0$ to those of earlier low energy experiments on one figure. The low-energy points show some scatter but tend to be larger than our high-energy measurements. This is particularly true if one only looks at the Cornell [McClellan, 1971] and DESY-MIT [Alvensleben, 1970] data, the most intensively analyzed of the results shown.

The errors quoted in Table (IV. E. 2) and Fig. (IV. E. 1b) are determined by the statistical uncertainty of our data sample. No contribution from systematic uncertainty is included in our errors. This does not imply that we feel the data are free of systematic uncertainties, but rather that we are unable to estimate them. An example of this kind of effect is the quantameter. As discussed in Chapter III the quantameter was calibrated with electrons of 10-15 GeV at SLAC before the

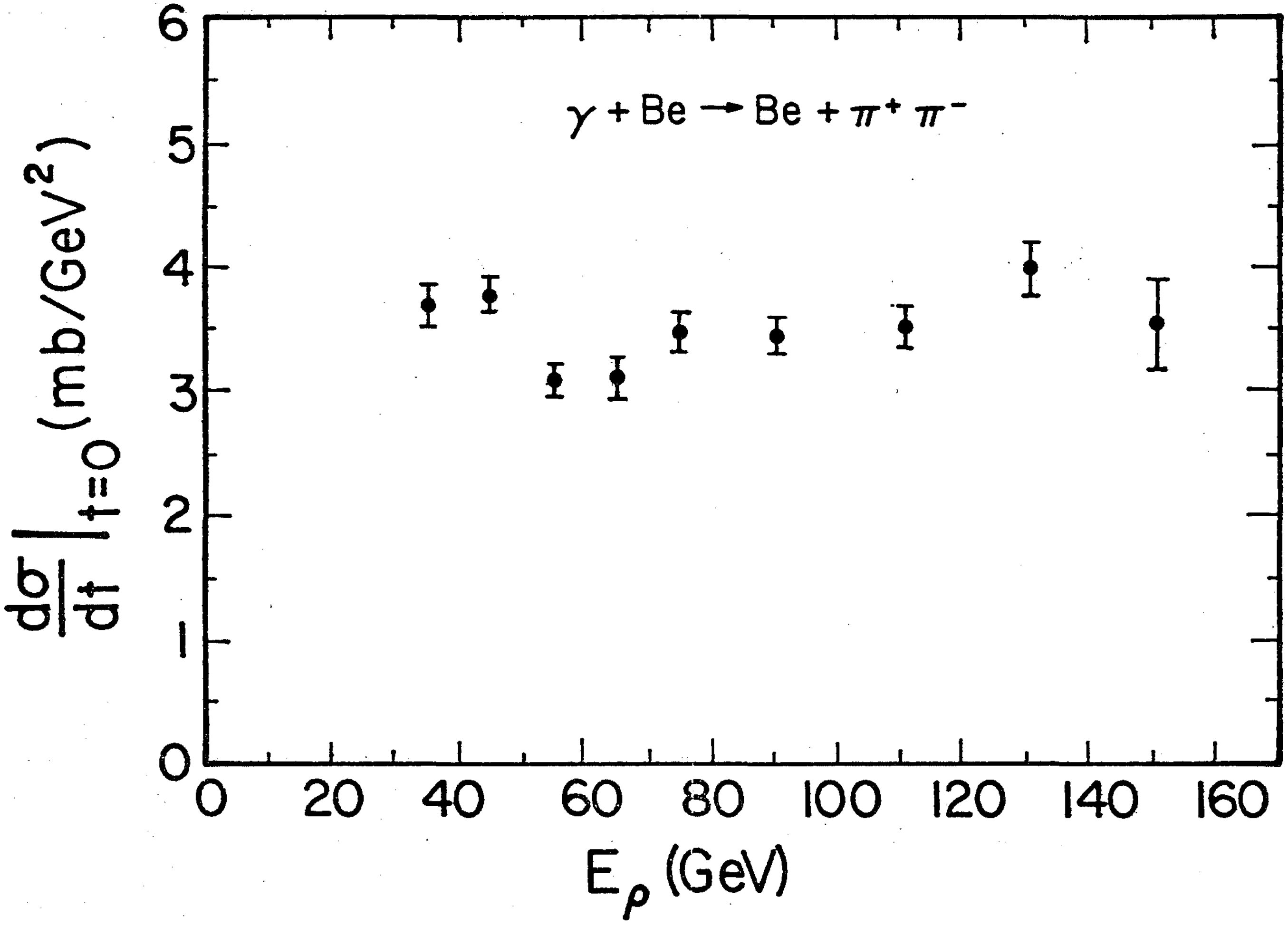

Fig. (IV.E.1a) Energy dependence of forward cross section for ρ photoproduction from berylium.

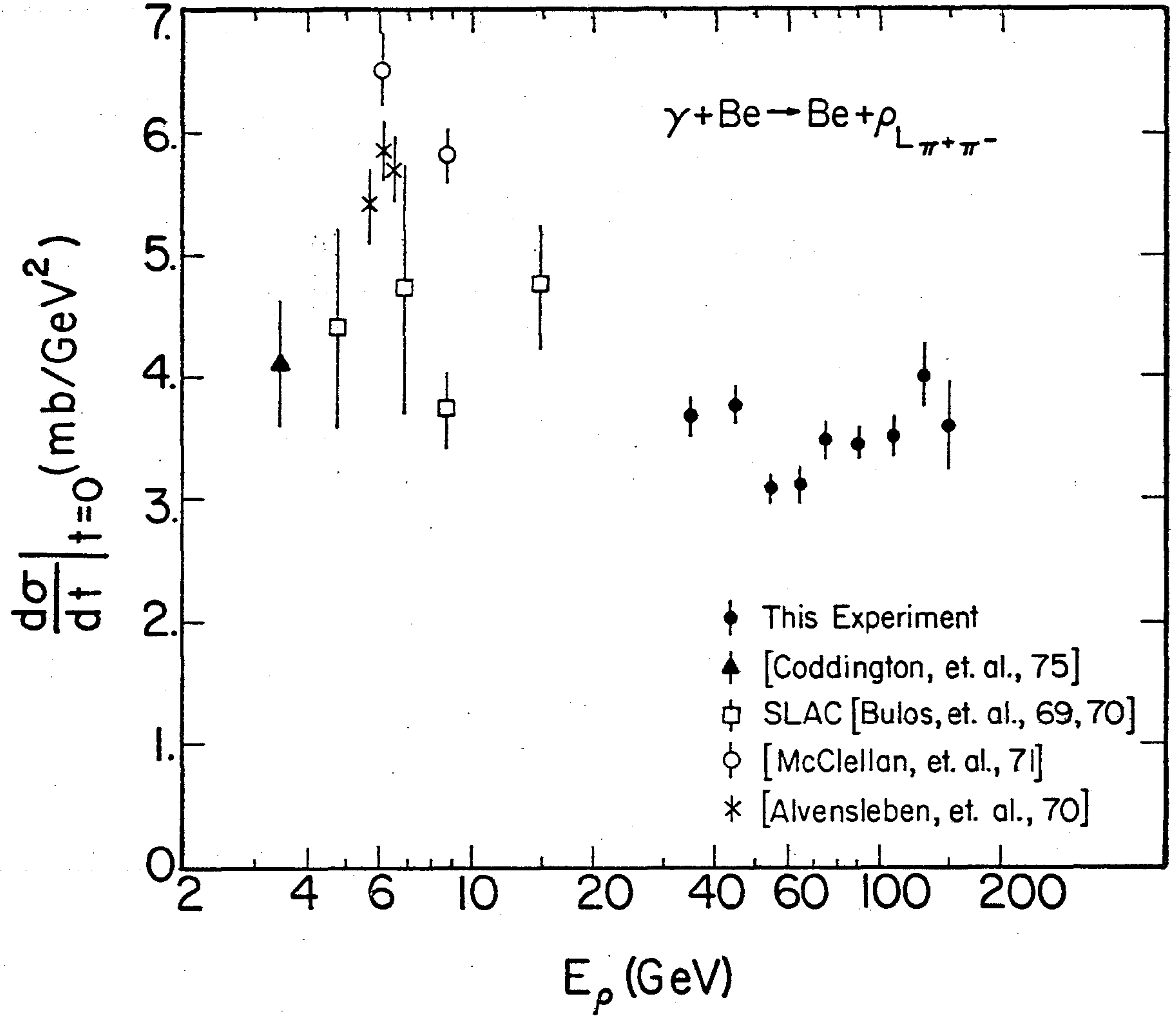

Fig. (IV.E.1b) Energy dependence of forward cross section for ρ photoproduction from berylium. Data from several low energy photoproduction experiments is shown for comparison.

Table (IV.E.2). Results of Fits to $\gamma + Be \rightarrow Be + \pi^+\pi^-$ Data as a Function of ρ Energy, E_ρ. $\sigma_{\gamma Be \rightarrow \rho}$, the Photoproduction Cross Section, Is Obtained By Integrating the Exponential t Fit. [See Eq. (IV.D.4) for the form of the fit.]

E_ρ (GeV)	$\left.\frac{d\sigma}{dt}\right\|_0$ (mb/GeV^2)	$\sigma_{\gamma Be \rightarrow \rho}$ (μb)	C_3 (GeV^{-2})	C_4 (GeV^{-2})	C_2
30- 40	3.67±0.14	102±3	66.9±4.3	9.2±1.1	6.4±0.9
40- 50	3.75±0.14	96±2	72.4±4.1	9.6±0.9	6.5±0.8
50- 60	3.06±0.11	91±3	59.4±3.7	7.9±1.2	7.4±1.2
60- 70	3.10±0.14	84±2	73.6±6.0	11.4±1.1	4.6±0.7
70- 80	3.46±0.15	88±2	73.1±5.8	12.2±1.1	4.9±0.8
80-100	3.43±0.12	91±2	66.3±4.1	9.3±1.1	7.0±1.1
100-120	3.50±0.18	90±3	76.0±7.0	11.6±1.3	5.0±0.9
120-140	3.99±0.28	93±3	78.6±10.2	13.4±1.9	4.8±1.2
140-160	3.58±0.34	-	69.6±7.9	-	-

experiment started. The quantameter is, in principle, a precision device, but because no electromagnetic beam above 20 GeV was available before the construction of the broad-band photon beam, the quantameter is operating in an energy range 10 times that for which it and its electronics have been calibrated.

Because of uncertainties such as this, the subsequent data and results we present will be analyzed in a way that is as independent of systematic effects as possible. In particular, we shall analyze and interpret all subsequent results without relying on the absolute normalization of the data.

For the above reasons we do not make any statement about the energy variation of the ρ photoproduction cross section from the low-energy experimental points to our own. However, we can determine the energy dependence of $d\sigma/dt|_0$ for ρ photoproduction from Be in our own energy range without difficulty. The important conclusion we draw from this part of our data is that the forward cross section for ρ photoproduction is energy independent from 30 to 160 GeV. The mean of the cross section in this energy range is $d\sigma/dt|_0 = 3.42 \pm 0.28\ \mu b/GeV^2$.

F. ρ Photoproduction A Dependence Analysis

The analysis of ρ photoproduction from four targets of increasing A is essentially that for the ρ energy dependence from beryllium, and we describe only the differences here. The target (A) sample available to us is Be (9.0), Al (27.0), Cu (63.6), and Pb (207). The two properties that distinguish the data on elements of A greater than 9 from data on beryllium are a change in the trigger and smaller statistics. These properties effect the binning we choose and also the choice of beryllium data to include in this analysis.

The only change in the trigger from the earlier ρ runs is the addition of a hadron calorimeter (HC) total pulse-height requirement. The purpose of this is to require a significant amount of energy in an event that is not from photons or electrons, thus triggering more selectively from the hadronic component of the photon cross section. This is especially important for large A targets because the relative amount of Bethe-Heitler e^+e^- pair production is larger and unless the trigger rejects these events very well, they will overwhelm the hadronic component of the data tapes. Also, an energy requirement will avoid triggering on events from low-energy photons for which our acceptance is low.

We pay a price for the enriched triggers that the HC requirement gives us. The energy resolution of this trigger is very broad, turning on between 20 and 50 GeV. This means that events in this energy range do not have a trigger efficiency that is easily calculable and we eliminate them so that we have a geometrically-defined acceptance for all events kept in the analysis. The ρ and ρ' data were taken at the same time with the same trigger so that a comparison of ρ and ρ' production can be made independently of systematic effects in overall normalization. The ρ-nucleon and ρ'-nucleon total cross sections obtained from the A dependence are independent of normalization. Moreover, we can measure the size of the effect of the HC in the trigger because we have data from beryllium taken both with the diffractive trigger and with the HC-diffractive trigger.

The number of runs we have with the HC-diffractive trigger on each target are 5 on beryllium, 3 on aluminum, $4\frac{1}{2}$ on copper, and 3 on lead. Recall that we have 30 runs with the diffractive trigger in our beryllium E_ρ dependence data. We use exactly the same cuts on all data, as previously described. We then compare the total number of events as a function of E_ρ from the HC diffractive trigger (A dependence) data with that obtained from the 30 runs of diffractive trigger data taken on beryllium (used already for E_ρ dependence). We find that the percentage of data on all targets with HC requirements compared to beryllium with no HC is stable above 50 GeV. The relative number of events with energy (E_ρ) > 50 GeV for these data compared to those used for the energy dependence is 47% for Be, 44% for Al, 26% for Cu, and 13% for Pb. This tells us the relative statistical strength of the A dependence data. We also see that the HC trigger enriches the ρ sample per run above E_ρ = 50 GeV by a factor of 3. By normalizing the Be data taken with and without the HC requirement, we have determined that the efficiency of the HC requirement is 95%. We correct all quoted cross sections for the ρ and ρ' data to account for this 5% inefficiency.

The analysis, binning, Monte Carlo, fitting and absolute normalization are done just as with the 30 runs used earlier for energy dependence, with the following exceptions. The binning in E_ρ is a single bin from 50-140 GeV. The same Monte-Carlo events are used to fit all 4 elements as are used on the 30 beryllium runs.

The normalization procedure is unchanged except for the 5% HC correction. The beryllium target is the same as used earlier (11/16 in.) which means $(\rho_S \ell)^{-1}$ = 4.64 barns/nucleus. The prescale factor on all of these runs is 1, independent of target. The properties of all the targets used along with the flux factors are listed in Table (IV. F. 1). The targets heavier than beryllium are composed of two pieces of material and are so marked in the table. $Q_{\text{effective}}$ contains the HC efficiency correction.

Table (IV. F. 1). Targets and Flux Factors for the A Dependence Runs.

Target	ℓ (Inches)	$(\rho_S \ell)^{-1}$ (Barns/Nucleus)	Q (Coulombs)	$Q_{\text{effective}}$ (Coulombs)
Be	11/16	4.64	1.198×10^{-5}	1.097×10^{-5}
Al	2×0.259	12.61	0.794×10^{-5}	0.739×10^{-5}
Cu	2×0.062	74.8	1.259×10^{-5}	1.136×10^{-5}
Pb	2×0.026	229.5	0.668×10^{-5}	0.639×10^{-5}

The uncorrected dN/dt for the four elements used in the A dependence analysis is plotted in Figs. (IV. F. 1-4). A clear diffractive peak from nuclear coherence that steepens dramatically with increasing A is evident. The results of fits to these data are in Table (IV. F. 2). Note that we also fit the beryllium energy dependence data over this energy region to obtain a result for $d\sigma/dt|_0$ within one standard deviation of the weighted average of the energy-dependence points, and it is this value that is used to calculate the HC efficiency. Thus the two Be entries for $d\sigma/dt|_0$ in Table (IV. F. 2) are equal by construction. The values of parameters C_2 and C_4 must be interpreted cautiously for reaons we have already given. In particular, the C_4 (incoherent slope) for Pb is not a measure of the true incoherent production because the secondary coherent diffraction maxima in Pb severely distort the region just outside the coherent peak where incoherent production becomes dominant in lighter nuclei. We defer discussion of the optical-model fits to these data and present them along with results on the ρ' optical-model fits in Section II.

G. ρ' Photoproduction A Dependence Analysis

In the analysis of $\rho' \to \pi^+\pi^-\pi^+\pi^-$ photoproduction (here after $\rho' \to 4\pi$) we follow as closely as possible the procedures used in $\rho \to \pi^+\pi^-$ energy and A dependence analyses just discussed. Certain features are special to the ρ' analysis, and we cover these here. The data are taken from the same triggers and the same runs as the $\rho \to \pi^+\pi^-$. We discuss the event selection from the sample on beryllium with the diffractive trigger first, and then give percentages for the other targets with the HC-diffractive trigger.

9830 events are available with 4 tracks through the spectrometer, net charge zero and the diffractive trigger, type (TSB) 14. Next, a target

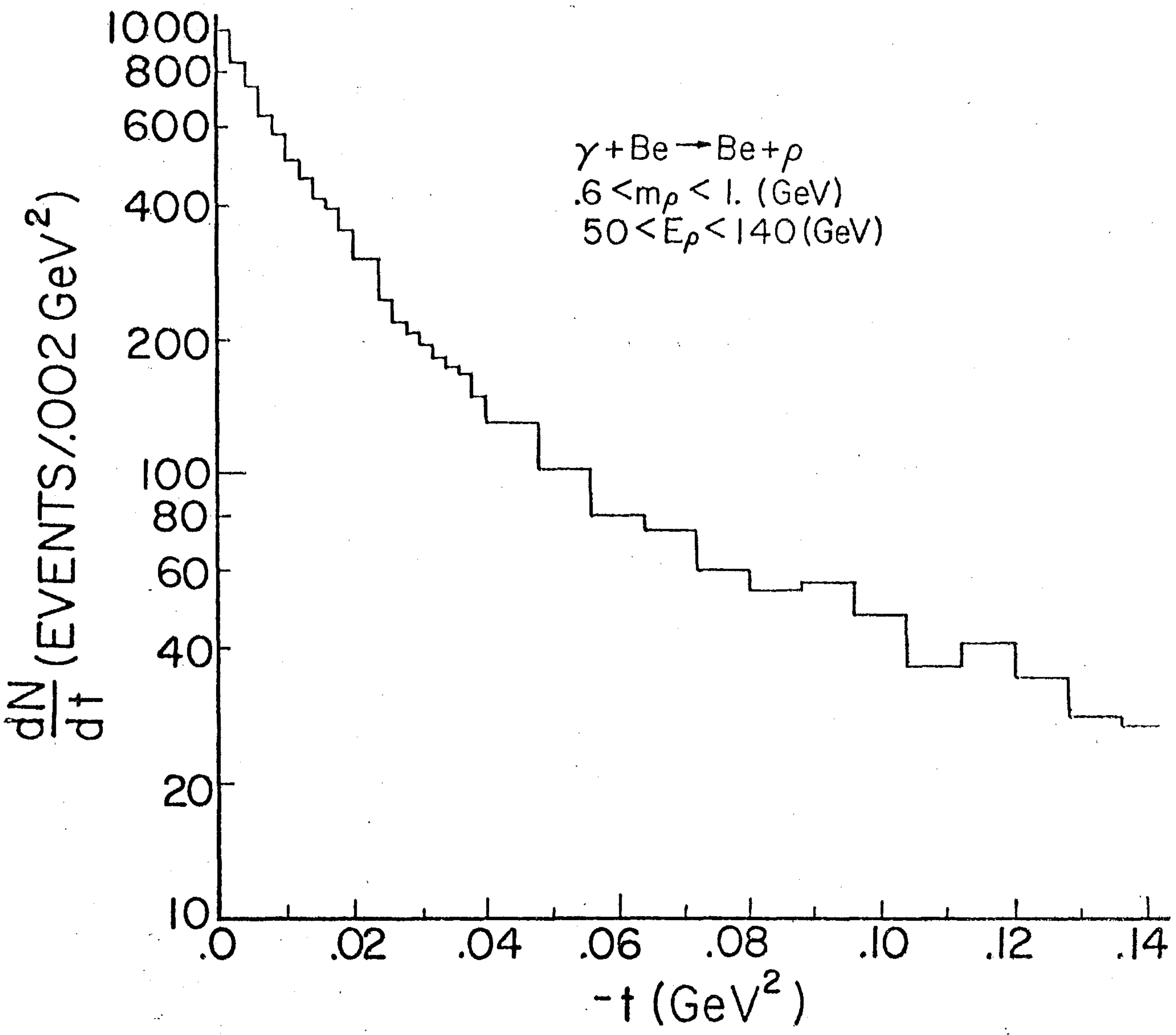

Fig. (IV.F.1) t dependence of ρ photoproduction from berylium, not corrected for acceptance or resolution.

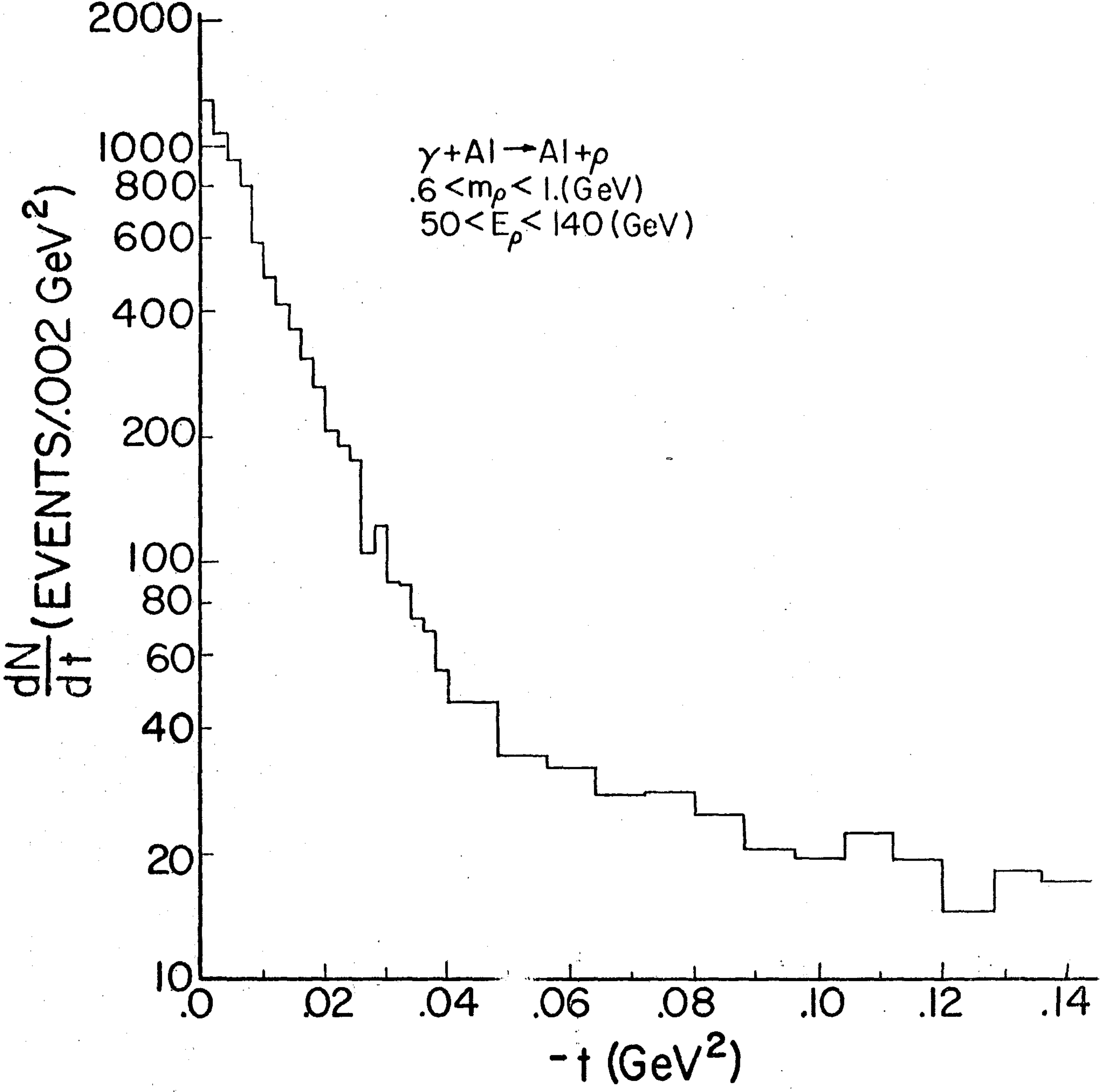

Fig. (IV.F.2) t dependence of ρ photoproduction from aluminum, uncorrected for acceptance or resolution.

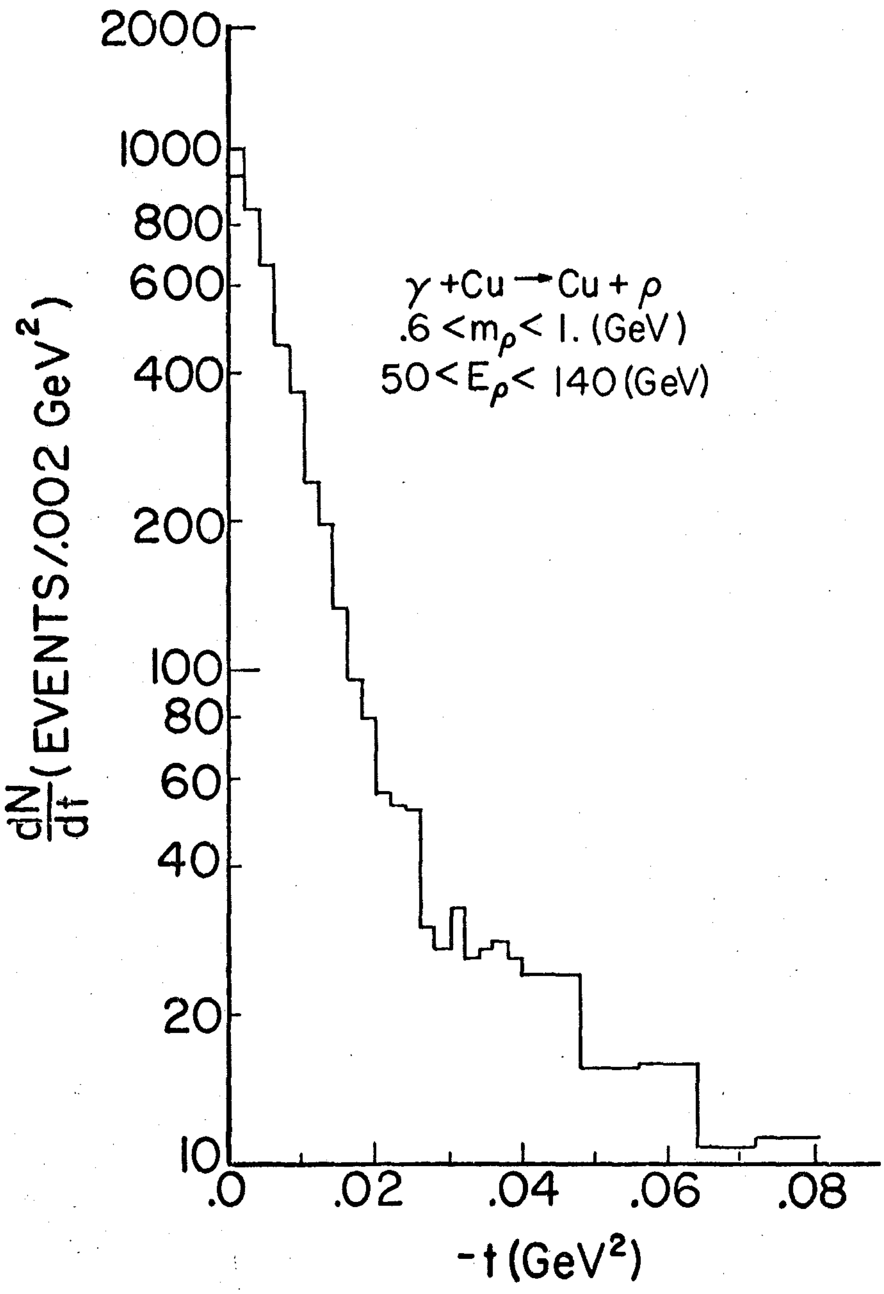

Fig. (IV.F.3) t dependence of ρ photoproduction from copper, not corrected for acceptance or resolution.

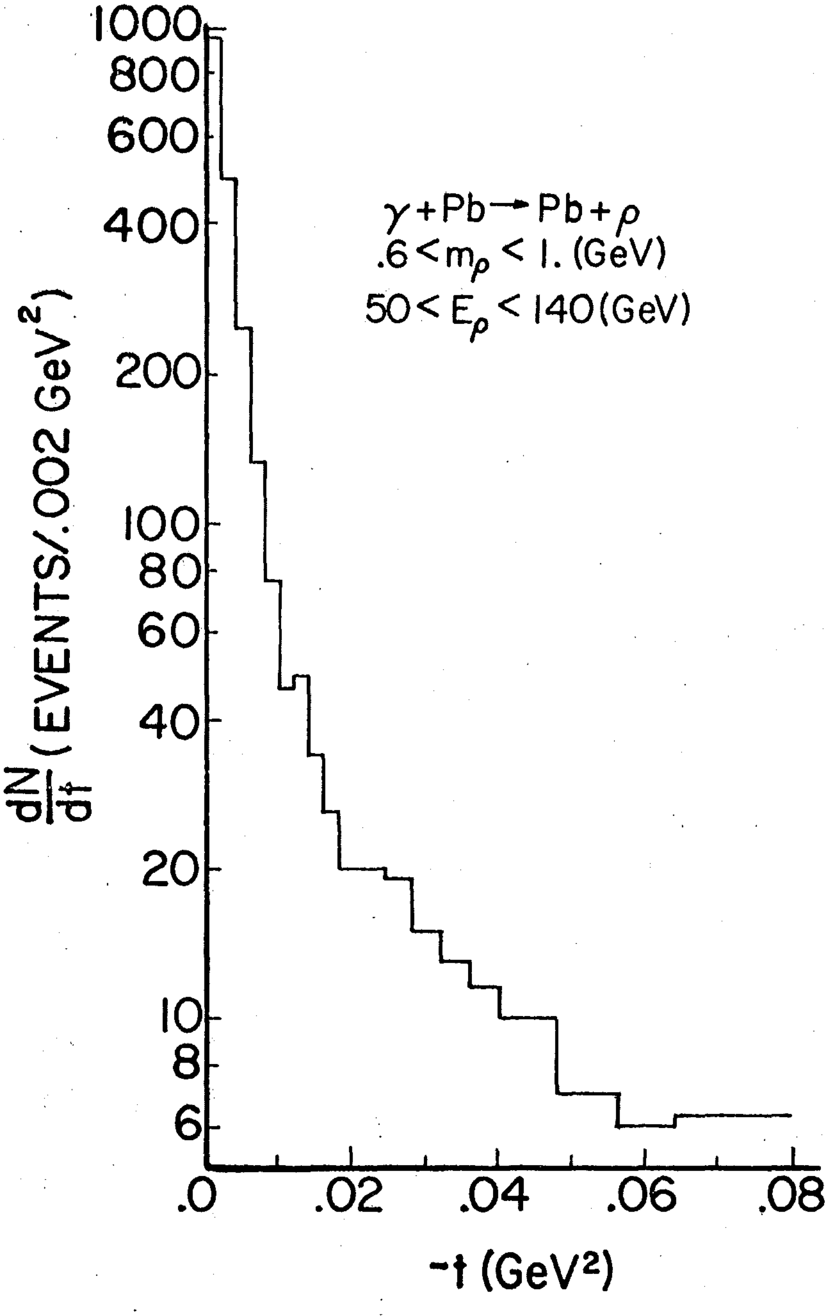

Fig. (IV.F.4) t dependence of ρ photoproduction from lead, not corrected for acceptance or resolution.

Table (IV.F.2). $\gamma + A \rightarrow A + \pi^+\pi^-$, Results of Fits to Data From Four Targets with HC Threshold in Trigger. $-t < 0.2$ GeV^2 and $0.6 < m_{\pi\pi} < 1$ GeV. The Range of 2π Energy, E_ρ, Is 50 to 140 GeV. For the Form of the Fit, See Eq. (IV.D.4).

Element	$\left.\frac{d\sigma}{dt}\right\|_0$ (mb/GeV^2)	C_3 (GeV^{-2})	C_4 (GeV^{-2})	C_2
Be (No HC)	3.30±0.06	66.7±2.0	9.9±0.5	5.9±0.4
Be	3.30±0.07	61.5±2.5	8.9±0.7	6.7±0.7
Al	19.6±0.4	95.7±2.1	6.6±0.7	29±3
Cu	71.4±1.8	160±4	9.1±0.9	47±4
Pb	389±15	361±12	17.5±1.3	53±5

requirement is made on the origin of the tracks. All six 2-track vertex combinations are made and rejected on distance of closest approach greater than 0.2 inches or parallelism. At least 5 of 6 combinations must pass that cut and 8190 events survive. The average Z position is then calculated for the pairings that pass and the event is rejected if this is more than 12 inches upstream or downstream of the target center. This cut is very clean and clearly removes interactions in the B3 trigger counter downstream of the target. 5750 events survive this stage. Requiring the B3 counter reduces the number of events to 5670. The same geometrical requirements are then made that were used for $\rho \rightarrow \pi^+\pi^-$. The aperture such as the magnet opening and PWC active area are made at the Monte Carlo stage for all four tracks. 5500 events survive to enter the binning process. The t binning is as for $\rho \rightarrow 2\pi$ and the 4π mass is binned in 50-MeV bins from 500 to 2500 MeV (0.5 to 2.5 GeV).

In order to get a feeling for the data that are contained in our matrix, one can look ahead at Fig. (IV. G. 1) and those following.

The Monte Carlo is a modified form of the $\rho \rightarrow \pi^+\pi^-$ version and different in the following ways. Four particles of pion mass and net charge zero are generated instead of two particles. The parent mass is sampled from a simple Breit Wigner of central mass 1.6 GeV and width of 0.8 GeV superimposed on a flat term of 1/3 as many events. This distribution is generated from 0.6 to 3.0 GeV. The t distribution is formed of two exponentials from -2 GeV^2 down to t_{min} with the recoil calculated from a beryllium nucleus or a proton as in the $\rho \rightarrow \pi^+\pi^-$ case. The first slope is 50 GeV^{-2}, the second slope is 7 GeV^{-2}, and the ratio of the intercepts at $t = 0$ is 7. The four-pion decay is done according to uniform phase space. Note that the mass and t distributions generated in the Monte Carlo are chosen for convenience and will be reweighted to match the data at the fitting stage.

Previous work on the ρ' by [Schachet et al., 1974] and others suggests that $\rho^0\pi^+\pi^-$ is a prominent decay mode of the ρ', however, our interest in the ρ' is focused on its production mechanism on nuclear targets and not on the dynamics of its decay distribution. Consequently, we have made no attempt to unfold the decay dynamics from our data, but rather have investigated only those properties of the decay process which could influence the optical-model analysis. Specifically, the four-pion acceptance could depend upon the dynamics of the decay process. We have checked the acceptance corrected four-pion mass distribution under two different assumptions for the model by which the ρ' decays: four-body phase space and decay through an intermediate ρ. We find that the four-pion mass acceptance correction is completely insensitive to these different decay models.

Because we must deal with the HC trigger data again, we check the relative efficiency of this trigger as a function of $E_{\rho'}$ by examining the ratio of low t production of four pions from Be and Pb with the HC requirement to Be without the HC requirement. These ratios are energy independent above 60 GeV and have values consistent with those obtained for the ρ. The HC efficiency is better measured in the ρ case and the efficiency measured for ρ' data is consistent with the 95% value obtained with ρ data. Based on this information and guided by our experiences with the ρ we choose the region in $E_{\rho'}$ from 60 to 180 GeV for final analysis, and we use an HC efficiency of 95%. All quoted cross sections for the ρ' contain this correction.

The fitting of the $\rho' \to 4\pi$ data follows that used on $\rho \to 2\pi$ with the following differences. The mass distribution is fitted to Eq. (IV. D. 2) with C_5 and C_6 set to zero and $\Gamma_{\rho'}$ and $m_{\rho'}$ free parameters replacing the fixed values of Γ_ρ and m_ρ used earlier. Naturally $4\,m_\pi^2$ is replaced by $16\,m_\pi^2$ in Eq. (IV. D. 2b). In our initial fits to the mass distribution parameters C_2, C_3, and C_4 were taken from the ρ fits. The mass fit is performed over the interval 0.75 to 2.25 GeV, for events with -t less than 0.2 GeV^2. For the 30-run Be data we fit the mass dependence separately for $60 < E_{\rho'} < 120$ GeV and $120 < E_{\rho'} < 180$, as well as a combined region to test for consistency and stability of our acceptance correction. The values of $m_{\rho'}$ so obtained are quite consistent with each other. We also fit the mass dependence of Be and Al data with the HC-diffractive trigger. For all of these fits essentially identical values are obtained, $m_{\rho'} = 1487 \pm 20$ MeV. The width, $\Gamma_{\rho'}$, shows somewhat more variation than $m_{\rho'}$. We obtain $\Gamma_{\rho'} = 675 \pm 60$ MeV from the above fits. In t fits and calculation of cross sections for the A dependence data we have used a constant value for the mass and width of the ρ'. As we shall see, use of standard values of $m_{\rho'}$ and $\Gamma_{\rho'}$ somewhat different than our best determination does not affect our conclusions. Figures (IV. G. 1) and (IV. G. 2) show the uncorrected dN/dM for 4π production from Be and Al.

The t dependence of ρ' photoproduction from beryllium is shown in Fig. (IV. G. 3) for the data sample used in the ρ energy dependence analysis. Figure (IV. G. 4) shows the t dependence of ρ' photoproduction from the four targets we use in our A dependence analysis. The distributions include events with four-pion masses between 1 and 2 GeV and are not corrected for acceptance or resolution. The fits obtained to these data are in Tables (IV. G. 1) and (IV. G. 2). We have investigated our sensitivity to the values of $m_{\rho'}$ and $\Gamma_{\rho'}$ we use by performing t dependence fits using values of $m_{\rho'}$ varied by 5% and $\Gamma_{\rho'}$ varied by 25%. Together these relatively large variations induce less than 20% shift in normalization and do not effect other results.

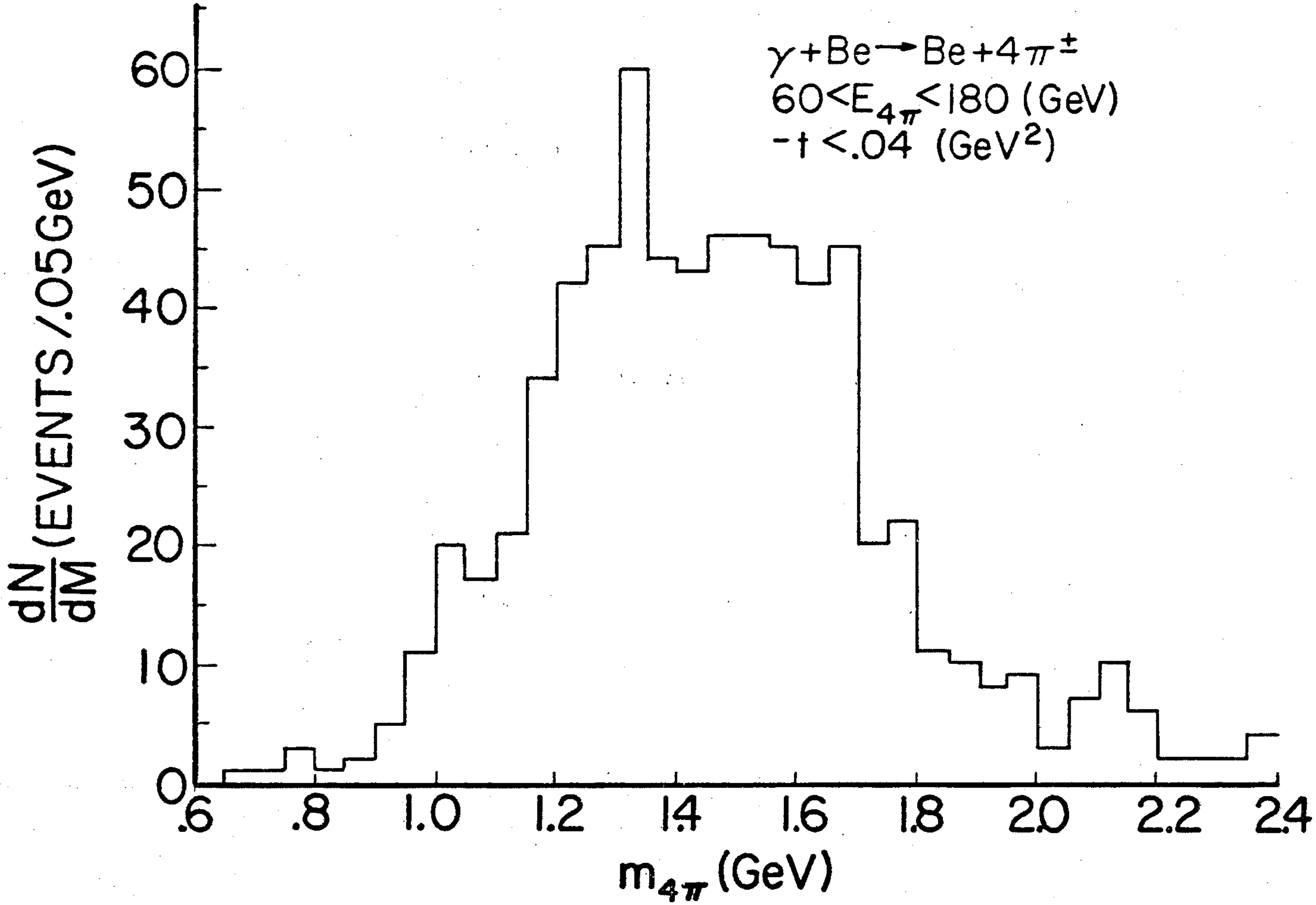

Fig. (IV.G.1) dN/dM for $4\pi^{\pm}$ photoproduction from beryllium, not corrected for acceptance or resolution.

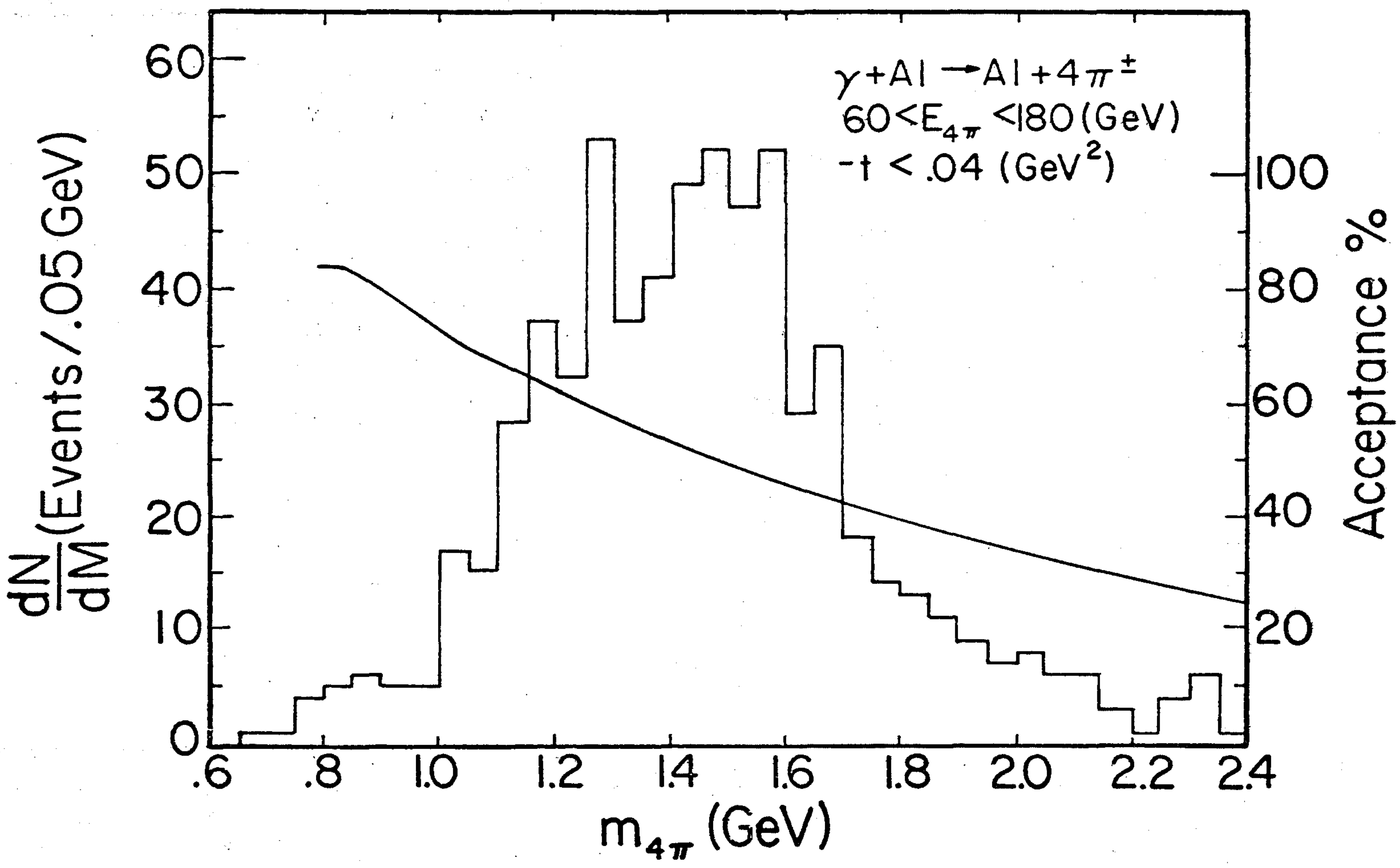

Fig. (IV.G.2) dN/dM for $4\pi^{\pm}$ photoproduction from aluminum, not corrected for acceptance or resoluticn. The acceptance curve is essentially identical for production from all target elements.

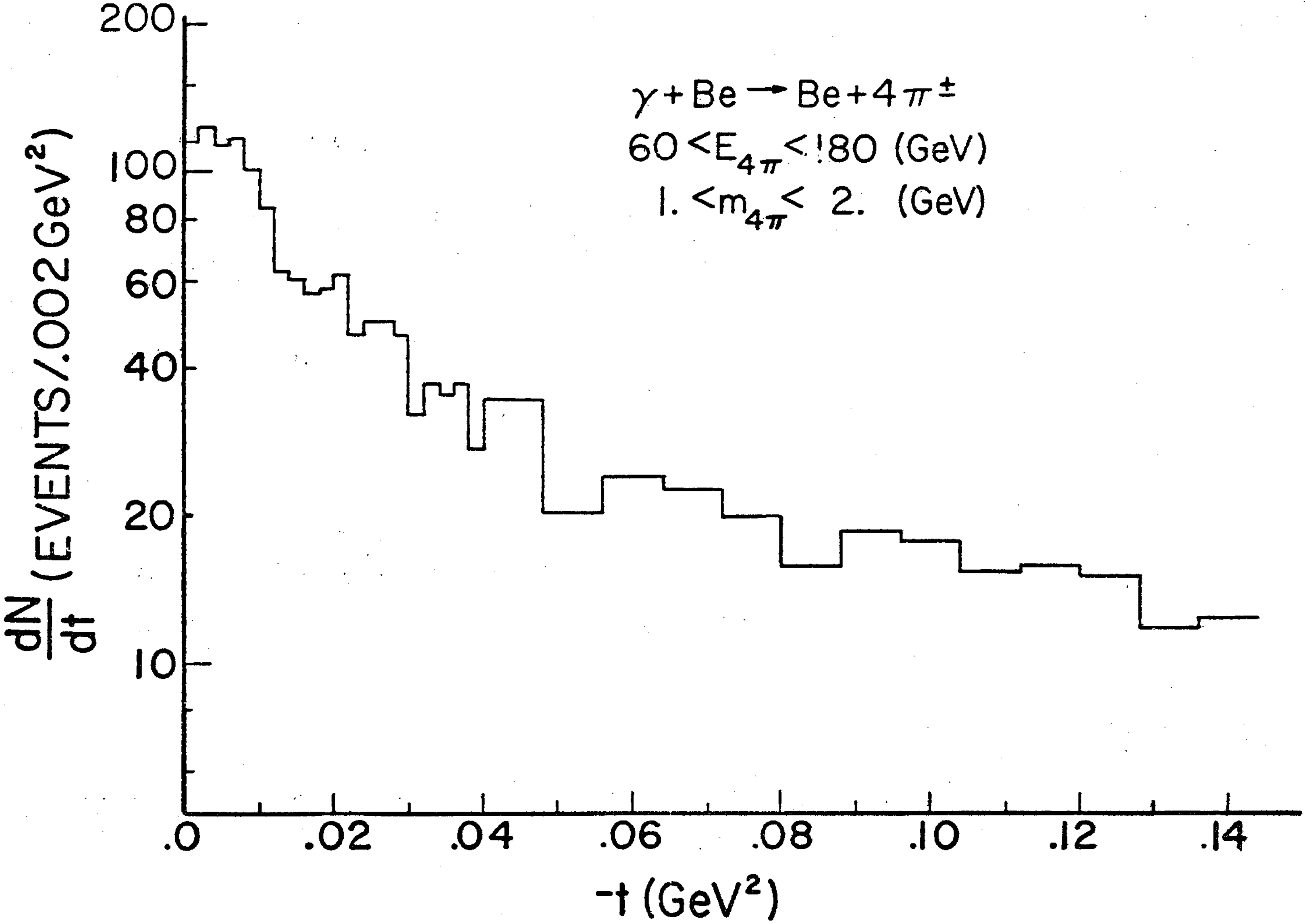

Fig. (IV.G.3). t dependence of $4\pi^{\pm}$ photoproduction from berylium, not corrected for acceptance or resolution.

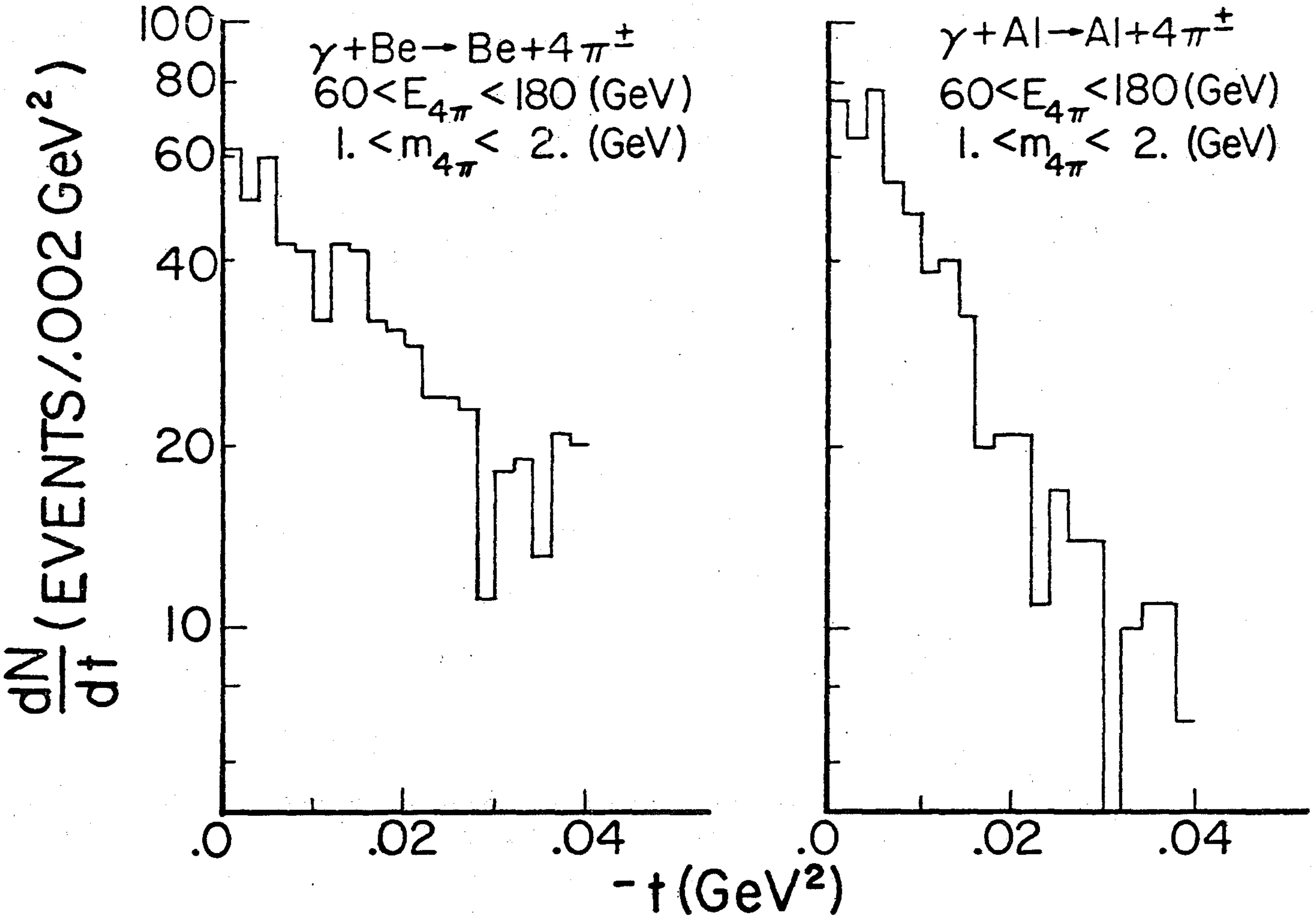

Fig. (IV.G.4a) and (IV.G.4b) t dependence of $4\pi^{\pm}$ photoproduction from berylium and aluminum, not corrected for acceptance or resolution.

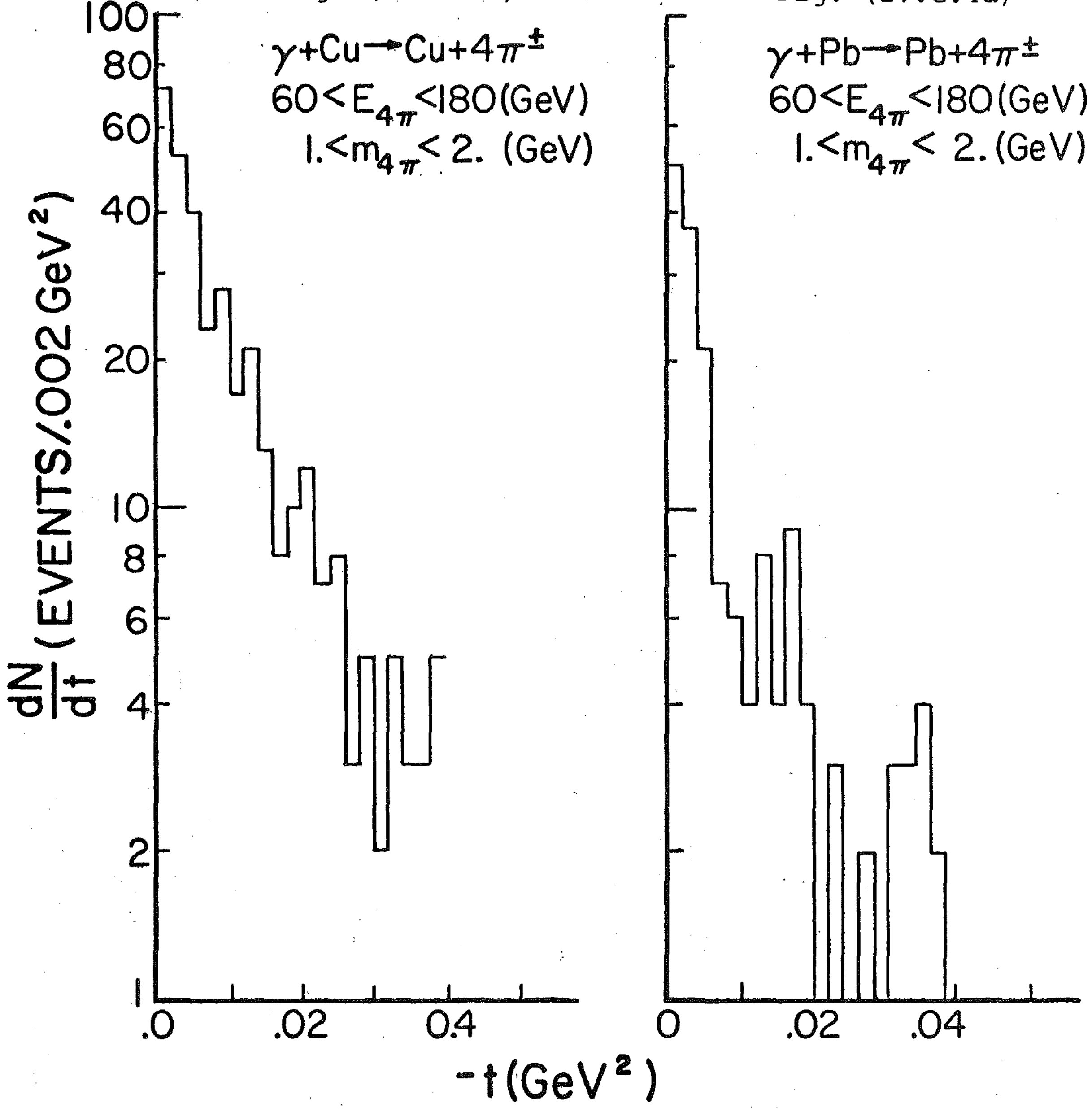
Fig. (IV.G.4c)

Fig. (IV.G.4d)

Fig. (IV.G.4c) and (IV.G.4d) t dependence of $4\pi^{\pm}$ photoproduction from copper and lead, not corrected for acceptance or resolution.

Table (IV. G. 1). Results of Fits to the t Dependence of ρ' Photoproduction from Beryllium for Two Ranges of 4-Pion Energy ($E_{\rho'}$) and a Total Range. The Fits Include Data with $-t < 0.2$ GeV^2 and Assume $m_{\rho'} = 1460$ MeV and $\Gamma_{\rho'} = 600$ MeV. [See Eq. (IV. D. 4) for the Form of the Fit.]

$E_{\rho'}$ (GeV)	$\left.\frac{d\sigma}{dt}\right\|_0$ (mb/GeV^2)	C_3 (GeV^{-2})	C_4 (GeV^{-2})	C_2
60-120	0.613±0.044	71.0±8.9	5.54±1.10	4.22±0.70
120-180	0.530±0.061	59.4±13.2	4.51±1.87	3.91±1.17
60-180	0.586±0.035	65.4±7.1	5.09±0.95	4.15±0.61

In Table (IV. G. 2) we show two fits to the ρ' A dependence data. One of these is conventional, but the other uses constrained values for the C_3 and C_4 parameters (the coherent and incoherent t slopes) and fits only over the restricted t range $-t < 0.01$ GeV^2. We are motivated to perform this second fit by noticing that C_3 is within about one standard deviation of the values obtained in the $\rho \rightarrow 2\pi$ fits. Since the statistics were much better on the $\rho \rightarrow 2\pi$ fits and the C_4 parameter is unimportant at low t we fix both C_3 and C_4 to the $\rho \rightarrow 2\pi$ values obtained earlier. This should give a better value for the intercept ($d\sigma/dt|_0$) if we assume that the coherent behavior of $\rho' \rightarrow 4\pi$ and $\rho \rightarrow 2\pi$ is the same.

H. Optical Model Analysis of A Dependence of ρ and ρ' Photoproduction

We have discussed the optical model of vector meson photoproduction from nuclei in Section II and in Appendix A. We reiterate the type of result we are seeking and our philosophy of applying the optical model to our data here very briefly before discussing the results.

The forward cross sections ($d\sigma/dt|_0$) for ρ and ρ' production from the previous sections are the input to the optical model analysis. From the A dependence of vector meson production independent of overall normalization, we obtain the

Table (IV.G.2). Results of Fits to the t Dependence of ρ' Photoproduction From Four Targets for 4 Pion Energy ($E_{\rho'}$) Between 60 and 180 GeV. The Fits Include Data with $-t < 0.2$ and C_3 and C_4 Free Parameters or with $-t < 0.01$ and C_3 and C_4 Constrained to Values Obtained for $\rho \rightarrow 2\pi$ from the Same Runs [See Table (IV.F.3).] $m_{\rho'} = 1460$ MeV and $\Gamma_{\rho'} = 600$ MeV [See Eq. (IV.D.4) for the Form of the Fit.]

Target	$\left.\frac{d\sigma}{dt}\right\|_0$ (mb/GeV^2)	C_3 (GeV^{-2})	C_4 (GeV^{-2})	C_2
Be	0.615±0.050	69.1±11.0	5.45±1.23	3.68±0.71
Be	0.606±0.069	—	—	—
Al	3.61±0.27	103.1±9.6	5.64±1.30	11.2±1.9
Al	3.12±0.32	—	—	—
Cu	11.4±1.1	145±15	6.1±1.9	21.9±4.8
Cu	12.1±1.3	—	—	—
Pb	59.7±8.5	317±39	8.7±2.6	41.0±11.4
Pb	65.9±7.4	—	—	—

vector meson-nucleon total cross section, $\sigma_{\rho'}$ or σ_ρ. We use fixed values of α_ρ or $\alpha_{\rho'}$, the ratio of real to imaginary parts of the forward vector meson scattering amplitudes. The overall normalization of the data from all targets gives the forward hydrogen cross section which can be interpreted via vector dominance arguments in terms of the photon-vector meson couplings $f_\rho^2/4\pi$ and $f_{\rho'}^2/4\pi$ and the already determined σ_ρ and $\sigma_{\rho'}$ respectfully. Because of possible uncertainties in our overall normalization due to the use of the quantameter to normalize production in our broad-band beam, discussed briefly in Section III, we use ratios of ρ and ρ' normalizations wherever possible to extract results. This exploits one of the real strengths of our apparatus and mode of taking data. Due to the fact we take two-particle and four-particle data at the same time, much of the relative error in normalization cancels out.

We exhibit again the form of the optical model we use for coherent production from nuclei. Here we have split the equation into real and imaginary parts and squared them to obtain the square of $N_{eff}(t)$ in a form suitable for implementation on a computer. The notation is that of Appendix A.

$$|N_{eff}(t)|^2 = \left\{ 2\pi \int_0^\infty bdb\, J_0(q_\perp b) \int_{-\infty}^{+\infty} dz\, \tilde{n}\, e^{-\frac{1}{2}\sigma_\rho \tilde{T}} \left[\cos(q_\parallel z) \cos\left(\frac{\sigma_\rho \alpha_\rho}{2} \tilde{T}\right) - \sin(q_\parallel z) \sin\left(\frac{\sigma_\rho \alpha_\rho}{2} \tilde{T}\right) \right] \right\}^2 + \left\{ 2\pi \int_0^\infty bdb\, J_0(q_\perp b) \int_{-\infty}^{+\infty} dz\, \tilde{n}\, e^{-\frac{1}{2}\sigma_\rho \tilde{T}} \left[\cos(q_\parallel z) \sin\left(\frac{\sigma_\rho \alpha_\rho}{2} \tilde{T}\right) + \sin(q_\parallel z) \cos\left(\frac{\sigma_\rho \alpha_\rho}{2} \tilde{T}\right) \right] \right\}^2 . \quad \text{(IV.H. 1)}$$

In particular, $\tilde{n}(\vec{b}, z)$, the optical density of the nucleus and $\tilde{T}(\vec{b}, z)$ are defined as follows:

$$\tilde{T}(b,z) = \int_z^\infty \tilde{n}(b,z')\,dz' \qquad \text{(IV.H. 2)}$$

$$\tilde{n}(r) = n_0\left(1 + e^{(r-C)/z_f}\right)^{-1} \qquad \text{(IV.H. 3)}$$

$$\frac{d\sigma}{dt} = |f_{0_\rho}|^2\,|N_{\text{eff}}(t)|^2 \qquad \text{(IV.H. 4)}$$

Equation (IV. H. 4) is the statement of the coherent optical model and $|f_{0_\rho}|^2$ is the square of the forward amplitude for ρ photoproduction. Here as in all the above relations the ρ and ρ' are interchangeable. r is just $(b^2 + z^2)^{\frac{1}{2}}$. z_f is 0.545 fm and $C = C_0 A^{1/3}$ with $C_0 = 1.12$ fm. n_0 is determined so that the volume integral of $\tilde{n}$ over all space is equal to A.

Encouraged by the success of [Spital and Yennie, 1974b] in using only the coherent optical model to fit small t ρ photoproduction from nuclei we use this model without any incoherent correction to fit $d\sigma/dt|_0$. Because the optical model formula is not trivial to implement on the computer and involves some numerical work, we test our program on data successfully analyzed by previous workers. This also tests the validity of some physical approximations we make, such as ignoring nuclear correlations. To test the model we use it to fit the 8.8-GeV ρ photoproduction data of the Cornell Group [McClellan, 1971], as given in [Spital and Yennie, 1974b], Table III of their article. Besides deuterium which is not relevant to our analysis, they have 8 elements. We divide them into two groups of four, one group consisting of Be, Mg, Cu, and Pb, the other of C, Ag, In, and Au. Except for the Mg and Al, which are adjacent elements in the periodic table, the first sample of four elements is just those we have to work with. They give $d\sigma/dt|_{t_{min}}$ and we use the approximation $t_{min} = -(m_\rho^2/2k)^2$; we use their errors and, for this test, the value of α_ρ preferred by Spital and Yennie, -0.2. For their equivalent analysis of all nine elements, Spital and Yennie obtain $\sigma_\rho = 25.9 \pm 0.6$ (mb) and $|f_0|^2$ = 103±2% (μb/GeV^2). This is to be compared with values of σ_ρ of 25.2±1.1 mb and 24.4±0.8 mb for the first and second data subsamples respectively. The two values for $|f_0|^2$ that we obtain are 106.9±3.4 μb/GeV^2 and 102.9±2.8 μb/GeV^2. Considering that we have left out the deuterium data and subdivided the remaining data, these results are in surprisingly good agreement, thus removing any doubts about our implementation of the optical model, at least for forward production as we plan to use it.

We make one further test on the Be, Mg, Cu, and Pb samples of the Cornell 8.8-GeV data to explore the dependence of the fits on the values of C_0 used in $C_0 A^{1/3}$. As well as the value of 1.12 fm preferred by the extensive analysis of ρ photoproduction by [Alvensleben et al., 1970], we fit to C_0 = 1.22 fm and C_0 = 1.02 fm. The effect this has on $|f_0|^2$ is small, approximately ±2%, however, the effect on σ_ρ is much larger, approximately ±13%. Both variations are in the same direction as the variation in C_0 (±9%). This same variation in C_0 applied to our data gives somewhat larger variations of ±4% and ±17% for $|f_0|^2$ and σ_ρ respectively. We make other tests on our data as well which we will only give the results for. Changing details of the numerical integration, such as step size by a factor of 2, has less than 0.5% effect on either quantity. Changing α_ρ to 0 from -0.2 increases $|f_0|^2$ by 1% and σ_ρ by approximately 2.5%. A change in z_f by approximately ±9% gives approximately a ±4% variation in $|f_0|^2$ and ±0.5% variation in σ_ρ. From this we see that the most important parameter of the model is C_0 and its effect is primarily on σ_ρ.

The results of our optical-model fits to the ρ and ρ' data in Tables (IV. F. 2) and (IV. G. 2) are contained in Table (IV. H. 1). For the ρ' we have chosen $\alpha_{\rho'}$ = 0, for the ρ we show fits for both α_ρ = -0.2, favored by the low-energy data, and

$\alpha_\rho = 0$. The phase of πp scattering has been measured and it approaches zero in the range of energy we use in this analysis [Lach, 1977], thus motivating the fits at $\alpha_\rho = 0$. We make no t_{min} corrections to $d\sigma/dt|_0$ for either ρ or ρ'.

Table (IV. H. 1). Optical Model Fits to the Data in Tables (IV. F. 3) and (IV. G. 5) of $d\sigma/dt|_0$ for ρ and ρ' Photoproduction from Be, Al, Cu, and Pb Targets. Errors Are Statistical Only.

Final State	σ_ρ or $\sigma_{\rho'}$ (mb)	$\lvert f_0\rvert^2$ (μb/GeV^2)	Comments
2π	37.9±1.6	66.5±2.3	$\alpha_\rho = -0.2$
2π	38.9±1.7	67.1±2.4	$\alpha_\rho = 0$
4π	48.9±7.7	14.5±2.1	
4π	40.3±7.2	12.0±2.0	t fit for $-t < 0.01$ and C_3, C_4 from ρ → 2π

Naturally in Table (IV. H. 1) 2π is for $\rho \rightarrow \pi^+\pi^-$ and 4π is for $\rho' \rightarrow \pi^+\pi^-\pi^+\pi^-$, but this notation is a reminder that we are only looking at the four-charged pion decay of the neutral ρ'. We do not make any attempt to correct for the branching ratio of the ρ' into this state, which to the best of our knowledge has not been measured. With the ρ → 2π this is not a problem as the branching ratio in this case is practically 100%. An additional check is made on the self-consistency of the ρ data points which we do not exhibit in Table (IV. H. 1). Fits are made excluding data from each of the targets in turn, yielding results for σ_ρ and $|f_0|^2$ that are within the statistical errors quoted in the table. The errors are statistical and are misleadingly small due to the fact that they do not reflect uncertainty in the form and parameters used in the model.

J. Discussion of ρ → 2π and ρ' → 4π Results

We intend to ratio ρ and ρ' results whenever possible to eliminate systematic biases from our results. No data besides our own exist for ρ' photoproduction from nuclei larger than deuterium or at photon energies above 20 GeV. However, we compare our results to some of those obtained at the lower energies as well as theoretical predictions of vector meson dominance. This process is aided by the existence of preprints of two chapters from the forthcoming Electromagnetic Interactions of Hadrons, Eds. Donnachie and Shaw; these are [Leith, 1977] and [Grammar and Sullivan, 1977]. The later preprint covering nuclear shadowing has come to our attention after our analysis was completed; however, it is quite useful as a review of generalized vector meson dominance (GVMD) as well as nuclear photoprocesses.

From the discussion of the ρ' in the vector-dominance model from Chapter II, we recall that GVMD in the diagonal approximation requires that σ_V, the vector meson-nucleon total cross section decrease as m_V^{-2} for members of each vector meson family. If we use our values for $m_{\rho'}$ obtained from the fit to the p-wave Breit-Wigner mass distribution, we obtain for the ratio of ρ' and ρ cross sections the following result under that assumption.

Predicted by diagonal GVMD

$$\frac{\sigma_{\rho'}}{\sigma_\rho} = \frac{m_\rho^2}{m_{\rho'}^2} = \left(\frac{770}{1487\pm20}\right)^2 = 0.27\pm0.01. \qquad \text{(IV.J. 1)}$$

We have used the standard value for the ρ mass from the [Particle Data Group, 1976] and the weighted average of $m_{\rho'}$ determined from our Be and Al data. The error is an estimate of the uncertainty of that particular set of fits and probably is an underestimate of our total uncertainty in the ρ' mass from such things as interfering nonresonant backgrounds, etc. Since we measure both quantities on the LHS of (IV.J. 1) we can evaluate it directly from the A-dependence results.

Measured $$\frac{\sigma_{\rho'}}{\sigma_{\rho}} = \frac{40\pm7}{38} = 1.05\pm0.18. \qquad \text{(IV.J. 2)}$$

Here we have used the results of Table (IV. H. 1) and the statistical errors from the ρ's which dominate since the same model was used for both analyses.

Comparing (IV. J. 1) and (IV. J. 2) it is clear that the diagonal GVMD requirement of (IV. J. 1) is not borne out by the data, which is entirely consistent with $\sigma_{\rho} = \sigma_{\rho'}$. A result obtained by comparing ρ' production from hydrogen [Davier et al., 1973] and storage-ring production of ρ' [Grilli et al., 1973] along with the assumption of VMD has already indicated that σ_{ρ} and $\sigma_{\rho'}$ might be comparable [Grammar and Sullivan, 1977].

By using the ratio of $\sigma_{\rho'}$ to σ_{ρ} and $d\sigma/dt|_0$ for ρ and ρ' production, we can extract the ratio of photon-vector meson coupling constants for the ρ and ρ' using vector meson dominance. We shall assume that the ρ' and ρ nuclear cross sections are identical, as implied by the result (IV. J. 2). We shall also assume that $\rho \leftrightarrow \rho'$ transistions are suppressed (diagonal approximation). Alternately we can consider a nondiagonal GVMD with only transitions between neighboring states, such as that of [FRS, 1975]. In this model the ρ and ρ' are not supposed to be adjacent states. In this approximation, VMD implies the following [Silverman, 1975], [Leith, 1977].

$$R = \frac{\left.\frac{d\sigma}{dt}\right|_0 (\rho)}{\left.\frac{d\sigma}{dt}\right|_0 (\rho')} = \frac{f_{\rho'}^{\,2}}{f_{\rho}^{\,2}} . \qquad \text{(IV.J. 3)}$$

For our data using the $|f_0|^2$ for ρ and ρ' photoproduction and including a systematic error encompassing our full uncertainty in the ρ't dependence, we obtain R' = 5.6±1.1. The reason we place a prime on this value is that we measure only the ρ' to four-charged pion decay mode and in R we must have $d\sigma/dt|_0(\rho')$

for all modes. The simplest assumption is to correct the $\pi^+\pi^-\pi^+\pi^-$ mode by 3/2 to account for the I = 1 (isospin) contribution from a $\pi^+\pi^-\pi^o\pi^o$ decay and further assume that $\rho' \rightarrow 2\pi$ is small. On this last point see [Silverman, 1975] and [Leith, 1977], where among other preliminary data a result from our group indicates $\rho' \rightarrow 2\pi$ is small but nonvanishing. This prescription at least has the advantage of uniformity with past practice, so we define R = 2/3 R'. If we use the currently accepted value of $f_\rho^2/4\pi = 2.54$ as given by most recent reviewers of this topic [Leith, 1977], then we obtain for $f_{\rho'}^2/4\pi$ the following result, using our value of R'.

$$f_{\rho'}^2/4\pi = \frac{2}{3} R' \times f_\rho^2/4\pi = 9.5\pm1.9. \qquad \text{(IV.J. 4)}$$

Using the same assumptions about ρ' branching ratios, the storage-ring result of [Grilli et al., 1973] is 11.2±2 which is in good agreement with our result. [Alexander et al., 1975] have measured four-charged pion photoproduction from deuterium in the bubble chamber to determine R = 6.0±1.2. This is not in particularly good agreement with the e^+e^- colliding-ring result for the photon-ρ' coupling constant as it implies $f_{\rho'}^2/4\pi = 15.2\pm3.0$, using $f_\rho^2/4\pi = 2.54$. This result is also not in particularly good agreement with our result, with no single point possible within all three errors.

GVMD in either the diagonal or nondiagonal form needs the following relationship between coupling constants in a family of vector mesons.

$$\frac{f_{\rho'}^2}{f_\rho^2} \equiv R = \frac{m_{\rho'}^2}{m_\rho^2}. \qquad \text{(IV.J. 5)}$$

Using the usual ρ' branching-ratio assumption, we have evaluated the LHS of (IV.J. 5) as 3.7±0.7 to be compared to the RHS (IV. J. 1 inverted) 3.7±0.1. Our data combined with a branching-ratio assumption thus gives nice agreement with this part of GVMD.

We have already discussed our mass distribution briefly and have $m_{\rho'} = 1487 \pm 20$ MeV, from fits to the Be and Al data at $-t < 0.2$. We use a mass distribution that is modeled on the one used for the ρ. Previous workers have used a variety of parametrizations and as a consequence have obtained a variety of estimates for the mass and width of the ρ'. In the case of the photoproduction from hydrogen, the contribution from a variety of nondiffractive exchanges and kinematic reflections complicates the mass spectrum. The Δ^{++} (a $\pi^{+}p$ resonance at about 1236 MeV) has been a special problem for these measurements. All these effects are unimportant for us, due to the high energy we use (> 60 GeV) and more importantly the use of data from the strong nuclear coherent peak in the t distribution. The consistency of this nuclear coherence with that seen in the ρ is proof of the diffractive nature of the production and strong evidence that the ρ', like the ρ, is a vector meson. In any case, we see a clean mass peak with a $\Gamma_{\rho'} = 675 \pm 60$ MeV. An inspection of the results of the low-energy ρ' experiments that we have been quoting shows that our mass distribution is the "cleanest" and most obviously background free ρ' photoproduction data available. A wide range of values of $m_{\rho'}$ and $\Gamma_{\rho'}$ have been reported, as can be seen by inspecting the [Particle Data Group, 1976] entry under ρ'(1600). We compare our results with a photoproduction experiment and choose [Schacht et al., 1974], partially because they analyze their data in two ranges of photon energy, 5.5 to 9.0 and 9.0 to 18.0 GeV. For these two regions they obtain 1550±50 MeV and 1450±100 MeV for $m_{\rho'}$, values in fair agreement with ours. $\Gamma_{\rho'}$ gave them more trouble particularly at low energy where the ρ' was not the largest part of their signal. They obtained 400±50 MeV and 850±100 MeV for $\Gamma_{\rho'}$. It is certainly true that the mass and width of the ρ' are not well understood at present. If we recall that the mass spectrum of the ρ daughters used by GVMD and motivated by the Veneziano model is $m_n^2 = m_\rho^2 (1 + 2n)$ and that our ρ' is supposed to be n = 2 member of the family, this model gives a mass (1700 MeV) on the upper limit of any reported.

K. Summary and Conclusions

We have measured the energy dependence of forward ρ photoproduction from beryllium over the momentum range from 30 to 160 GeV. We obtain a cross section that is consistent with the constant value $d\sigma/dt|_0 = 3.42 \pm 0.28\ \mu b/GeV^2$ over the entire range. When fit to exponentials the coherent and incoherent t (- momentum transfer squared) slopes are $67 \pm 2\ GeV^{-2}$ and $9.9 \pm 0.5\ GeV^{-2}$ for this momentum range and are consistent with previous measurements of this process. The errors quoted are statistical.

We have observed neutral 2- and 4-body photoproduction from beryllium, aluminum, copper, and lead targets using photons of 50 to 140-GeV momentum for two-body states and 60 to 180 GeV for four-body states. On all four elements sharp nuclear coherence peaks are observed at small t in both two- and four-body channels when analyzed as all pion final states. On all elements the coherent t slopes for 4π photoproduction are consistent with the better-determined slopes from 2π production and yield nuclear radii estimates in the range $1.1 \pm 0.1\ A^{1/3}$ fm for a Woods-Saxon nuclear density. For an optical model analysis of the 2π and 4π data we adopt the radii $1.12\ A^{1/3}$ fm with a Woods-Saxon density with no correlation corrections. This model is quite successful in fitting $d\sigma/dt_{\theta=0}$ for low energy ρ photoproduction.

The 2π production is dominated by the ρ (ρ^0, 770) for which we use a relativistic Breit Wigner mass distribution with a phenomenological interference from nonresonant 2π production. We input fixed values of ρ mass and width to all parts of the analysis, using 770 MeV and 150 MeV respectively. The 4π data are well fit by the same type of mass distribution as used for the ρ, with no background provision. We obtain a mass of 1487±20 MeV and a width of 675±60 MeV, attributing all of this signal to the ρ' [called ρ' (1600) or ρ' (1500) in the literature].

The optical model, applied to the ρ and ρ' data, provides us with a determination of the ratio of the ρ-photon and ρ'-photon coupling constants: $f_{\rho'}^2/f_{\rho}^2 = 3.7 \pm 0.7$. This result is in excellent agreement with the prediction of Generalized Vector Meson Dominance (GVMD): $f_{\rho'}^2/f_{\rho}^2 = m_{\rho'}^2/m_{\rho}^2 = 3.7 \pm 0.1$. By using the accepted value $f_{\rho}^2/4\pi = 2.54$ for the ρ-photon coupling constant, we extract the ρ'-photon coupling constant $f_{\rho'}^2/4\pi = 9.5 \pm 1.9$ in good agreement with the storage-ring results.

The A (nucleon number) dependence of ρ and ρ' photoproduction cross sections from nuclear targets are strikingly similar. Using the conventional assumptions embodied in the standard optical model of diffractive photoproduction from nuclei, we determine the ratio of the ρ'-nucleon to the ρ-nucleon total cross section: $\sigma_{\rho'}/\sigma_{\rho} = 1.05 \pm 0.18$. This result is totally inconsistent with the diagonal version of Generalized Vector Meson Dominance (GVMD), which predicts $\sigma_{\rho'}/\sigma_{\rho} = m_{\rho}^2/m_{\rho'}^2 = 0.27 \pm 0.01$. Both the standard optical model and the diagonal version of GVMD assume the absence of transitions between different vector mesons (e. g., $\rho \nrightarrow \rho' \nrightarrow \rho$). We interpret our measurement of $\sigma_{\rho'}/\sigma_{\rho} = 1.05 \pm 0.18$ as providing strong evidence for the necessity of including off-diagonal terms in GVMD.

As expected, high-energy photoproduction provides a fertile environment for testing models which attempt to describe the relationship between the photon and the vector mesons. This thesis has described the first high-energy photoproduction results to confront these models and has illustrated that the diagonal version of the Generalized Vector Meson Dominance model does not adequately describe the data.

LIST OF REFERENCES

[Alexander et al., 1975] Tel Aviv University preprint TAUP-481-75 (1975).

[Alvensleben et al., 1970] H. Alvensleben et al., Phys. Rev. Lett. 24, 792 (1970).

[Ballam et al., 1973] J. Ballam et al., Phys. Rev. D 7, 3150 (1973).

[Barger and Cline, 1969] V. Barger and D. Cline, Phys. Rev. 182, 1849 (1969).

[Bauer, 1971] T. H. Bauer, Phys. Rev. D 3, 2671 (1971).

[Chavin, 1976] S. Chavin, PhD Thesis, University of Illinois, unpublished (1976).

[Cormell, 1976] L. R. Cormell, Jr., PhD Thesis, University of Illinois (1976).

[Davier, 1973] M. Davier et al., Nucl Phys. B58, 31 (1973).

[Feld, 1969] B. T. Feld, Models of Elementary Particles, Blaisdell (1969).

[Feldman and Perl, 1977] G. J. Feldman and M. Perl, SLAC-PUB-1972 (July 1977) (T/E).

[Frazer and Fulco, 1960] W. R. Frazer and J. R. Fulco, Phys. Rev. 117, 1603 (1960).

[FRS, 1975 a] H. Fraas, B. J. Read and D. Schildknecht, Nucl. Phys. B86, 346 (1975).

[FRS, 1975 b] H. Fraas, B. J. Read and D. Schildknecht, Nucl. Phys. B88, 301 (1975).

[Giese, 1974] R. Giese, PhD Thesis, Stanford University (1974).

[Glauber, 1958] R. J. Glauber, Boulder Lectures in Theoretical Physics, Vol. 1 (1958); (Interscience Publ. N.Y. 1959).

[Glauber, 1967] R. J. Glauber, High Energy Physics and Nuclear Structure (North Holland, 1967) Ed. by G. Alexander.

[Glauber, 1970] R. J. Glauber, High Energy Physics and Nuclear Structure (Plenum Press, N.Y., 1970) Ed. by S. Devons.

[Grammar and Sullivan, 1977] G. Grammar, Jr. and J. D. Sullivan, ILL-(TH)-77-20 University of Illinois Report, June 1977.

[Greco, 1973] M. Greco, Nucl. Phys. B63, 398 (1973).

[Grilli et al., 1973] M. Grilli et al., Nuovo Cimento A 13, 593 (1973).

[Harris and Yount, 1974] F. Harris and D. Yount, Nucl. Instrum. Methods 114, 357 (1974).

[Joos, 1967] H. Joos, Acta Phys. Austriaca, Suppl. IV.

[Kendall, 1971] H. W. Kendall, in Proceedings of the 1971 International Symposium on Electron and Photon Interactions at High Energies, Ed. by N. B. Mistry, 247.

[Knauer, 1975] J. Knauer et al., in Proceedings of the Calorimeter Workshop, 215, Fermilab (1975).

[Kroll, Lee and Zumino, 1967] N. M. Kroll, T. D. Lee and B. Zumino, Phys. Rev. 157, 1376 (1967).

[Lach, 1977] J. Lach, Preprint FERMILAB-Conf-77/38-EXP, April 1977. Invited talk presented at XIIth Rencontre de Moriond, March 1977.

[Lee et al., 1970] W. Lee, NAL Experiment Proposal 87A, and Addendum, Fermi National Accelerator Laboratory (1970).

[Leith, 1977] D. W. G. S. Leith, SLAC-PUB-1878, Stanford Linear Accelerator Center Report, January 1977.

[Lipkin, 1966] H. J. Lipkin, Phys. Rev. Lett. 16, 1015 (1966).

[McClellan, 1971] G. McClellan et al., Phys. Rev. D 4, 2683 (1971).

[Nambu, 1957] Y. Nambu, Phys. Rev. 106, 1366 (1957).

[Particle Data Group, 1976] Particle Data Group, N. Barash-Schmidt et al., Rev. Mod. Phys. 48, No. 2, Part II, April 1976.

[Perl, 1975] M. Perl, SLAC-PUB-1614 (July 1975) (T/E).

[Ross and Stodolsky, 1966] M. Ross and L. Stodolsky, Phys. Rev. 149, 1172 (1966).

[Sakurai, 1960] J. J. Sakurai, Ann. Phys. 11, 1 (1960).

[Sakurai, 1969] J. J. Sakurai, Currents and Mesons, University of Chicago Press (1969).

[Sakurai and Schildknecht, 1972 a] J. J. Sakurai and D. Schildknecht, Phys. Lett. 40B, 121 (1972).

[Sakurai and Schildknecht, 1972 b] J. J. Sakurai and D. Schildknecht, Phys. Lett. 41B, 489 (1972).

[Sakurai and Schildknecht, 1972 c] J. J. Sakurai and D. Schildknecht, Phys. Lett. 42B, 216 (1972).

[Sarracino, 1976] J. S. Sarracino, PhD Thesis, University of Illinois (1976).

[Schacht et al., 1974] P. Schacht et al., Nucl. Phys. B81, 205 (1974).

[Shapiro, 1969] J. A. Shapiro, Phys. Rev. 179, 1345 (1969).

[Silverman, 1975] A. Silverman, review talk in the International Lepton-Photon Symposium, Stanford (1975).

[Söding, 1966] P. Söding, Phys. Rev. Lett. 19, 702 (1966).

[Spital and Yennie, 1974a] R. Spital and D. R. Yennie, Phys. Rev. D 9, 126 (1974).

[Spital and Yennie, 1974b] R. Spital and D. R. Yennie, Phys. Rev. D 9, 138 (1974).

[Stodolsky, 1967] L. Stodolsky, Phys. Rev. Lett. 18, 135 (1967).

[Veneziano, 1968] G. Veneziano, Nuovo Cimento A 57, 190 (1968).

[Wijanco, 1976] A. R. Wijanco, PhD Thesis, Columbia University (1976).

[Yennie, 1971] D. R. Yennie, Hadronic Interactions of Electrons and Photons, Proceedings of the 11th Session of the Scottish Universities Summer School in Physics, 1970, Eds. J. Cumming and H. Osborn.

[Zalewski, 1977] K. Zalewski, Frascati Preprint LNF-77/2(P), January 1977.

APPENDIX. OPTICAL MODEL OF VECTOR MESON PHOTOPRODUCTION FROM NUCLEI

Because the optical model is necessary for extracting the information on the basic reactions from photoproduction on nuclear targets we spend some time developing it. The basic ideas are present in the case of elastic scattering of a hadron from a nucleus so we will show that in some detail [Glauber, 1958, 1967, 1970] and then generalize to coherent and incoherent particle production more rapidly.

Let us start with the familiar partial wave expansion for scattering.

$$f(\theta) = \frac{1}{2ik} \sum_{\ell} (2\ell+1)\left(e^{2i\delta_\ell} - 1\right) P_\ell(\cos\theta). \tag{A.1}$$

$P_\ell(\cos\theta)$ are the Legendre polynomials, δ_ℓ is the phase shift for the ℓth partial wave, k is the particle momentum, and $f(\theta)$ is the scattering amplitude. This is merely the scattering solution to the Schoedinger equation and when written in this way implies

$$\frac{d\sigma}{d\Omega} = |f(\theta)|^2 \quad \text{scattering differential cross section} \tag{A.2a}$$

$$\sigma_T = \frac{4\pi}{k} \operatorname{Im} f(0) \quad \text{optical theorem.} \tag{A.2b}$$

We are interested in very high energy scattering so we use a large k approximation. Go to impact parameter representation via $\ell = kb - \frac{1}{2}$ with a continuous impact parameter, $\delta_\ell \rightarrow \chi(b)$, $d\ell/db = k$.

$$f(\theta) = -ik \int_{\frac{1}{2}k}^{\infty} b\,db \left[e^{2i\chi(b)} - 1\right] P_{kb-\frac{1}{2}}(\cos\theta).$$

Use the relation

$$\lim_{n\rightarrow\infty} P_n\left(1 - \frac{z^2}{2n^2}\right) = J_0(z)$$

and recall

$$\sin\left(\frac{\theta}{2}\right) = \sqrt{\frac{1 - \cos\theta}{2}}$$

to obtain

$$f(\theta) = ik\int_0^\infty b\,db\left[1 - e^{2i\chi(b)}\right] J_0\left[2kb\sin\left(\frac{\theta}{2}\right)\right]. \tag{A.3}$$

Since we are going to limit our discussion to cases of axial symmetry about the incoming particle direction we can recover a more familiar form by noting the following, where $\vec{k}_t$ is the component of momentum given to the scattering particle, perpendicular to the incident direction.

$$J_0(z) = \frac{1}{\pi}\int_0^\pi e^{iz\cos\theta}\,d\theta; \quad J_0(z) = J_0(-z); \quad k_t \approx 2k\sin\left(\frac{\theta}{2}\right)$$

for small θ.

We then have

$$f(\vec{k}_t) = \frac{ik}{2\pi}\int e^{-i\vec{k}_t\cdot\vec{b}}\,\Gamma(b)\,d^2b, \tag{A.4}$$

where we have made the following identification: $\Gamma(b) = 1 - e^{2i\chi(b)}$. This function is easy to invert:

$$\Gamma(b) = \frac{1}{2\pi ik}\int e^{i\vec{k}_t\cdot\vec{b}}\,f(\vec{k}_t)\,d^2k_t \tag{A.5}$$

and can be shown [Yennie, 1971] to be the shape of the scattering wave immediately downstream of the scatterer, in the following sense.

incident wave: e^{ikz}

immediately downstream of scatterer $\approx e^{ikz} - \Gamma(b)\,e^{ikz}$. The $\Gamma(b)$ are convenient to manipulate and because of the geometrical interpretation just given are called profile functions.

The next basic assumption is that the phase shifts from collisions with the nucleons in a nucleus are additive. Thus we assume implicitly that the nucleons do not overlap, or, if they do, it does not affect the phase shift they contribute to the scattering. This assumption can be written as

$$\chi(\vec{b}, \vec{s}_1, \ldots\ldots, \vec{s}_A) = \chi_1(\vec{b} - \vec{s}_1) + \ldots\ldots + \chi_A(\vec{b} - \vec{s}_A) \tag{A.6}$$

for the A nucleons in a nucleus. The $\vec{s}_i$ are the transverse position vectors of the nucleons.

The picture of what we assume is illustrated in Fig. (A.1)

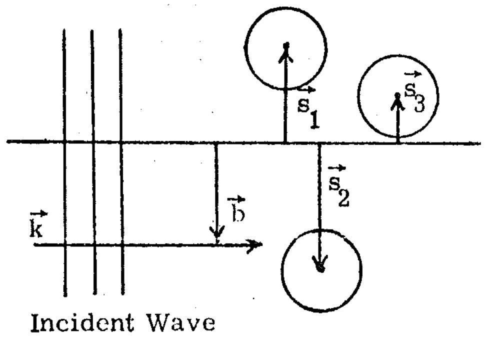

$\vec{k}$ is the momentum of the projectile and the $\vec{s}_i$ are the transverse component of the nucleon position vectors.

Fig. (A.1)

The projectile (or incident hadron) is assumed to plow straight through the nucleus collecting phase from the stationary nucleons as it goes. We can sum all nucleons because a "miss" is taken care of by a zero contribution from the missed $\chi(\vec{b} - \vec{s}_i)$. Obviously from the definition of $\Gamma(b)$ and the assumption (A.6), the following composition formula is implied for the $\Gamma(\vec{b} - \vec{s}_i)$.

$$1 - \Gamma^A(\vec{b}) = \prod_{i=1}^{A} [1 - \Gamma(\vec{b} - \vec{s}_i)] \quad \text{for A nucleons.} \tag{A.7}$$

Now we need to evaluate (A.7) between the groundstate wave functions of the nucleus. This is a very complex problem; however, we can achieve a great simplification by making some major approximations to the nuclear groundstate.

We assume that spin and isopsin are not important and all nuclei contribute identically to high-energy scattering. Also the precise spatial interrelationship of the nucleons is very complex, but we assume an independent particle model where one density describes the positions of all nucleons in the following way.

$$|\psi_0(\vec{r}_1,\ldots\ldots,\vec{r}_A)|^2 = \rho_A(\vec{r}_1,\ldots\ldots,\vec{r}_A) \simeq \prod_{i=1}^{A} \rho_1(\vec{r}_i) \tag{A.8a}$$

where

$$\rho_1(\vec{r}) = \int \rho(\vec{r},\vec{r}_2,\ldots\ldots,\vec{r}_A)\, d^3r_2\ldots\ldots d^3r_A. \tag{A.8b}$$

Using this independent particle nuclear density and our previous assumption about the non-importance of overlapping between nucleons we can evaluate the nuclear groundstate contribution to hadron scattering.

$$\begin{aligned} 1 - \Gamma^{(A)}(b) &= \prod_{i=1}^{A} \int d^3r_i\, [1 - \Gamma(\vec{b} - \vec{s}_i)]\, \rho_1(r_i) \\ &= \left[1 - \int d^3r\, \Gamma(\vec{b} - \vec{s})\, \rho_1(\vec{r})\right]^A. \end{aligned} \tag{A.9}$$

First we relate this result to the "smeared" density seen by a finite size projectile hitting the finite size nucleons, $\tilde{\rho}_1(\vec{b}, z)$. If we first note by Formula (A.4) that

$$\int \Gamma(\vec{b} - \vec{s})\, d^2s = \frac{2\pi}{ik} f(0), \tag{A.10}$$

where f(0) is the forward hadron-nucleon scattering amplitude, we are led to define $\tilde{\rho}_1(\vec{b}, z)$ by the following relation.

$$\int d^3r\, \Gamma(\vec{b} - \vec{s})\, \rho_1(r) \equiv \frac{2\pi}{ik} f(0) \int_{-\infty}^{\infty} \tilde{\rho}_1(\vec{b}, z)\, dz. \tag{A.11}$$

A standard notation often encountered is $T(\vec{b})$, which is just the amount of nuclear material encountered in traversing the nuclear at impact parameter $\vec{b}$.

$$T(\vec{b}) = A\int \rho_1(\vec{b}, z)\, dz = \int n_1(\vec{b}, z)\, dz. \qquad (A.12)$$

We have introduced $n_1(\vec{b}, z)$, a normalized total density. We can define analogous "twiddle" versions, $\tilde{T}(b)$ and $\tilde{n}_1(\vec{b}, z)$, that are "smeared" by the extent of the hadron-nucleon interactions, to abbreviate relation (A.11).

$$\tilde{T}(\vec{b}) = A\int \tilde{\rho}_1(\vec{b}, z)\, dz = \int \tilde{n}_1(\vec{b}, z)\, dz. \qquad (A.13)$$

By using the optical theorem (A.2b) and defining α as the ratio of real to imaginary part of the forward hadron-nucleon scattering amplitude, we can write

$$f(0) = \frac{ik}{4\pi}\sigma_T(1 - i\alpha), \qquad (A.14)$$

where σ_T is the hadron-nucleon total cross section. Using the above definitions and relations we obtain

$$\int d^3r\ \Gamma(\vec{b} - \vec{s})\, \rho_1(r) = \tfrac{1}{2}\sigma_T(1 - i\alpha)\frac{\tilde{T}(\vec{b})}{A}. \qquad (A.15)$$

A little thought shows that

$$\frac{\tilde{T}(b)}{A} \leq \frac{2R}{\left(\frac{4}{3}\pi R^3\right)} \sim \frac{1}{2R^2},$$

where R is the nuclear radius. σ_T must at most be the size of a nucleon so that as A gets larger, $\frac{1}{2}\sigma_T(1 - i\alpha)\tilde{T}(\vec{b})/A$ gets smaller and we can use the following approximation for (A.9).

$$1 - \Gamma^{(A)}(\vec{b}) = \left[1 - \int d^3r\, \Gamma(\vec{b} - \vec{s})\, \rho_1(\vec{r})\right]^A \simeq \exp\left[-\tfrac{1}{2}\sigma_T(1 - i\alpha)\tilde{T}(\vec{b})\right]. \qquad (A.16)$$

In the limit of small-angle scattering and potentials small and slowly varying compared to the kinetic energy one can identify a phase shift from the Schroedinger equation and derive a potential theory expression for $1 - \Gamma^{(A)}(\vec{b})$.

$$1 - \Gamma_{pot}(\vec{b}) \simeq \exp\left[-\frac{i}{2k}\int_{-\infty}^{\infty} U(\vec{b},z)\,dz\right]. \qquad (A.17)$$

So that we can think of a nucleus offering an effective potential of

$$U_{eff}(\vec{b},z) = -4\,f(0)\,\tilde{n}_1(\vec{b},z). \qquad (A.18)$$

We now have a solution to hadron scattering from a nucleus, by substituting (A.16) into (A.4) and then applying (A.2a) to obtain $d\sigma/d\Omega$.

$$\frac{d\sigma}{d\Omega} = \left|\frac{ik}{2\pi}\int d^2b\, e^{-i\vec{k}_t\cdot\vec{b}}\left\{1 - \exp\left[-\tfrac{1}{2}\sigma_T(1-i\alpha)\int_{-\infty}^{+\infty}\tilde{n}_1(\vec{b},z)\,dz\right]\right\}\right|^2. \qquad (A.19)$$

Now to gain some insight we try a simple example at this stage that is familiar from ordinary optics. We use an effective nuclear shape that is a disc of radius R and length l, perpendicular to the beam, even though a spherical shape casting this kind of shadow is not too physical for a real nucleus. Note that $\tilde{n}_1(\vec{b},z)$ integrated over the nucleus is normalized to A as is implied by its definition. We assume that the incident particle is only absorbed, $\alpha = 0$.

$$\begin{aligned}\tilde{n}_1(\vec{b},z) &= \frac{A}{l\pi R^2} \quad b < R;\ 0 < z < l \\ &= 0 \text{ elsewhere.}\end{aligned} \qquad (A.20)$$

If we do the ϕ integration to recover our Bessel function, we have

$$\begin{aligned} f(\theta) &= ik\int_0^{\infty} b\,db\; J_0\left[2kb\sin\left(\frac{\theta}{2}\right)\right]\left\{1 - \exp\left[-\frac{\sigma_T}{2}\int_{-\infty}^{+\infty}\tilde{n}_1(\vec{b},z)\,dz\right]\right\} \qquad (A.21)\\ &= ik\int_0^{R} b\,db\; J_0\left[2kb\sin\left(\frac{\theta}{2}\right)\right] C,\end{aligned}$$

where

$$C = 1 - \exp\left(-\frac{\sigma_T A}{2\pi R^2}\right).$$

By using $\int x\,J_0(x)\,dx = x\,J_1(x)$, we obtain

$$f(\theta) = ik\,\frac{C R\,J_1\left[2kR\sin\left(\frac{\theta}{2}\right)\right]}{2k\sin\left(\frac{\theta}{2}\right)}$$

$$\frac{d\sigma}{d\Omega} = |f(\theta)|^2 = k^2C^2R^4 \frac{J_1^2\left[2kR\sin\left(\frac{\theta}{2}\right)\right]}{\left[2kR\sin\left(\frac{\theta}{2}\right)\right]^2} . \tag{A.22}$$

In terms of $q^2 \simeq k^2\theta^2$ at small θ, and expanding $J_1(x)$ and e^{-x} and equating like powers of x, we obtain

$$\frac{d\sigma}{d\Omega} \simeq \frac{k^2R^4C^2}{4} \exp[-R^2q^2/4], \tag{A.23}$$

with q being the momentum transfer in the scattering.

We can now use this simple example to gain insight into the behavior of the model. The q^2 dependence is only related to the radius of the nucleus and not to the opacity which is in C^2 via σ_T. To a good approximation this behavior holds for the complete theory and observation. Our ρ photoproduction data are well fit by an exponential at low t and the slope is very consistent with that obtained from ψ(3.1) photoproduction from the same target, even though the σ_T for ρ-nucleon and ψ-nucleon scattering are quite different. This means that the detailed shape or slope of the coherent peak (where the nucleus is acting as a whole) tells us about the nucleus and not about the interaction of the incident particle. Although approximately true experimentally as we shall see, this is not an exact general result of the theory, but depends on the nuclear shape.

The absolute normalization, on the other hand, does depend on σ_T through its appearance in C. Thus we can measure σ_T by requiring that it have a value that gives the correct normalization. Yet another method of getting at σ_T is possible and to see what it is we expand C for σ_T small and large to see how the normalization depends on A, the number of nucleons.

For σ_T small

$$C^2 = \left[1 - \exp\left(\frac{\sigma_T A}{2\pi R^2}\right)\right]^2 \approx \frac{\sigma_T^2 A^2}{4\pi^2 R^4},$$

and still for σ_T small we obtain

$$\frac{d\sigma}{d\Omega} \approx \frac{k^2 \sigma_T^2 A^2}{16\pi^2} \exp(-R^2 q^2/4), \tag{A.24}$$

while for σ_T large we obtain

$$\frac{d\sigma}{d\Omega} \approx \frac{k^2 R^4}{4} \exp(-R^2 q^2/4). \tag{A.25}$$

Assuming a constant density for nuclear matter independent of A, the large σ_T limit goes as $A^{4/3}$ because then volume $\propto R^3 \propto A$. Thus the normalization for $d\sigma/d\Omega$ varies as $A^{4/3}$ for σ_T large and A^2 for σ_T small. Then if we choose a value of σ_T for our model that gives the right variation of $d\sigma/d\Omega|_{q^2=0}$ as a function of A, we will have determined σ_T independently of overall normalization. What is needed is a series of different nuclear targets to get the A dependence to be fit by the optical model. We can preview here the difficulty of this approach in photoproduction because it depends on something that we already have in the elastic-scattering case. Naturally one must use a reasonable nuclear model, but also we cannot assume $\alpha = 0$. The problem is that independent unique values of σ_T and α cannot be simultaneously determined from this analysis [Spital and Yennie, 1974b].

In summary we can obtain σ_T from the overall normalization on one nucleus or from a fit to an A dependence using only relative normalization between different nuclei. In both cases α must be input as an externally defined constant.

Aside: It is also worth noting that a nucleus with fuzzy edges will remove the zeros of the Bessel function result and yield an exponential in $-q^2$ out to larger q^2. One can see that in our elastic scattering model this will occur if one compares the following integral with the form of Eq. (A.21) and (A.23).

$$\int_0^\infty e^{-ab^2} J_0(qb)\, b\, db = e^{-q^2/4a}$$

This case (Gaussian) and several other integrable ones are worked out in [Feld, 1969]. One point worth noting is that the effect of σ_T is not confined to the normalization as it is exactly for the black disc model. End of Aside.

One of the points that may have come through in the discussion of finding σ_T for elastic hadron scattering was: Why bother? One can make a beam of hadrons and scatter them from a hydrogen target (protons) and get σ_T, but many hadrons like the ρ are not stable enough to form into a beam to hit a target. The ρ lifetime is about 0.5×10^{-23} sec, and at 20 GeV travels about 40 fermis before decaying. This is longer than the largest nuclei but very short on the atomic scale. Thus this indirect approach to σ_T may be the only way to measure the hadronic interactions of many short-lived particles. As we are about to see, the diffractive production of the ρ is very much like ρ elastic scattering in the optical model and the same approach to σ_T is possible in photoproduction as in the (hypothetical) ρ-nucleus elastic scattering just discussed.

Now we very briefly sketch the development of coherent photoproduction of neutral vector mesons. To be definite we shall always talk about the ρ, but the arguments and results are identical for all other neutral vector mesons. We work with the profile functions and combine them to build up the total profile and from that determine the production. We need a new kind of profile function, however, that will describe the production of particles. So in analogy to our old elastic profiles we define

$$\Gamma_{yx}(\vec{b}) = \frac{1}{2\pi i k_y} \int \exp(i\vec{k}_t \cdot \vec{b}) f_{yx}(\vec{k}_t) d^2 k_t, \tag{A.26}$$

where the profile function Γ_{yx} describes the scattering of a particle of type x on a nucleon to a particle of type y, which in principle could transfer quantum numbers to the nucleon. No such transfer occurs in the case of interest to us, $\Gamma_{\rho\gamma}(\vec{b})$, which describes the photon to ρ conversion on a nucleon. $\Gamma_\gamma(\vec{b})$ is the γ to γ scattering and is like the elastic profile functions we used before, similarly $\Gamma_\rho(\vec{b})$. As one would expect from VMD Γ_γ is of order e^2 and $\Gamma_{\rho\gamma}$ is of order e and we will work to order e^2.

If now the photon encounters a nucleus we must account for the transmission of the photon and the ability of the photon and ρ to scatter back and forth via $\Gamma_{\rho\gamma}$ and $\Gamma_{\gamma\rho}$. Initially the photon has amplitude 1 and the ρ has amplitude 0. Each amplitude has different wave number, k for the photon and k_ρ for the ρ, so that as they scatter on nucleons at different z positions, we must keep track of the relative phase of the two plane waves of the form e^{ikz}. After the first nucleon, located at impact parameter $\vec{s}_a$, the photon amplitude will be $1 - \Gamma_\gamma(\vec{b} - \vec{s}_a)$. Now, however, the ρ amplitude will be non-zero, $-\Gamma_{\rho\gamma}(\vec{b} - \vec{s}_a) \exp[i(k - k_\rho) z_a]$. The phase comes from the fact that this amplitude is for a ρ propagating with $\exp(ik_\rho z)$, while at z_a where it was created it had the photon phase, $\exp(ikz_a)$. At the next nucleon, which we shall label c to avoid double use of the letter b, more interesting things can happen. The photon amplitude, in addition to scattering as at nucleon a, can get a piece from the ρ component converting back into a photon component. Keeping terms of order e^2 allows all of the following possible contributions to the amplitude: $\gamma \rightarrow \gamma$, $\gamma \rightarrow \rho \rightarrow \gamma$, $\rho \rightarrow \gamma \rightarrow \rho$, and $\rho \rightarrow \rho \rightarrow \rho \rightarrow \rho$, etc. So to order e^2 the ρ and γ contribution after 2 scatters are:

$$\gamma: \quad 1 - \Gamma_\gamma(\vec{b} - \vec{s}_a) - \Gamma_\gamma(\vec{b} - \vec{s}_c) + \Gamma_{\gamma\rho}(\vec{b} - \vec{s}_c)\,\Gamma_{\rho\gamma}(\vec{b} - \vec{s}_a)\exp[i(k - k_\rho)(z_a - z_c)] \tag{A.27a}$$

$$\rho: \quad -\{\Gamma_{\rho\gamma}(\vec{b} - \vec{s}_c)\exp[i(k - k_\rho)z_c] + [1 - \Gamma_\rho(\vec{b} - \vec{s}_c)][\Gamma_{\rho\gamma}(\vec{b} - \vec{s}_a)\exp[i(k - k_\rho)z_a]\} \tag{A.27b}$$

We will write down the ρ after traversing the whole nucleus. Continuing the above process it must have a $\Gamma_{\rho\gamma}$ to make a ρ followed by $(1 - \Gamma_\rho)$ on the remaining nucleons to account for the ρ leaving the nucleus.

$$\Gamma^{(A)}_{\rho\gamma}(\vec{b}; \vec{s}) = \sum_i \left\{ \prod_{j \neq i} [1 - \Gamma_\rho(\vec{b} - \vec{s}_j)\,\theta\,(z_j - z_i)] \right]\Gamma_{\rho\gamma}(\vec{b} - \vec{s}_i)\exp(i\Delta_\rho z_i), \tag{A.28}$$

where $\Delta_\rho = k - k_\rho \simeq m_\rho^2/2k$ at large k. The θ function is a step function to insure that the ρ only sees nucleons occurring after the one where the γ-ρ conversion takes place. Read right to left (as quantum mechanical operations always are) (A.28) is exactly what the statement preceding it advertizes it to be.

As an aside we can see that our expression for $\Gamma^{(A)}_{\rho\gamma}$ satisfies VMD for the whole nucleus. For ρ mesons only, VMD requires that

$$\Gamma_\gamma(\vec{b}) = g_{\gamma\rho}\Gamma_{\rho\gamma}(\vec{b}) = g_{\gamma\rho}^{\;2}\,\Gamma_\rho(\vec{b}). \tag{A.29}$$

By VMD for the whole nucleus we mean that the profile functions for the whole nucleus $\Gamma^{(A)}$ obey (A.29), which is for a single nucleon. This can be done via a simple trick where, as we have been, we follow Yennie. In the demonstration one is forced to ignore the phase factors, which can be done as k gets large. Looking at (A.7) we see in our slightly modified notation.

$$g_{\gamma\rho}\Gamma^{(A)}_\rho(\vec{b}; \vec{s}) = g_{\gamma\rho}\left\{1 - \prod_j [1 - \Gamma_\rho(\vec{b} - \vec{s}_j)]\right\}$$

This can be rewritten as

$$= g_{\gamma\rho} \int_{-\infty}^{+\infty} dz \left\{ \frac{\partial}{\partial z} \prod [1 - \Gamma_\rho(\vec{b} - \vec{s}_j)\,\theta(z_j - z)] \right\}$$

$$= \sum_i \left\{ \prod_{j \neq i} [1 - \Gamma_\rho(\vec{b} - \vec{s}_j)\,\theta(z_j - z_i)] \right\} g_{\gamma\rho} \Gamma_\rho(\vec{b} - \vec{s}_i)$$

$$g_{\gamma\rho} \Gamma_\rho^{(A)}(\vec{b}; \vec{s}) = \Gamma_{\rho\gamma}^{(A)}(\vec{b}; \vec{s}), \tag{A.30}$$

where (A.29), nucleon-photon VMD, was used in the last step. Thus at high energies VMD applies to the nucleus as a whole. This result also indicates our earlier statement that ρ photoproduction could be understood by studying the hadron-nucleus scattering case.

Now we want to take (A.28) and make the approximations made earlier on hadron-nucleus scattering to get the result equivalent to (A.19) for vector meson photoproduction. To do this one takes the nuclear ground state expectation value of (A.28) using the independent particle model just as on (A.7). Again one exponentiates the absorption factor after assuming that the density for the nucleus varies more slowly than the Γ_ρ or $\Gamma_{\rho\gamma}$, just as before. The result is as follows.

$$\Gamma_{\rho\gamma}^{(A)}(\vec{b}) = \frac{2\pi}{ik} f_{\rho\gamma}(0) \int_{-\infty}^{\infty} dz\, \tilde{n}_1(\vec{b},z) \exp(i\Delta_\rho z) \exp\left[-\tfrac{1}{2}\sigma_\rho(1 - i\alpha_\rho) \int_z^\infty \tilde{n}_1(\vec{b},z')dz' \right], \tag{A.31}$$

where our notation is just as before. σ_ρ and α_ρ are σ_T and α for the ρ in particular and are the ρ-nucleon total cross section and the ratio of real to imaginary part for the forward ρ-nucleon scattering. $f_{\rho\gamma}(0)$ of course is the forward amplitude for photon to ρ scattering on a nucleon. Notice that the $\tilde{n}_1$ that appears in the exponential is from the ρ absorption and was present in the elastic scattering case. The other $\tilde{n}_1$ and $f_{\rho\gamma}(0)$ are from the photon-ρ scattering, so that in principle the two $\tilde{n}_1$ could be different, but we expect the two to be similar even without assuming VMD. In VMD one has:

$$f_{\rho\gamma}(0) = g_{\gamma\rho} f_{\rho}(0) = g_{\gamma\rho} \frac{ik}{4\pi} \sigma_{\rho} (1 - i\alpha_{\rho}). \qquad (A.32)$$

Using (A.4) and (A.31), we obtain for coherent ρ photoproduction,

$$\frac{d\sigma}{dt}^{\text{coherent}} (\gamma A \rightarrow \rho A) = |N_{\text{eff}}(t)|^2 |f_{\rho\gamma}(0)|^2 \qquad (A.33a)$$

$$N_{\text{eff}}(t) = \int d^2b dz \exp(i \vec{k}_t \cdot \vec{b} + i \Delta_{\rho} z) \tilde{n}_1 (\vec{b}, t) \exp\left[-\tfrac{1}{2} \sigma_{\rho}(1 - i\alpha_{\rho}) \int_z^{\infty} \tilde{n}_1(\vec{b}, z) dz'\right], \qquad (A.33b)$$

where $t = -(k_t^2 + q_{||}^2)$ is the invariant momentum transfer in the reaction.

In the discussion up to now we have used the ground state of the nucleus and have made no provision for the nucleus changing its state. The scattering from the individual nucleons adds in the amplitude and the nucleus recoils as a whole and casts a shadow and corresponding diffraction pattern that reflects the size of the nucleus. This scattering cannot persist as the dominant form at larger q^2 however because as more momentum is transferred to the nucleons in a nucleus they eventually get knocked out or excited and the nucleus no longer acts as a whole. This kind of scattering is called incoherent, because the nucleon scatterings do not add coherently. The method of calculating this scattering uses closure, a sum over all nuclear final states, because we do not know the nucleus final state and we observe scattering in principle with all final states.

Let us work with elastic scattering again as it is simpler than production, and we know from VMD that it is basically similar to vector meson photoproduction at high energies. Before, we took the final state of the nucleus to be the ground state $<0|$, but we can have a transition to any nucleon final state $<f|$ with a resulting profile function.

$$\delta_{f0} - \Gamma_{f0}^{(A)}(\vec{b}) = <f| \left[1 - \Gamma^{(A)}(\vec{b}_j; \vec{s}_i)\right] |0> . \qquad (A.34)$$

The δ function results from the orthoginality of the nuclear states and $\Gamma^{(A)}(\vec{b}_j; \vec{s}_i)$ is given by (A.7). The amplitude for a nuclear excitation process is

$$f_{f0} = \frac{ik'}{2\pi} \int \exp(-i\vec{k}_t \cdot \vec{b})\, \Gamma^{(A)}_{f0}(b)\, d^2b, \tag{A.35}$$

where k' is the hadrons' momentum after traversing the nucleus. Since energy loss in the nucleus is small compared to the beam momentum, we will ignore the difference between k and k' from now on. The cross section for scattering, with any possible nuclear state remaining, then must be: (the "cl" stands for closure)

$$\begin{aligned} \frac{d\sigma_{cl}}{d\Omega} &= \frac{k^2}{4\pi} \sum_f \iint d^2b\, d^2b' \exp[i\vec{k}_t \cdot (\vec{b}' - \vec{b})] < 0|\Gamma^{(A)^*}(\vec{b}; \vec{s})|f> < f|\Gamma^{(A)}(\vec{b}; \vec{s})|0> \\ &= \frac{k^2}{4\pi} \iint d^2b\, d^2b' \exp[ik_t \cdot (\vec{b}' - \vec{b})] < 0|\Gamma^{(A)^*}\Gamma^{(A)}|0>, \end{aligned} \tag{A.36}$$

where the second step uses the completeness of the nuclear states. Now since the sum over the final states must include the ground state to use closure as we just did, this result contains the coherent result in it and if we want the incoherent part alone, we must subtract the coherent part out. As in the coherent case we make the independent particle approximation for the nucleus as embodied in (A.8). At this point the manipulations grow cumbersome, but they are not subtle. We just substitute (A.7) into (A.36) and using (A.8) we multiply out all the terms and identify and remove those which make up the coherent result we calculated earlier. The result can be expressed in the following way, where the "inc" means incoherent.

$$\frac{d\sigma_{inc}}{d\Omega} = \frac{k^2}{4\pi^2} \int d^2b\, d^2b' \exp[i\vec{k}_i \cdot (\vec{b}' - \vec{b})] \times \left\{ [\lambda(\vec{b}, \vec{b}') + \mu(\vec{b}, \vec{b}')]^A - [\lambda(\vec{b}, \vec{b}')]^A \right\} \tag{A.37a}$$

where
$$\lambda(\vec{b}, \vec{b}') \equiv \left[1 - \int \Gamma(\vec{b} - \vec{s})\rho_1(\vec{r})\, d^3r\right] \left[1 - \int \Gamma^*(\vec{b}' - \vec{s}')\rho_1(\vec{r}')\, d^3r'\right], \tag{A.37b}$$

and

$$\mu(\vec{b},\vec{b}') \equiv \int \Gamma(\vec{b}-\vec{s})\Gamma^*(\vec{b}'-\vec{s})\rho_1(\vec{r})\,d^3r - \int \Gamma(\vec{b}-\vec{s})\rho_1(\vec{r})d^3r \int \Gamma^*(\vec{b}'-\vec{s}')\rho_1(\vec{r}')d^3r'. \qquad (A.37c)$$

The λ function has the appearance of an absorption term squared and the μ function looks like a scattering term squared, when compared to our earlier work. Thus if we expand the products in the curly brackets in (A.37a) we obtain the following.

$$A\lambda^{A-1}\mu + \frac{A(A-1)}{2}\lambda^{A-2}\mu^2 + \dots \qquad (A.38)$$

The first term is scattering from one nuclear and absorption from the next, the second term is scattering from two nucleons and absorption from the rest, etc. To the extent that ρ-nucleon scattering is absorptive we expect the single scattering term to dominate, and we will make this approximation, without claiming that the other terms are really negligible, so as to obtain a tractable result. Also we will not work at the smallest scattering angles, because in that region coherent scattering dominates in any nucleus of the size of beryllium or larger. Since $\rho_1(\vec{r})$ is normalized to 1 integrated over the nucleus it must go like A^{-1} so that the second term of μ can be neglected. It is also more spread out in b and b' and hence falls faster away from forward scattering. As before we exponentiate for large A and assume that the nucleons' size, as given by the Γ's, is small compared to the nuclear size as given by $n_1(\vec{r})$ and end up with

$$\left(\frac{d\sigma_{inc}}{d\Omega}\right) = \frac{k^2}{4\pi^2}\, d^2b\, d^2b' \exp\left[i\vec{k}_t\cdot(\vec{b}'-\vec{b})\right]\int d^3r'\,\Gamma(\vec{b}-\vec{s}')\Gamma^*(\vec{b}'-\vec{s}')\tilde{n}_1(\vec{r}')$$

$$\times \exp\left[-\int [\Gamma(\vec{s}-\vec{s}') + \Gamma^*(\vec{s}-\vec{s}')]\tilde{n}_1(\vec{r})\,d^3r\right] \qquad (A.39a)$$

$$= |f(\vec{k}_t)|^2 \int d^3r' \exp[-\sigma_T T(s')]\,\tilde{n}_1(\vec{r}') \qquad (A.39b)$$

$$\equiv N_1 |f(\vec{k}_t)|^2, \qquad (A.39c)$$

where $f(\vec{k}_t)$ is the amplitude for scattering from a single nucleon. Many approximations were used to arrive at (A.39b), but it contains the right behaviors. In the region away from $q^2 = 0$ ($k_t = 0$), where we expect the scattering to no longer be dominated by recoil of the whole nucleus (coherent scattering); the q^2 dependence of the scattering is essentially that of hadron-nucleon scattering, but not A times as strong because of shadowing effects. Thus N_1 is to be thought of as an effective number of nucleons seen by the incident hadrons. We can see this clearly if we look at the case σ_T small. From the normalization of $n_1(\vec{r}')$ we see that N_1 approaches A as we would expect with the nucleons no longer shadowing each other. Thus in this approximation and away from the region dominated by the diffractive peak all the q^2 behavior is from the underlying hadron nucleus scattering and only the normalization is affected by the nucleus. If we notice that N_1 depends on σ_T and that the A dependence of N_1 is different than the A dependence of the coherent normalization, then we see that there is hope of determining σ_T by looking at the incoherent part, much as with the coherent part from the normalization on one nucleus or from the relative normalization on several nuclei (A dependence). Also since the A dependence of the coherent and incoherent normalizations are different one could in principle determine σ_T from the relative normalization of coherent to incoherent production on a single nucleus. We make a tentative statement here because the theory of incoherent scattering (and production) from nuclei is not as well understood as the coherent case and results based on the normalization of incoherent reactions are correspondingly less reliable.

In order to determine the equivalent results for incoherent vector meson photoproduction to those just exhibited for incoherent scattering, we use closure and the independent particle and other approximations just used, however, we start with the profile function for vector meson photoproduction (A.28). The incoherent part of the reaction results from pairings of Γ and Γ^* for the same nucleon (we ignore nucleon-nucleon correlations at large angles as before), see

(A.37) and (A.38). The amplitude is made of two pieces, one where the incoherent reaction occurs on the same nucleon as the γ-ρ transition and the other where the $\Gamma^*\Gamma$ pairing for the incoherent scattering occurs after the γ-ρ transition has occurred on an earlier nucleon. The result in our standard notation is the following.

$$\frac{d\sigma_{\mathrm{inc,\,VMD}}}{d\Omega}(\gamma\rightarrow\rho) = \left|f_{\rho\gamma}(k_t)\right|^2 N_{\mathrm{eff}} \qquad \text{(A.40a)}$$

$$N_{\mathrm{eff}} = \int d^3r_a\, \tilde{n}_1(\vec{r}_a)\exp -\sigma_\rho \int_{z_a}^{\infty} \tilde{n}_1\, dz$$
$$\times \left| 1 - \int_{-\infty}^{z_a} dz_i \tilde{n}_1 \tfrac{1}{2}\sigma_\rho(1-i\alpha_\rho)e^{i\Delta_\rho z_i} \exp\left[-\tfrac{1}{2}\sigma_\rho(1-i\alpha_\rho)\int_{z_i}^{z_a}\tilde{n}_1(\vec{b},z_2)dz_2\right]\right|^2 . \qquad \text{(A.40b)}$$

At large k this is reducible to the following result, the obvious VMD result from elastic scattering (A.39).

$$N_{\mathrm{eff}} = \int d^3r_a \tilde{n}_1(\vec{r}_a)\exp\left[-\sigma_\rho\int_{-\infty}^{\infty}\tilde{n}_1(\vec{s}_a, z_2)dz_2\right]. \qquad \text{(A. 41)}$$

The remaining input to produce a complete model of vector meson photoproduction from nuclei has to do with the details of describing the nucleus. In the independent particle approximation we have used this consists of determining $\tilde{n}(\vec{r})$ for all the nuclei we use. Many previous analyses of vector meson photoproduction from nuclei have also included corrections to the independent particle model. This takes the form of two-body correlations and are not an important factor in the model. We do not include these effects, motivated to use the model without them because they are so poorly understood [Spital and Yennie, 1974b] and because large analyses of this type have been successful without them [Alvensleben et al., 1970].

Previous workers have generally used one of the following two forms for their optical density functions, although some analyses have used more primitive parameterizations.

$$n(\vec{r}) = n_0\left(1 + e^{(r - C)/z_f}\right)^{-1} \qquad \text{Fermi} \qquad (A.42)$$

$$n(\vec{r}) = n_0\left(1 + \delta\frac{r^2}{a_0^2}\right)e^{-r^2/a_0^2} \qquad \text{Shell Model} \qquad (A.43)$$

The parameters of the two models are C, z_f, a_0, δ, and n_0. These constants can be determined from either theory or results from other experiments such as electron scattering, or can be determined by the photoproduction data itself. For example, the nuclear radius (C in the Fermi model) is the primary determining factor in the q^2 (or $-t$) slope of the diffractive photoproduction cross section in the coherent region, just as it was for the simple grey disk scattering model we used earlier.

The Fermi model is generally considered to be more accurate for larger nuclei, and the shell model is preferred for light nuclei such as beryllium. However, [Alvensleben et al., 1970] use the Fermi model on nuclei of A down to 9 (beryllium) with good success. [Spital and Yennie, 1974] add a large number of small corrections to their optical model, including the use of the shell model for Be and C. They end up with results essentially identical to those of [Alvensleben et al., 1970] when using the same data.

Thus we follow [Alvensleben et al., 1970] in three major respects. We neglect correlations as they did. We use the Fermi shape for all nuclei as they did. We adopt their nuclear radii, measured under just these assumptions, from ρ photoproduction.

$$C = C_0 A^{1/3}; \; C_0 = 1.12 \pm 0.02. \tag{A.44}$$

z_f is fixed at 0.545 fm, a value used successfully in previous analyses. n_0 is defined by requiring the volume integral of $\tilde{n}(\vec{r})$ be equal to A.

We have defined a straightforward conventional optical model of a kind used quite successfully in the past. A study of the model parameter dependence of the optical model results ($|f_{\rho\gamma}(0)|^2$ and σ_ρ) is carried out in Chapter IV along with a test of our implementation of the model, on previously analyzed low-energy ρ photoproduction data from another group.

VITA

John Michael Bronstein [redacted] He entered Illinois Wesleyan University in 1966, where he received the degree of Bachelor of Science in Physics in 1970. Since 1970 he has been a student at the University of Illinois where he received the degree of Master of Science in Physics in 1972.